

**Surface Functionalization of Silicon Microwires for Use in Artificial
Photosynthetic Devices**

by

Jared Patterson Bruce

A Thesis submitted to the Faculty of Graduate Studies of

The University of Manitoba

In partial fulfilment of the requirements of the degree of

MASTER OF SCIENCE

Department of Chemistry

University of Manitoba

Winnipeg

Copyright © by Jared P. Bruce

Abstract

Integrated photoelectrochemical water splitting with sunlight is one possible solution to growing global energy needs. Integration of catalysts, photoabsorbers and a membrane require low barriers to charge dissipation if a free standing device structure is to be achieved. The n-type/PEDOT:PSS junction has been identified as the major resistive component and constitutes a large barrier to charge dissipation. In this thesis, the modification of the interface between n-type Si/PEDOT:PSS was achieved by growing a highly – doped region at the contact between the wire and the membrane to reduce voltage loss at the junction from 300 mV to 130 mV. In addition, modification of the surface using a thiophene moiety is observed to decrease the voltage loss from 300 mV to 30 mV.

Formation of an insulating silicon oxide on the methyl functionalized surface of the microwires identified a need for characterization of planar silicon samples representative of the sides of the microwires. Si (110), (211) and (111) crystal faces were functionalized with a methyl group and showed different resistance to oxidation. The Si (111) surface was the most resistant while the Si (211) surface was observed to be the least resistant to ambient oxidation.

Acknowledgements

Over my time at the University of Manitoba I have grown so much as a researcher and as a person. I was lucky enough to meet some of the best people in the world on this journey and I really can't thank them enough. I started off at the California Institute of Technology working with Nate Lewis and I really have to thank him for all his help and support over my time there and his continued efforts as I move forward with my career. Nate has been a real inspiration and mentor for me. Ron Grimm was a post doc that took me under his wing during my growing pains at Caltech and I can't say enough about his abilities and drive for science. James Blakemore, Adam Nielander, Joseph Beardslee, Shane Ardo, Fadl Saadi, Wes Sattler and Aaron Sattler are all such great people who I am lucky enough to have as friends. Bryce Sadtler was also my office mate at Caltech and I thank him for many insightful conversations.

Moving back to Manitoba, after being in California, was definitely bittersweet but I have to thank all of my lab mates for making it such a wonderful experience. We really had a great group that worked so well together and made coming to work every day a delight. Kevin McEleney helped me lay the foundation for the XPS work I have done. I am truly in debt to him for his knowledge and help with the XPS work. Mike McDonald was a PhD student before I entered the lab and finished his dissertation just before I defended my thesis. He really kept me grounded during my time and was always there to share a laugh with. Megan McClarty is one of the most intelligent people I know. Her curiosity and love of science is second to none and wherever she ends up, it will be a better place just for having her in it. Shaun Ryman, Akin Iyogun, Ramesh Kumar, Ehsan Tahmasebian, Onkar Kang and Elahe Asgari round out the rest of the wonderful day – to – day team that made our group so fun to work in. I also have to thank the talented undergrads who worked with me to make this thesis possible. Patrick Giesbrecht, Heather Cavers

and Sophia Schrekenbach were all great students and will all be very successful moving forward in their careers. I can't forget Denise McInnes who helped me so much when dealing with any paperwork in general and really took a lot of it off of our shoulders. Joey Lussier also stood by me in some of the tough times and I really can't thank him enough for all of his wonderful discussions over the past few years. I also would like to thank the members of my Committee, Drs. Derek Oliver and Mario Bieringer, for their comments and assistance in regards to this work.

Dr. Michael Freund has probably been the best supervisor I could have asked for during my time here at the University of Manitoba. He took a real chance by hiring me as a summer student during my undergrad and by sending me to Caltech to learn and grow into my own as a scientist with some of the best minds in the world. I always felt like I had his full support and confidence while I was away and when I returned. He has guided me through many unknowns and given me the space to explore my ideas. I don't think I would ever be able to thank him enough for what he has done for me.

In closing, I would like to thank my Mom (Sonya), Dad (Terry), Brother (Reid) and Sister (Larah) for all their love and support throughout my degree. They taught me how to get back up when something knocks you down and always kept me grounded with their teasing and laughter. They give me the confidence to strive for excellence and none of this would be possible without them.

Table of Contents

ABSTRACT	I
ACKNOWLEDGEMENTS	II
LIST OF TABLES.....	VI
LIST OF FIGURES.....	VII
LIST OF COPYRIGHT MATERIALS.....	XI
CHAPTER 1: INTRODUCTION TO SOLAR FUELS	1
1.1 - THE DRIVE TOWARDS RENEWABLE ENERGY	1
1.2 - SOLAR FUELS AND ELECTROCHEMISTRY.....	2
1.3 - JUNCTIONS IN SOLAR FUEL GENERATION	9
1.4 - INTEGRATED SOLAR FUEL GENERATION	15
CHAPTER 2: EXPERIMENTAL METHODS.....	20
2.1 - SILICON MICROWIRE SYNTHESIS	20
2.2 - SILICON SURFACE CHEMISTRY.....	22
2.3 - CHARACTERIZATION TECHNIQUES	24
2.3.1 - X-ray Photoelectron Spectroscopy.....	24
2.3.2 - Electrical Measurements	26
CHAPTER 3: IMPROVING THE CHARACTERISTICS OF SILICON MICROWIRE/P-TYPE CONDUCTING POLYMER JUNCTIONS FOR ARTIFICIAL PHOTOSYNTHETIC DEVICES.....	31
3.1 - INTRODUCTION	31
3.2 - EXPERIMENTAL	33
3.2.1 - Resistance Measurements to Characterize Dopant Density.....	35
3.3 - RESULTS.....	35
3.3.1 - Electrical Characterization of n ⁺ /n Silicon Microwires	35
3.3.2 - Surface Functionalization of Silicon Microwires	38
3.3.3 - Electrical Characterization of the PEDOT:PSS/Si Microwire Junction	42
3.3.3.1 - Changes in Resistivity and Metal Contacts	42
3.3.3.2 - Effects of Surface Functionalization.....	44
3.4 - DISCUSSION	50
3.4.1 - Electrical Behaviour of Differential Doping in Silicon Microwires	50
3.4.2 - X - ray Photoelectron Characterization of Silicon Microwires	50
3.4.3 - Junction Behavior of Si Microwires in Contact with PEDOT:PSS	52
3.4.3.1 - n ⁺ /n contribution	52
3.4.3.2 - Metal catalysts	54
3.4.3.3 - Thiophene termination	55
3.4.4 Impact of Losses in Model Artificial Photosynthetic Device.....	60
3.4 - CONCLUSION AND FUTURE WORK	63
CHAPTER 4: FUNCTIONALIZATION OF REPRESENTATIVE SILICON MICROWIRE SURFACES...65	
4.1 - INTRODUCTION	65
4.2 - EXPERIMENTAL	68
4.2.1 - Surface Chemistry.....	68
4.2.3 - X-ray Photoelectron Spectroscopy.....	69

4.2 RESULTS	69
4.2.1 Ideal Coverage of Si (110) and Si (211) Surfaces	69
4.2.2 H –terminated Planar Silicon Surfaces	74
4.2.3 Methyl Terminated Silicon Surfaces	75
4.3 DISCUSSION	79
4.3.1 Oxidation of H –terminated Planar Silicon Surfaces.....	79
4.3.2 Methylation of the Silicon Surfaces	80
4.3.3 Consequences of Methylation on Silicon Microwires.....	82
4.4 CONCLUSION AND FUTURE WORK	82
CHAPTER 5: CONCLUSIONS AND FUTURE WORK	84

List of Tables

Table 2.1: XPS parameters of high resolution analysis	26
Table 3.1: Summary of the data relevant to the direct-contact technique with W probes on Si microwires.....	37
Table 3.2: Summary of junction resistances of n-type silicon microwires in contact with PEDOT:PSS.....	44
Table 3.3: Summary of Si/PEDOT:PSS junctions with different groups attached to the surface.....	56
Table 3.4: Summary of voltage losses in a model integrated artificial photosynthetic device operating under AM1.5 conditions.....	62
Table 4.1: Summary of surface density and calculated surface to bulk ratios.....	71

List of Figures

- Figure 1.1: Electrochemical half reactions relevant to water splitting when compared to high and low work function metal. The standard hydrogen electrode is the proton reduction reaction at pH 1 under 1 atm of H₂. It is considered the standard reference for redox reactions in solution and is set to a potential of 0V.....4
- Figure 1.2: Formation of bands from individual energy levels of an ideal semiconductor for water splitting. The conduction band is situated negative of the proton reduction reaction and the valence band lies positive of the water oxidation reaction creating favorable thermodynamic conditions for water splitting.....5
- Figure 1.3: Common semiconductor materials and their band alignments with the water oxidation and hydrogen reduction standard potentials. The conduction band is shown to the left and the valence band is shown to the right. Copyright 2010 American Chemical Society.....7
- Figure 1.4: Solar energy air mass (AM) 1.5 solar spectrum in terms of photon and radiative energy. Copyright 2002 International Association of Hydrogen Energy.....8
- Figure 1.5: Band diagrams of junction formation between n-type semiconductor and metal. Band bending is described when the semiconductor work function is higher or lower than the Fermi level of the semiconductor. Copyright 2012 American Chemical Society.....10
- Figure 1.6: Current generation mechanisms across a Schottky junction. Under light conditions, electron – hole pair formation increases the minority charge carrier concentration near the surface and while the electric field drives them towards the interface and out of the semiconductor.....14
- Figure 1.7: Comparison of planar silicon wafer and silicon microwires. The cross section of a planar wafer is depicted on the left while the highlighted cross section of a wire is in the red circle. The absorption coefficient is represented by α and the minority charge carrier diffusion length is represented by L_d16
- Figure 1.8: Model solar fuels device with high – aspect ratio structures as the photoabsorbing materials. The red pillars are n – type materials for water oxidation, blue pillars are p – type materials for proton reduction and the green membrane will mediate ionic and electronic conduction between each side. The spheres on each of the wires represent catalysts for each reaction.....18

Figure 2.1: Microwire growth substrate preparation. 6N Cu is used as the growth catalyst in all of the Si microwire synthesis.....21

Figure 2.2: Block diagram of custom built chemical vapour deposition reaction chamber. The chamber was kept under high vacuum conditions while not in use. Two lines from the H₂ are used; one is sent through the SiCl₄ while the other brings the total flow rate to 500 sccm.....22

Figure 2.3: Nucleophilic addition of C-Si bond to the surface of silicon. Methyl Grignard or organolithium reagents are used to add the Si – C bond to the surface.....23

Figure 2.4: Single junction measurement of silicon microwire in contact with PEDOT:PSS. A full unit cell of a model device would have a p – type wire on one side of the PEDOT:PSS membrane and an n – type wire on the opposite side. R_{wire} is the slope of the resistance versus length measurement and the intercept is R_c.....29

Figure 2.5: a) Image of electrical junction characterization setup. The pads used in this image are Ag. b) Light microscope image of junction formed between Si microwire and PEDOT:PSS film at 200x magnification. The scale bar shows 10 μm.....30

Figure 3.1: Unit cell of model solar fuels device with electrical contributions to the total circuit highlighted. The n-type microwire and p –type microwire junctions are highlighted as the majority contributions to the iR loss in the system.....32

Figure 3.2: Contact resistance measurements of methylated highly doped base (n⁺n) Si microwires. Three independent measurements were performed at each individual point along the wire, and measurements were conducted by movement of the W probes in both directions along the Si microwire. (a) movement of the mobile probe from the n (top) to n⁺ (base) direction and (b) movement of the mobile probe from the n⁺ (base) to n (top) direction. The linearity of the data reflects the uniformity of the dopant concentration over the length scales considered throughout the regions investigated.....36 - 37

Figure 3.3: X-ray photoelectron spectra of surface functionalized silicon microwire arrays a) Survey spectra with comparison between methyl terminated wires and thiophene terminated wires b) High resolution spectra of the S 2s region c) High resolution spectra of the Si 2p region.....39

Figure 3.4: Complete coverage of the microwire surface with thiophene groups. The top of the figure shows the oxidation after 3 months in ambient conditions while the bottom shows coverage of the wires. A methylated microwire is the zero point for reaction time and degree of oxidation. Coverage and degree of oxidation are expressed as a percent of the Si 2p bulk peak for clarity.....41

Figure 3.5: *I-V* characteristics of methyl-terminated n-type Si microwires in contact with PEDOT:PSS. The low-doped end ($\sim 5 \times 10^{17} \text{ cm}^{-3}$) in contact with PEDOT:PSS was the only sample that exhibited a rectifying contact. For the highly doped region ($> 3 \times 10^{18} \text{ cm}^{-3}$) in contact with PEDOT:PSS, the *I-V* behavior was symmetric. The inset shows the low-bias region relevant to Air Mass 1.5 G operating conditions.....42

Figure 3.6: Semilog plot of operating current used to evaluate the *iR* losses for the different n-type Si microwires in contact with PEDOT:PSS. At 21 nA, the associated *iR* loss due to the junction between the highly doped Si microwire and PEDOT:PSS was 90 mV. The corresponding *iR* losses for the high-doped end and low-doped end of the n^+/n silicon microwire were 130 mV and 290 mV, respectively. Gold and copper catalysts that were left after surface functionalization produced *iR* losses of <10 mV and 50 mV, respectively.....43

Figure 3.7: Current – Voltage curves of thiophene functionalized silicon microwires in contact with PEDOT:PSS. a) p – type wire curves indicate tunnelling behaviour and b) n –type wire curves indicate leaky diode behaviour.....46

Figure 3.8: Addition of thiophene and its effect on junction resistance. Higher currents observed in reverse bias indicated by the arrow.....47

Figure 3.11: C 1s envelope of Si microwires. (a) methyl terminated wires show a distinct shift in the Si – C bond to the surface (b) thiophene terminated Si – C bond is convoluted, reducing accuracy for quantification of surface coverage.....51

Figure 3.12: Dipole orientations of terminating groups to silicon surfaces.....57

Figure 3.13: Interfacial energy diagram of n – Si in contact with PEDOT:PSS. The red lines indicate the HOMO/LUMO of the thiophene molecule. PEDOT:PSS workfunction is 5 eV.....59

Figure 4.1: Model of silicon microwire with dominant crystal phases highlighted for a 6 – sided wire. The right scanning electron image shows a real 6 – fold silicon microwire.....66

Figure 4.2: Unreconstructed Si (211) and (110) surfaces. The different colours represent possible surface bonding sites. In Si (211), the two colours represent distinct bonding sites. The blue represents one possible bonding site, similar to Si (111), while the pink represents two bonding sites, similar to Si (100). Si (110) has one possible bonding site that is similar across the whole surface.....67

Figure 4.3: X-ray photoelectron spectra of planar silicon sample. Top shows survey spectra, bottom left is the Si 2p high resolution spectr and the bottom left is the C 1s high resolution spectra.....72

Figure 4.4: Oxidation of H – terminated silicon surfaces over the course of 1 month. a) Ratio of Si_{oxide} to Si_{bulk} time dependence represented as a percentage for clarity b) Equivalent monolayers formed on each silicon surface.....74

Figure 4.5: Behaviour of methyl monolayer over the course of 1 month exposed to ambient conditions. (a) Ratio of methyl peak in C 1s to Si_{bulk} represented as a percentage for clarity. (b) Surface coverage expressed in monolayers.....76

Figure 4.6: Oxidation behaviour of methylated silicon surfaces. (a) Ratio of oxide peak to Si_{bulk} as a percent for clarity. (b) Number of monolayers of oxide formed over the course of a month.....77

Figure 4.7: Rate of oxidation for each planar silicon phase (a) Si (110) (b) Si (111) (c) Si (211) The dashed lines represent the H – terminated surfaces while the solid lines represent the methyl terminated surfaces.....78

List of Copyright Materials

- Walter, M. G.; Warren, E. L.; McKone, J. R.; Boettcher, S. W.; Mi, Q.; Santori, E. A.; Lewis, N. S., Solar water splitting cells. *Chemical Reviews* **2010**, *110* (11), 6446-73. Figure 2.....7
- Bak, T.; Nowotny, J.; Rekas, M.; Sorrell, C. C., Photo-electrochemical hydrogen generation from water using solar energy. Materials-related aspects. *International Journal of Hydrogen Energy* **2002**, *27* (10), 991-1022., Figure 10.....8
- Zhang, Z.; Yates, J. T., Band Bending in Semiconductors: Chemical and Physical Consequences at Surfaces and Interfaces. *Chemical Reviews* **2012**, *112*, 5520-5551. Figure 2.....10
- Gray, H. B., Powering the Planet with Solar Fuel. *Nature Chemistry* **2009**, *1* (1), 7. Figure 1.....18
- Chapter 4 was adapted with permission from Bruce, J. P.; Asgari, S.; Ardo, S.; Lewis, N. S.; Oliver, D. R.; Freund, M. S., Measurement of the Electrical Resistance of n-Type Si Microwire/p-Type Conducting Polymer Junctions for Use in Artificial Photosynthesis. *The Journal of Physical Chemistry C* **2014**, *118* (48), 27742-27748 Copyright 2014 American Chemical Society

Chapter 1: Introduction to Solar Fuels

1.1 - The Drive Towards Renewable Energy

Global energy consumption has grown significantly over the past decade. Large industrialized countries such as the United States, Canada and China require an immense amount of energy to sustain their high quality of life while growing populations and economic development in second and third world economies are intensifying the energy consumption on a global scale. In 2013, global consumption moved past 17 TW or 17×10^{12} W relying heavily on the use of fossil fuels to meet these needs.¹⁻³ As a result of such a reliance on fossil fuels, greenhouse gas emissions have also reached an unprecedented amount, creating concentrations of CO₂ in the atmosphere near 400 ppm.²⁻⁴

Policies imposed by nations around the globe represent a lack of recognition of current energy and climate projections. At the current rate, our energy needs are expected to surpass 30 TW by the year 2050. Our heavy dependence on fossil fuels with limited implementation of renewable resources presents an additional challenge for addressing climate concerns. Increasing the efficiency of processes reliant on fossil fuels is a good first step however, if we are going to meet the demand projected, then our supply will require a shift to carbon neutral, environmentally friendly renewable energy sources.

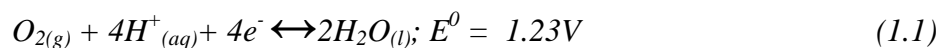
There are a wide variety of options for renewable resources that are currently available. Geothermal, wind, solar, hydroelectric, biomass and tidal currents all represent possible sources of renewable fuels.⁵ At the present time, wind and hydroelectric are the only technologies that are being used extensively, with hydroelectric power being especially prevalent in Manitoba. These technologies, however, will not provide sufficient amounts of energy to meet our growing

energy needs. Hydroelectric power has a gross energy output of approximately 5 TW if all rivers are developed and wind power is predicted to only output 3 TW.^{5, 6} Wind also has the added challenge of strict guidelines for use and issues related to reliability.

Solar energy has a vast, untapped potential. More energy from the Sun strikes the Earth in one hour than our total energy use in a year.⁵⁻⁸ Photovoltaics rely on direct conversion of light energy to electrical energy. However, issues related to consistent delivery of power, efficiency and cost have stunted widespread implementation of photovoltaic infrastructure. Coupling photovoltaic technology to the formation of chemical bonds would allow efficient energy storage and consistent delivery of power when these fuels are burned.⁹ In addition, this marriage between photovoltaic technology and chemical synthesis could be achieved with green fuels that would not exacerbate the climate issues.

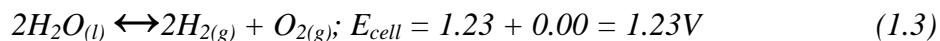
1.2 – Solar Fuels and Electrochemistry

Water is an abundant resource that can be used as a mediator in the conversion and storage of light energy as fuel. In any undergraduate chemistry class, water is often “split” into its components to illustrate fundamental principles of electrochemistry. The half – reactions that make up this experiment are as follows.



Electrochemical reactions are often measured relative to some well – defined reference. The absolute energy scale has its reference point at vacuum, where an electron is free and completely

detached from its bonds. This scale is cumbersome under solution conditions and is often substituted for a scale more practical under such conditions. The standard hydrogen electrode at pH 1 under 1 atm of H₂ is the standard reference for redox chemistry in solution. Many different reference electrodes can be used based on the solution conditions of the experiment. Equation 1.1 shows the oxidation or loss of electrons from water while Equation 1.2 shows the reduction or gain of electrons from protons to form hydrogen. The total cell potential is written as the sum of the oxidation and reduction potentials.



These cell and half – reaction potentials indicate the thermodynamic driving force required for the reaction to proceed. Half – reactions can be compared with metal work functions to determine whether a reaction will proceed spontaneously or non – spontaneously at its interface. A work function (ϕ_m) of a metal is the amount of energy required to remove an electron from the material. A high work function material requires a significant amount of energy to remove an electron or oxidize whereas a low work function metal is the exact opposite in that it takes a lot of energy to add an electron or reduce. Figure 1.1 represents work functions in the context of electrochemical potentials.

Lithium metal is an example of a low work function metal and readily gives up its electrons to become oxidized. The energy released by removal of the electron is much greater than what is required to reduce protons to hydrogen gas as seen in Figure 1. Gold, on the other hand, is an example of a high work function metal that is difficult to oxidize and does not have the energy required to reduce protons to hydrogen. However, oxidation of water to oxygen and protons could be carried out by gold. If reduction of protons is desired, gold can still perform this

reaction but requires an external electrical source to inject electrons into the material, thus raising its potential, driving the reaction.

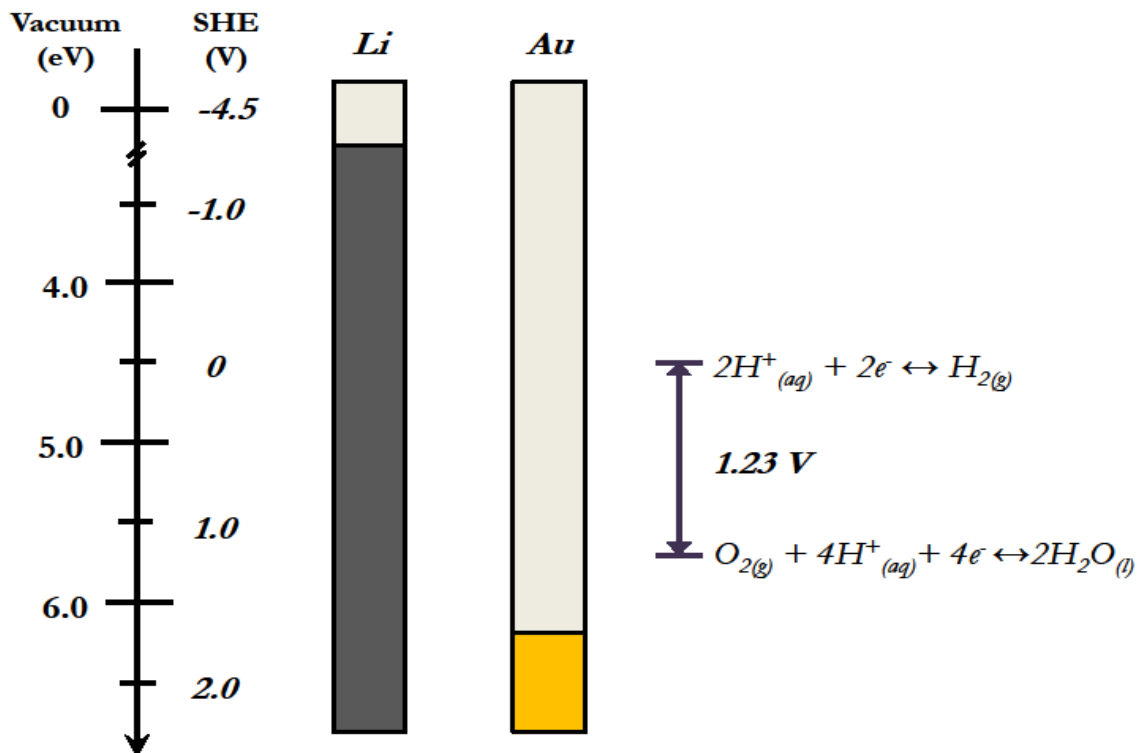


Figure 3.1 Electrochemical half reactions relevant to water splitting when compared to high and low work function metal. The standard hydrogen electrode is the proton reduction reaction at pH 1 under 1 atm of H₂. It is considered the standard reference for redox reactions in solution and is set to a potential of 0V.

The highest occupied molecular orbital (HOMO) and lowest unoccupied molecular orbital (LUMO) of individual molecular species can also be defined on each of the energy scales in Figure 1.1 above. Identical species can be added to the system until a semi – infinite condition exists, where the difference in the energy levels below the HOMO and above the LUMO is small enough to be considered a continuum, known as a band. Energy levels above the LUMO are grouped into the conduction band while energy levels below the HOMO are grouped into the valence band. The energy difference between the HOMO and LUMO where no other levels exist is known as the band gap. Metals tend to have very small band gaps in which charge carriers are

able to move freely between the conduction band and valence band with only thermal energy. In contrast, insulators have very large gaps in excess of 3 eV, which require a large amount of energy to move charge carriers between the conduction and valence bands. Semiconducting materials fall in between the two extremes of an insulator and metal. The amount of energy required to move a charge carrier from the valence band to the conduction band is usually in the ultra-violet and visible range of the light spectrum. Figure 1.2 shows the transition of a molecular species to a band structure of a semiconducting material.

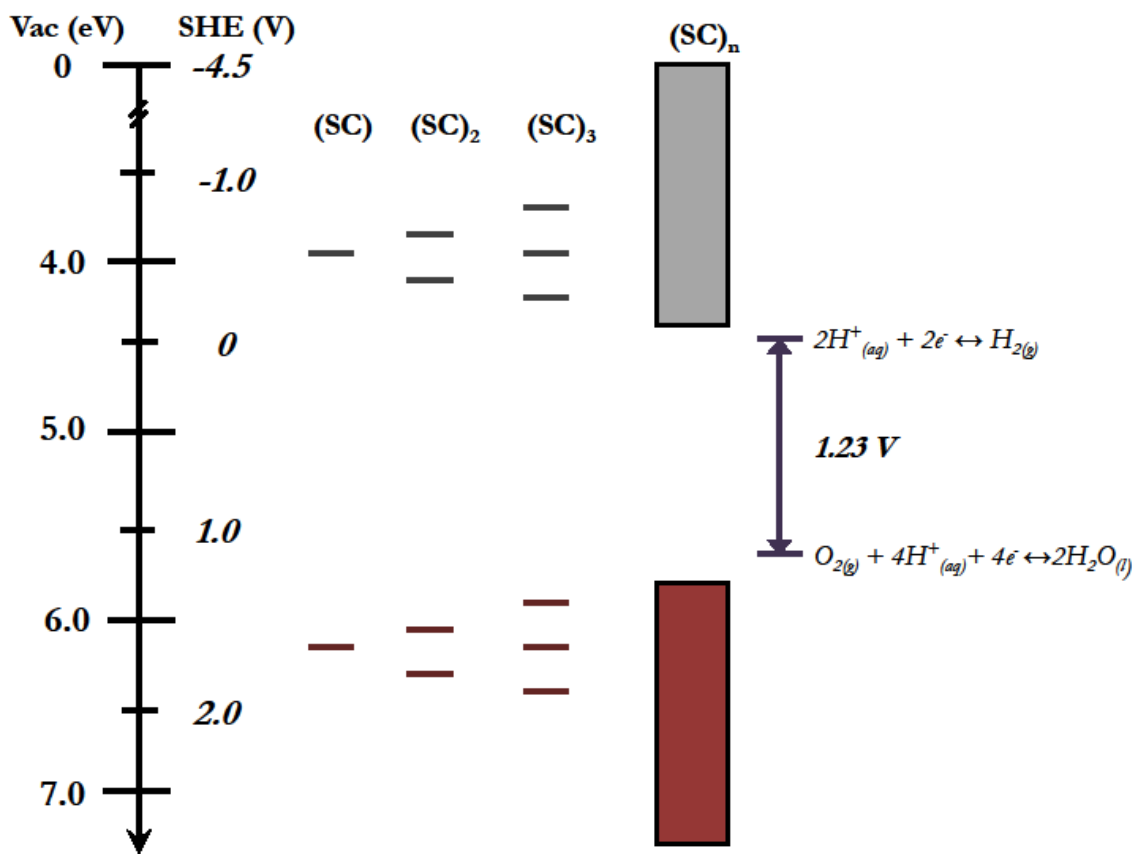


Figure 1.2 Formation of bands from individual energy levels of an ideal semiconductor for water splitting. The conduction band is situated negative of the proton reduction reaction and the valence band lies positive of the water oxidation reaction creating favorable thermodynamic conditions for water splitting.

Absorption of light by semiconductors promotes a negatively charged electron from the valence band to the conduction band leaving behind a positively charged hole. These charge carriers have the capability to do work external to the material if they can be collected without recombining internally. The energy available when these charge carriers are separated can be utilized to drive a chemical reaction given the energy of the HOMO or LUMO (oxidation or reduction) is greater than the electrochemical potential of the reaction. Figure 1.2 shows the band edge alignment of an ideal semiconductor for both the reduction of protons and the oxidation of water. Unfortunately, as is the case with many ideal systems, there are a limited number of materials that have the correct band alignment to run both reactions simultaneously while still absorbing a significant portion of the solar spectrum. In addition, excess driving force will be required to overcome losses inherent to the system. These losses have been proposed to be greater than 0.8V for a single semiconductor system due to thermodynamic contributions associated with the production of charge carriers and kinetic contribution from overpotentials associated with catalysts.^{10, 11}

A single junction solar device with two semiconductors connected in series is an alternative to a lone semiconductor approach to solar fuel generation. Each semiconductor could be relied on to drive the desired chemical reaction for water splitting based on its band alignment. A major drawback to a single junction device is that it requires the absorption of two photons instead of one; however, each semiconductor is not required to absorb the 1.23 V of solar energy to drive water splitting individually but can absorb a fraction of it as long as the band alignment is favorable. In Figure 1.2, for instance, one semiconductor would be responsible for driving the hydrogen reduction reaction while the other drives the water oxidation reaction. Semiconductors responsible for the hydrogen reduction reaction would be a p-type material, utilizing the driving

force of photogenerated holes from the conduction band energy while simultaneously; an n-type material would utilize the driving force of photogenerated electrons in its valence band in order to drive water oxidation. Proper band alignment is essential to driving the chemical reactions required for water splitting, overcoming losses highlighted earlier, at a significant solar – to – fuel efficiency. In Figure 1.3, common semiconductor band alignments are shown with respect to the standard water oxidation potential and hydrogen reduction potential.

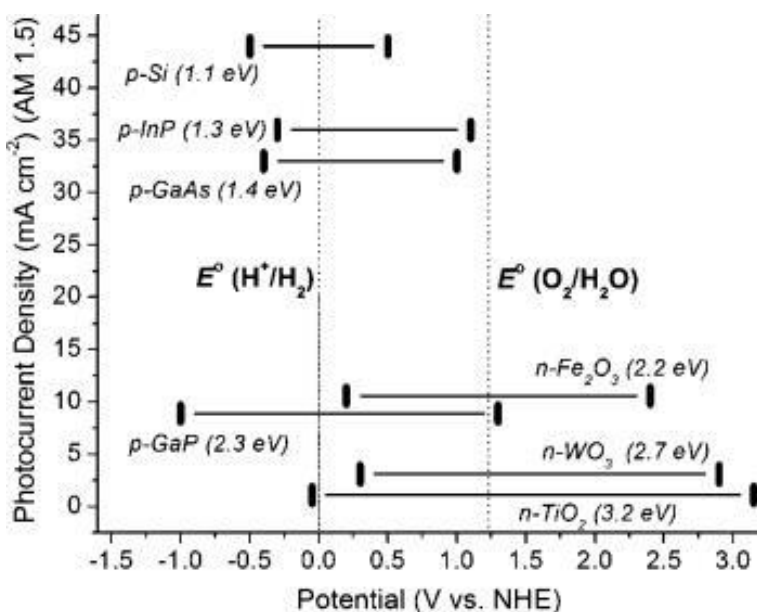


Figure 1.3 Common semiconductor materials and their band alignments with the water oxidation and hydrogen reduction standard potentials. The conduction band is shown to the left and the valence band is shown to the right. Copyright 2010 American Chemical Society

Dual semiconductor systems are not limited by light absorption of a single material to drive water splitting. In Figure 1.4, the majority of potential energy generated by solar irradiation under Air Mass (AM) 1.5 conditions lies in the visible region of the spectrum. AM1.5 is the optical path length of solar flux with respect to the surface normal of the Earth and is the standard condition for characterizing semiconductor light conversion efficiencies.¹⁰ A large, single band gap material such as TiO_2 (> 3 eV band gap) will not absorb any visible light but

could be electrically connected to a semiconductor, such as Si (1.12 eV band gap), that has a suitable band gap to absorb the light in the visible region, increasing the overall light collection of the device as a unit.¹² The minimum amount of energy required to thermodynamically split water is 1.23 eV as indicated in Figure 1.4, with an additional 0.8V to overcome any losses in the system. This additional driving force increases the energy requirement for water splitting to 2 eV or 600 nm for a single semiconductor system. Dual semiconductor systems would have multiple materials with different band gaps to absorb this energy.

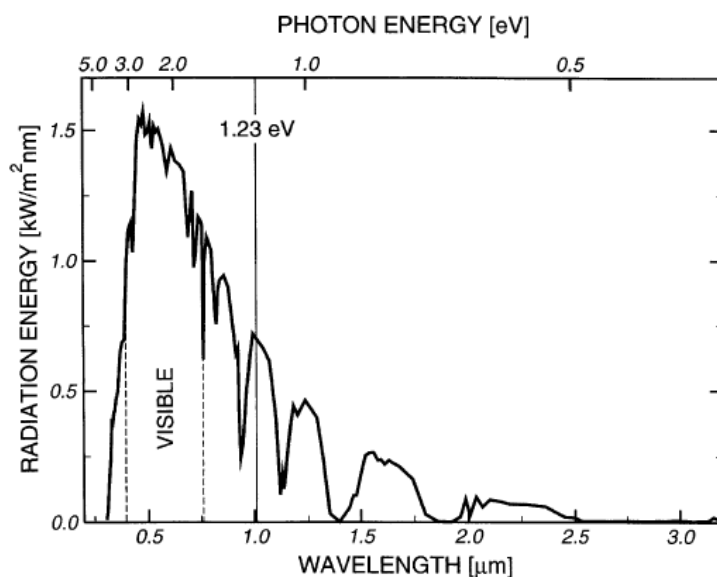


Figure 1.4 Solar energy air mass (AM) 1.5 solar spectrum in terms of photon and radiative energy. Copyright 2002 International Association of Hydrogen Energy

Single junction solar fuel devices need to be electrically connected if multiple semiconductors are used to drive water splitting. In addition, stability of the surface to aqueous conditions is an extremely crucial aspect of utilizing semiconductor substrates to split water. Formation of a thin insulating layer under aqueous conditions would hinder charge transport through the system and out of the material to drive the reactions. These layers also form mid – gap trap states that offer an alternative pathway to charge transport instead of through the

external circuit. This effect, known as recombination, reduces the solar – to – fuel efficiency of both single and multiple semiconductor devices. Understanding the electronic transport throughout the system is essential to creating a high efficiency solar fuel device.

1.3 – Junctions in Solar Fuel Generation

At the heart of solar fuel generation is the formation of junctions between different phases and materials. A solar fuel device relies on junction potentials to separate photogenerated charges allowing them to drive reactions. In addition, charge dissipation throughout the device requires the minimization of iR losses throughout the system; inability to achieve this will result in low solar – to – fuel efficiencies. Solid state junctions and semiconductor liquid junctions each have their place in a final device structure and understanding the nature of these junctions will enable high efficiency solar fuel devices to be created.

When two solid materials with different electrical potentials are brought in contact, the interface between these materials is known as the junction. Metal – semiconductor junctions are the simplest model to understanding the physical effects of junction formation. In Figure 1.5, the band diagram of an n-type semiconductor with a metal contact is shown.

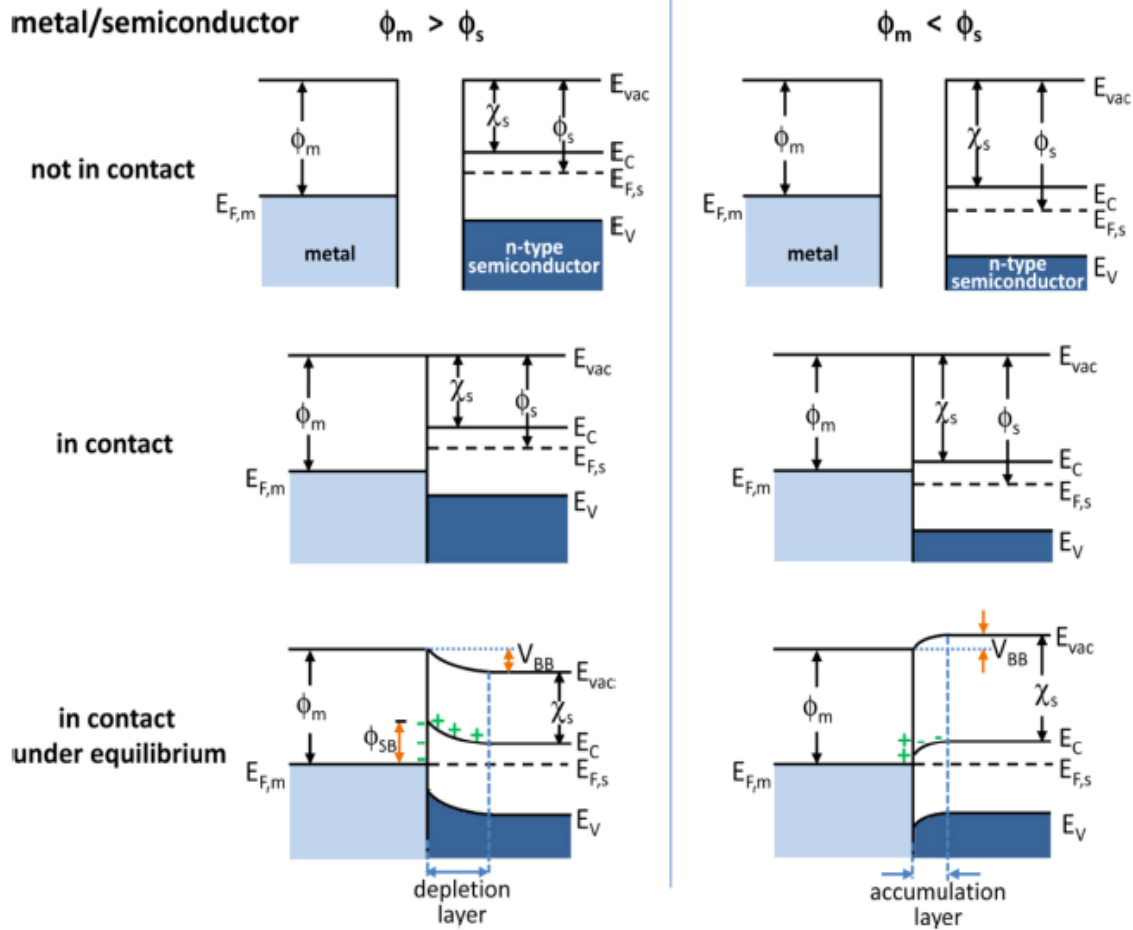


Figure 1.5 Band diagrams of junction formation between n-type semiconductor and metal. Band bending is described when the semiconductor work function is higher or lower than the Fermi level of the semiconductor. Copyright 2012 American Chemical Society

Prior to contact, the metal and semiconductor are each characterized by their individual work functions (ϕ_m and ϕ_s), the energy of the valence band maximum (E_V) and the energy of the conduction band minimum (E_C) or electron affinity (χ_s). When the semiconductor and metal come into contact, three conditions for the system are possible after equilibrium has been reached. The first is when the metal and semiconductor work function are the same ($\phi_m = \phi_s$) and no net charge transfer occurs across the interface between the metal and the semiconductor. When the metal work function is greater than the work function of the semiconductor ($\phi_m > \phi_s$), net charge transfer out of the semiconductor into the metal brings the system to equilibrium and

the Fermi level of the semiconductor equals the Fermi level of the metal ($E_{F,m} = E_{F,s}$). This is represented on the left in Figure 1.5 and because the semiconductor is doped with a low concentration of fixed dopants, an electric field is created as the charge becomes depleted at the interface. The semi – infinite nature of the electric field within the semiconductor allows this region to be characterized in one dimension and is known as the depletion layer.¹³ Finally, when the metal work function is less than the work function of the semiconductor ($\phi_m < \phi_s$), net charge transfer occurs into the semiconductor to reach equilibrium. After charge transfer has occurred, the depletion layer has an excess of charge and is, instead, called the accumulation layer. The creation of a space – charge region, where there is either an accumulation or depletion of charge and a subsequent electric field due to charge transfer is known as band bending.¹³ The degree of band bending is the difference in the work functions of the metal and the semiconductor as seen in Equation 1.4.

$$V_{bb} = |\varphi_m - \varphi_s| \quad (1.4)$$

In order to adequately describe the behaviour observed when characterizing these junctions, we consider the behaviour of the majority charge carrier moving from an infinite distance within the solid towards the interface.^{13, 14} For the n-type semiconductor in Figure 1.5, the electron is the majority charge carrier moving within the conduction band. When $\phi_m = \phi_s$ the degree of band bending is zero and the system is said to be under so called flat – band condition.¹³ An electron moving from an infinite distance towards the interface would not encounter an electric field and would move across the interface unaffected.

Under accumulation, ($\phi_m < \phi_s$), ohmic contact is observed and current flows from the metal to the semiconductor or vice –versa because of the directionality of the electric field at the

interface. The bands are bent in a downward fashion as the potential energy of the electron is lowered as it reaches the interface.

When the system is under depletion conditions, ($\phi_m > \phi_s$), the bands of the semiconductor are bent upward as is seen in Figure 1.5. An electron moving towards the interface now experiences an electric field that opposes its movement and an increase in energy is required for the electron to surmount the field and move into the metal. This field is known as a Schottky barrier (ϕ_{sb}) and only allows current to flow in one direction. The Schottky barrier is defined by the difference between the work function of the metal and the electron affinity of the semiconductor, which characterizes the conduction band edge, for an n-type semiconductor.^{13, 15} The current density – voltage (J – V) character of the junction follows an exponential function as seen in Equation 1.5.

$$J = J_0 \left[\exp\left(-\frac{qV}{\eta k_b T}\right) - 1 \right] \quad (1.5)$$

Where the current density flowing through the system is represented by J , the applied potential is V , q is the charge of the electron, k_b is the Boltzman constant, T is the temperature in Kelvin and η is the ideality factor. When charge transfer occurs over the barrier this is known as thermionic emission and under ideal conditions, the ideality factor approaches unity. J_0 is the saturated current density and is related to the Schottky barrier height obtained from thermionic – emission – diffusion theory assuming all voltage drops at the interface.¹⁵ Equation 1.6 gives the relation for the saturated current density.

$$J_0 = A^{**} T^2 \left[\exp\left(-\frac{q\phi_b}{k_b T}\right) \right] \quad (1.6)$$

A^{**} is known as the reduced Richardson constant and has consequences associated with changes in dopant density and temperature that are beyond the scope of this thesis. Connecting

the barrier height to the electrical properties of the junction is fairly straightforward using these relations and also highlights the effect of band bending on the electrical characteristics of the system.

Minority charge carriers experience the same electric field at the interface as the majority charge carriers. In the case of n – type silicon, holes have a concentration similar to intrinsic silicon ($\sim 10^{10} \text{ cm}^{-3}$) and are dwarfed by the concentration of majority carriers ($\geq 10^{15} \text{ cm}^{-3}$) in the bulk.¹⁵ Majority carrier concentration is equal to the dopant density in the semiconductor. The current observed under dark conditions is solely based on the transport of majority carriers over the barrier because of the large difference in concentration between minority and majority carriers in the semiconductor driven by the application of a voltage. The current observed under illumination conditions changes, however, because of the creation of electron – hole pairs in the space charge region near the interface. Under depletion conditions, electrons are repelled by the field while holes are attracted to the interface and driven out of the semiconductor into the metal creating a photocurrent. Figure 1.6 shows the mechanism of current generation under light and dark conditions.

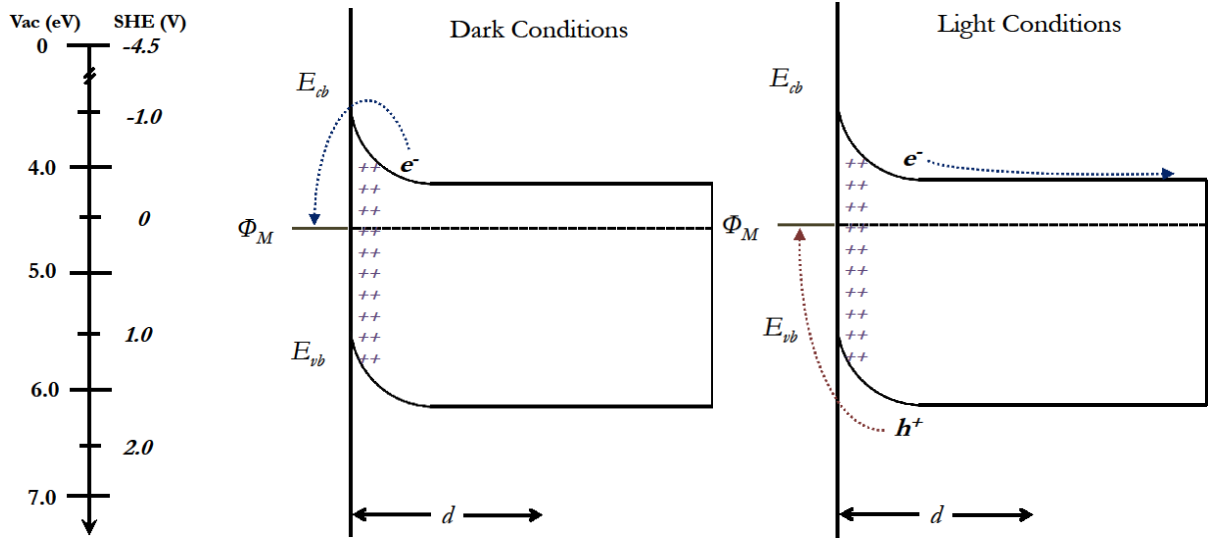


Figure 1.6 Current generation mechanisms across a Schottky junction. Under light conditions, electron – hole pair formation increases the minority charge carrier concentration near the surface and while the electric field drives them towards the interface and out of the semiconductor.

The resulting photocurrent generated from the minority charge carriers is added to the total current observed in the system. We can modify Equation 1.5 to account for the increase in current observed under illumination conditions.

$$J = J_{IL} + J_0 \left[\exp\left(-\frac{qV}{\eta k_b T}\right) - 1 \right] \quad (1.7)$$

Quantifying solar conversion efficiencies is done by carefully evaluating the resulting J-V curves of a dark and illuminated diode. Several parameters can be collected from these curves to report efficiencies. The open circuit potential (V_{oc}), short circuit current (J_{sc}), fill factor (FF) and maximum power point (P_{max}) are all collected from the resulting J-V curve of the illuminated diode. The efficiency (η) is then reported with respect to the incoming power. Under AM 1.5 conditions, the incident light is expected to give 100 mW/cm^2 of power to the system.^{6, 12, 16, 17}

$$P_m = J_p V_p \quad ff = \frac{J_p V_p}{J_{sc} V_{oc}} \quad \eta = \frac{J_p V_p ff}{P_{in}} \times 100 \quad (1.8)$$

Optimization of efficiency, from a photovoltaic standpoint, would be increasing the V_{oc} , J_{sc} and ff while lowering any losses from recombination and series resistances. Creation of fuels with a photoelectrochemical cell will rely on optimizing these parameters in addition to minimizing iR contributions from catalyst overpotentials and ionic movement through the system. Integrating all components into close proximity to reduce electric and ionic iR losses and optimizing the photovoltaic components are the foundation for a high efficiency artificial photosynthetic device.

1.4 – Integrated Solar Fuel Generation

Integrated photoelectrochemical splitting of water would reduce iR losses and utilizes multiple photoabsorbers to gather the energy required to split water. Silicon is one of the most abundant elements and has been studied extensively in literature making it a very attractive photoabsorbing material for integrated photoelectrochemical cell capable of splitting water. The alignment of its band edges, as observed in Figure 1.3, make it an attractive candidate for the photocathode responsible for the proton reduction reaction. Despite its high abundance, the cost of silicon photovoltaics is quite high for widespread, industrial utilization.¹⁸ This stems from an extremely energy intense and expensive fabrication process to create high quality silicon free of recombination centers that reduce efficiency.¹⁸⁻²² Circumventing this process by using low quality materials with photovoltaic characteristics similar to high quality silicon would assist in dropping the overall cost of silicon to make it more viable on an industrial scale.^{7,8}

Orthogonalization of light absorption and charge carrier collection is one approach for achieving high efficiency photovoltaic characteristics from low quality materials, such as silicon. High – aspect ratio structures are designed for charge collection to occur in the short dimension while light absorption would occur in the long dimension. Structuring the material in this fashion

depends on its absorptivity and usually requires collection of greater than 90% of the incident light to reach maximum efficiencies.⁷ In the case of silicon, a minimum of 110 μm of material is required for the absorption of 90% of the incident light and microwires are grown to achieve this absorption.^{18, 23} In Figure 1.7, the long axis of the silicon microwire structure is the light absorption dimension whereas the short axis is the dimension where minority charge carrier collection would occur.

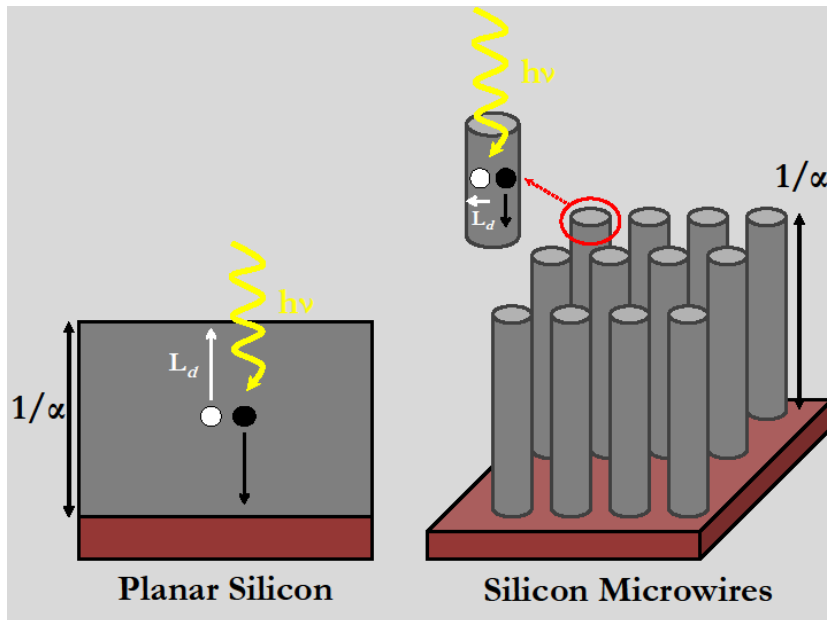


Figure 1.7 Comparison of planar silicon wafer and silicon microwires. The cross section of a planar wafer is depicted on the left while the highlighted cross section of a wire is in the red circle. The absorption coefficient is represented by α and the minority charge carrier diffusion length is represented by L_d .

Longer diffusion lengths increase the probability for photogenerated charge carriers to recombine because of the increased probability of falling into a trap state.¹⁵ In a planar silicon wafer, the charge carriers generated at the absorption depth limit are required to travel that distance without undergoing recombination. However, by collecting these carriers in the short dimension of a microwire, these carriers are no longer required to travel a long distance to be collected; allowing for higher defect density material to be used at a reduced cost to fabricate.²³

Fabrication of these high – aspect ratio structures is possible by a variety of different mechanisms. Chemical vapour deposition using a metal catalytic seed allows for high fidelity arrays of silicon microwires to be grown over areas $> 1 \text{ cm}^2$ and has also been demonstrated at the wafer scale.^{20, 23, 24} These microwire arrays can be doped during growth to create n or p –type silicon with similar dopant densities to their planar counterparts and also show respectable photovoltaic characteristics with V_{oc} greater than 400 mV and J_{sc} values greater than 10 mA/cm^2 yielding a 5% efficient solar cell.^{25,26} A model solar fuel generator using high – aspect ratio structures as the photocathode and photoanode is shown in Figure 1.8. The oxidation of water and reduction of protons would be carried out in separate compartments. All of the components would be integrated together and anchored by a membrane capable of ionic and electronic transport.¹⁷ Integration in this fashion would bring all of the components in close proximity to one another in an attempt to minimize any ionic and electronic losses that may be present in the system. Ionic losses are of particular interest when dealing with the membrane of the system however, strategies addressing ionic losses are currently being investigated elsewhere.^{17, 27, 28} Electrical losses are often compensated or neglected when controlling the system with an external source, however, the upper bound of the input power driving this system is based on the incident light. Therefore, in order to maximize the efficiency of the system and to ensure that any losses are below the 800 mV threshold highlighted in the previous section, identification and characterization of these losses are crucial to understanding the behaviour of a free – standing, integrated photoelectrochemical cell capable of water splitting and hydrogen fuel generation.

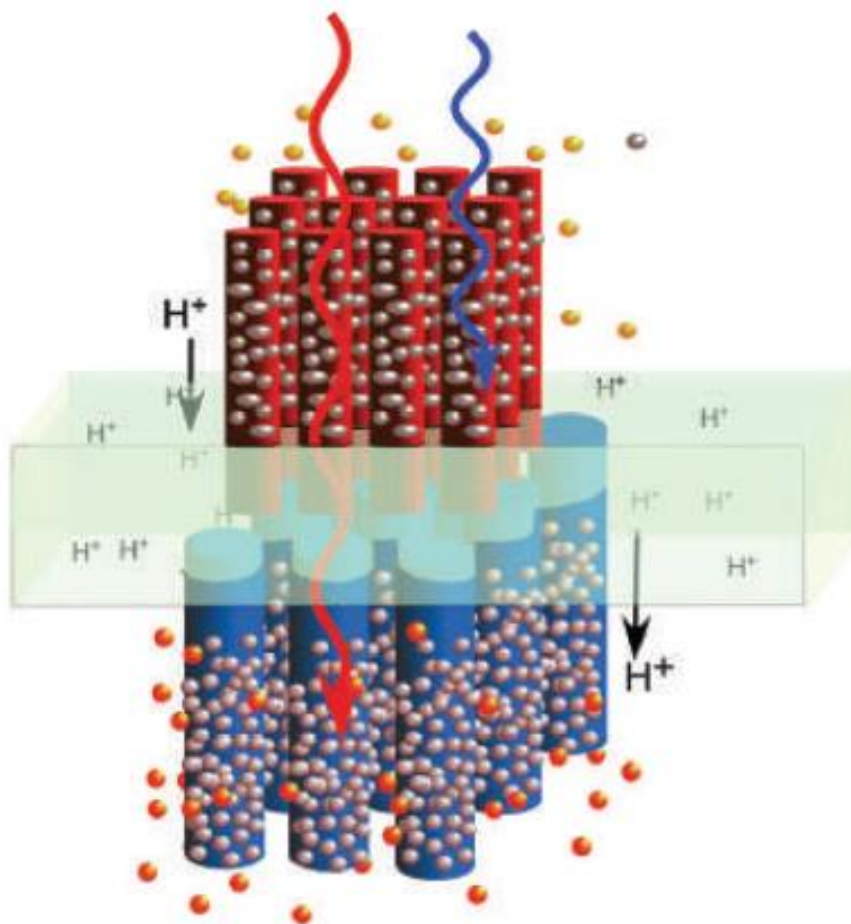


Figure 1.8 Model solar fuels device with high – aspect ratio structures as the photoabsorbing materials. The red pillars are n – type materials for water oxidation, blue pillars are p – type materials for proton reduction and the green membrane will mediate ionic and electronic conduction between each side. The spheres on each of the wires represent catalysts for each reaction. Reprinted by permission from Macmillan Publishers Ltd: Nature Chemistry Ref (9), Copyright 2009

The works presented in this thesis contribute to two individual aspects related to integration of high aspect ratio silicon microwire arrays into a final device structure. The first addresses the electrical contribution of the solid state junctions to the overall loss for integrated photoelectrochemical splitting of water. Two strategies are utilized; one that focuses on bulk electrical conductivity at the interface between the microwire and PEDOT:PSS while the second uses a different moiety to functionalize the surface and protect against the formation of silicon

oxide on the surface. Each approach will be evaluated on its own merit and compared to one another based on the observed effects on the resistance of the junction.

Second, the surface of silicon microwire arrays are quite complex when compared to planar silicon. Characterization of the surface functionalization by X – ray photoelectron spectroscopy (XPS) has been developed in the literature for planar Si (111) and (100)^{29, 30} but not for surfaces relevant to the microwires or the microwires themselves. Characterization of surface functionalized planar silicon surfaces relevant to the silicon microwire arrays is presented. Protection of the surface with a methyl group is evaluated for each individual surface and conclusions are drawn based on the completion of termination and resistance to oxide formation. Conclusions from this study will also help prevent the formation of silicon oxide on the microwire by ensuring the surface is fully functionalized and will assist in the development of new techniques for characterization.

Chapter 2: Experimental Methods

The development of silicon microwires has enabled high efficiency photovoltaic devices to be created with cheap materials but the formation of a silicon oxide layer continues to hinder charge transport out of the material. In addition, surface chemistry of planar silicon wafers of Si (111) and Si (100) are well established but the majority of exposed crystal faces on the wire are not of these orientations. Throughout this chapter the procedures and techniques used to fabricate and characterize the microwires and their properties will be highlighted and discussed.

2.1 – Silicon Microwire Synthesis

Silicon microwire substrates were fabricated using double – side polished, degenerate p^+ – type Si (111) substrates ($\rho < 0.005 \Omega \cdot \text{cm}$; Addison Engineering). A 500 nm thick thermal oxide layer was grown on the surface of a 3 inch wafer followed by a photolithographic process to create a template of circular holes with a 3 μm diameter and 7 μm pitch center to center. The oxide layer was then etched off using buffered oxide etch (Transene; **BOE contains hydrofluoric acid and ammonium fluoride both of which are extremely poisonous. Be sure to read the MSDS and take proper training for handling and disposal*) and transferred to a metal evaporator to deposit 500 nm of 6N copper. After deposition, photoresist was removed using acetone and the substrates were stored out of the light until further use. Figure 2.1 shows the substrate preparation process.

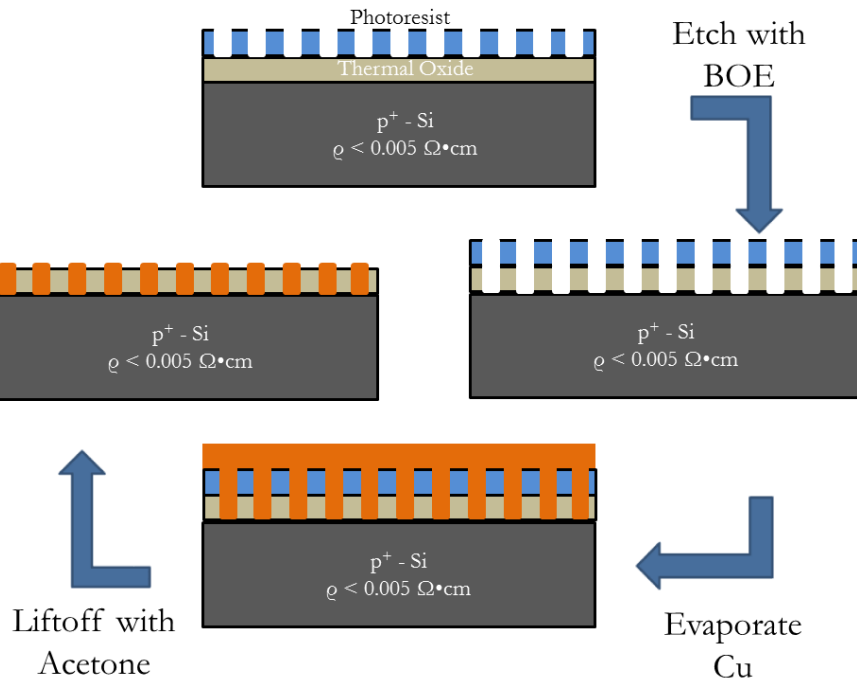


Figure 2.1 Microwire growth substrate preparation. 6N Cu is used as the growth catalyst in all of the Si microwire synthesis.

Silicon microwires were fabricated in a custom built chemical vapour deposition (CVD) reactor. Small pieces of growth substrate (1 x 3 cm) were added to the reaction chamber and heated to 1000°C under $\text{H}_{2(\text{g})}$ (6.0 Semiconductor Grade, Welders Supply). A separate line of $\text{H}_{2(\text{g})}$ was used to bubble through silicon tetrachloride (SiCl_4 ; Strem Chemicals, Fibre optic grade) which was then sent into the reaction chamber. The wires could be doped either p or n by the use of BCl_3 (5N, 250 ppm in $\text{H}_{2(\text{g})}$; Matheson Tri-Gas) or PH_3 (5N, 100 ppm in $\text{H}_{2(\text{g})}$) respectively. The flow of SiCl_4 was set at 50 sccm and dopant levels would be changed based on the flow rate into the reaction chamber. Dopant flow rates varied from 0.1 sccm to 5 sccm based on the desired dopant density of the wires. The total flow into the CVD chamber was set at 500 sccm and any difference was made up by a separate flow of $\text{H}_{2(\text{g})}$. The length of the wires was controlled by the reaction time and lengths could vary from 50 – 200 μm however, the majority

of wires used in this study were $\sim 100\ \mu\text{m}$ long. Figure 2.2 illustrates a block diagram of the CVD reaction chamber and where each flow of gas originates.

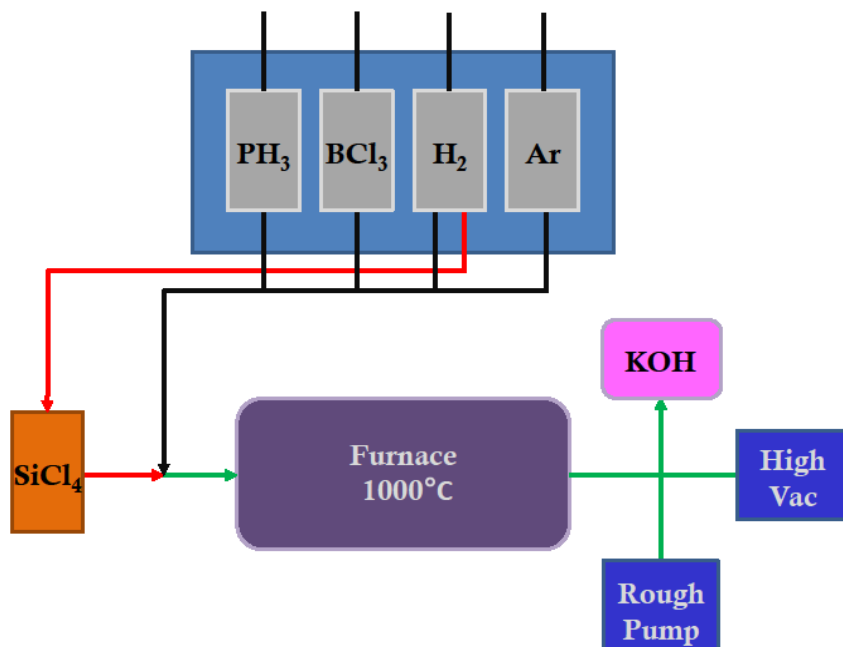


Figure 2.2: Block diagram of custom built chemical vapour deposition reaction chamber. The chamber was kept under high vacuum conditions while not in use. Two lines from the H₂ are used; one is sent through the SiCl₄ while the other brings the total flow rate to 500 sccm.

After the gases have passed through the quartz tube in the furnace, they enter a 6M KOH bath that oxidizes any remaining reactants that could be present. Phenolphthalein is used in the KOH scrubber to indicate when the solution turns neutral and, therefore, needs to be replaced.

2.2 – Silicon Surface Chemistry

Silicon and its propensity to the formation of a thin, insulating oxide layer is of particular interest. This oxide layer hinders charge transfer out of the material and also forms a mid – gap state that becomes a charge recombination center at the surface.^{31, 32} One approach that has had great success and garnered significant interest in the literature is the formation of a Si – C bond

at the surface.³²⁻³⁵ Formation of a Si – C bond can be achieved using hydrosilylation via thermal or photogenerated attachment^{36, 37} and through the use of Grignard or organolithium reagents.^{31-33, 35, 38} In the work of this thesis, the use of organolithium or Grignard reagents was utilized for the formation of a Si – C bond to silicon surfaces. The synthetic route is shown in Figure 2.3.

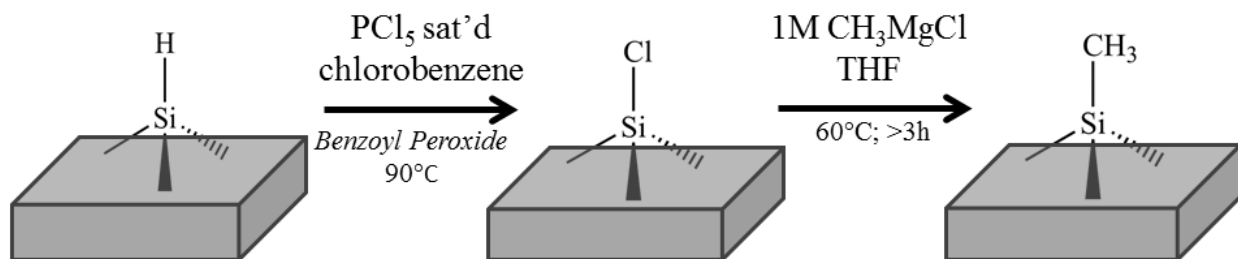


Figure 2.3: Nucleophilic addition of C-Si bond to the surface of silicon. Methyl Grignard or organolithium reagents are used to add the Si – C bond to the surface.

This approach is very attractive because each reaction step is carried out in solution. A small, 3 x 1 cm, piece of silicon is cut from a larger, 3 inch, wafer (Addison Engineering, Virginia Semiconductor Inc.). The native oxide layer was removed using a 10% v $\text{HF}_{(\text{aq})}$ dip and was removed in the same manner after each RCA clean throughout the procedure. Organic contaminants were removed using 1:1:5 (v/v/v) $\text{NH}_4\text{OH}:\text{H}_2\text{O}_2:\text{H}_2\text{O}$ solution commonly referred to as a RCA 1 clean. Metal contaminants were removed using 1:1:6 (v/v/v) $\text{HCl}:\text{H}_2\text{O}_2:\text{H}_2\text{O}$ commonly referred to as a RCA 2 clean. The H-terminated surface was created by submersing a silicon piece into nitrogen purged ammonium fluoride (40% v; NH_4F , Transene) solution. The solution was purged for a minimum of 30 minutes before samples were added. During etching, samples were agitated periodically to keep them from sticking to one another and to keep bubbles off of the surface. Silicon samples were etched in NH_4F for 6 – 10 minutes before being transferred to a N_2 purged glovebox where O_2 levels never exceeded 10 ppm.

Silicon pieces were transferred to a saturated solution of PCl_5 (Alpha Aesar, 99.998% metal basis) in chlorobenzene (anhydrous, 99.98% Sigma Aldrich) to generate the Cl-terminated surface. A few grains (< 1 mg) of benoyl peroxide were added to the mixture and the solution was heated to 90°C for 45 minutes. Afterwards, the solution was then allowed to cool for ~10 minutes and samples were washed with copious amounts of chlorobenzene and THF (anhydrous, >99.9% inhibitor free Sigma Aldrich).

Silicon pieces were then transferred to a 1M solution of Grignard or organolithium solution and excess THF or diethyl ether was added to the solution to prevent solvent loss during the reaction. The solution was heated to 60°C for a minimum of 3 hours when using THF and 40°C when using diethyl ether. After the reaction, samples were rinsed copiously with THF and methanol (anhydrous, 99.8% Sigma Aldrich) before being removed from the glovebox in methanol. Samples were sonicated and rinsed with methanol, isopropanol, acetonitrile and water before being transferred to the XPS chamber for analysis. Any samples that were unable to be characterized immediately after the final rinsing procedure were transferred back to the glovebox to be stored under the N_2 environment.

2.3 – Characterization Techniques

2.3.1 – X-ray Photoelectron Spectroscopy

Analytical techniques used for investigating the surface of a sample are generally limited by the amount of material available for observation. For instance, the surface density of a Si (111) plane is $7.8 \times 10^{14} \text{ cm}^{-2}$ is more than 7 orders of magnitude less than Avogadro's number and makes using traditional solution based techniques such as nuclear magnetic resonance, infrared spectroscopy or mass spectrometry extremely challenging.

X – ray photoelectron spectroscopy (XPS) is one of the most useful analytical techniques to characterize the surface of a solid. Excitation using X – ray radiation ejects core electrons from atoms in the solid which are used to characterize chemical species on the surface.

$$E_{KE} = h\nu - E_{BE} - \phi \quad (2.1)$$

Where E_k is the kinetic energy of the electron, $h\nu$ is the energy of the irradiating source, E_{BE} is the orbital binding energy and ϕ is the workfunction of the material. The quantized state of the energy levels of an atom yields a characteristic energy associated with the orbital where the electron is located. Equation 2.1 can be rearranged and expressed in terms of binding energy,

$$E_{BE} = h\nu - E_{KE} - \phi \quad (2.2)$$

which is independent of the instrument on which the analysis is carried out. X –rays have the ability to penetrate into the solids, sometimes travelling through an entire sample depending on the absorptivity of the material to X-ray radiation but are not the source of surface sensitivity synonymous with XPS. The mean free path of an electron moving in a solid is often only a few nanometers and, as such, any photoelectrons ejected from a material originate from the first few nanometers near the surface. Photoelectrons generated in the bulk are scattered before they are ejected, preserving the surface sensitivity of the technique.

Chemical bonding is confined to the activity of the valence electrons however; their interactions with other species influence the core electrons and signals observed with XPS. Bonding of more or less electronegative elements will cause a subsequent shift in the spectra to either higher or lower binding energies respectively. Measurable shifts in the spectra and peak fitting will allow for quantitative analysis of the surface chemistry performed herein.

All XPS spectra were collected on a Kratos Axis Ultra DLD XPS spectrometer using Al K α (1486.7 eV) monochromatic light at 10 mA emission current and 15 kV anode voltage. The base pressure never exceeded 1×10^{-9} Torr and no charge neutralization was used as samples were conductive enough to prevent charge buildup. All spectra were collected with a fixed analyzer transmission mode, survey scans were collected with a pass energy of 160 eV while high resolution scans were collected with a pass energy of 20 eV. All spectra were taken at surface normal unless otherwise indicated. High resolution scans of each region are summarized in the following table and are representative of all scans taken at those in those regions.

Table 2.1: XPS parameters of high resolution analysis

Element and Orbital	Step size (meV)	Dwell time (ms)	Number of Sweeps
C 1s	10	260	3 – 5
Si 2p	10	400	3 – 5
O 1s	50	330	3
S 2s	50	400	5 - 10

Peak fitting analysis of high resolution spectra was carried out using CasaXPS software. A Shirley baseline was used with blended Gaussian-Lorentzian peaks to fit the spectra. The peaks consisted of an 80% Gaussian contribution and a 20% Lorentzian contribution. Detailed peak fittings covered in subsequent chapters.

2.3.2 – Electrical Measurements

Electrical measurements of silicon microwires were performed using a standard probestation with a B4500 parameter analyzer (Agilent). Tungsten probes with a diameter of

2 μm were used to make ohmic contact to the wires. Pressure was applied using either manual probe manipulators or by miBot micro/nanomanipulators (Imina Technologies) in an effort to exceed 11 $\text{mN}\cdot\mu\text{m}^{-2}$.³⁹⁻⁴² This amount of applied pressure changes the interaction between the silicon microwires and the tungsten probes creating a low resistance, ohmic contact to the microwires. A small corner of the microwire array would be scraped with a razor blade to remove a small amount of silicon microwires from the substrate. Once removed, they were carefully placed in a small vial where acetonitrile would be added to suspend them. The concentration of microwires in the suspension is not known, however the amount was visible by eye before the acetonitrile was added. In addition, the suspension was required to be sufficiently dilute to prevent multiple microwires from adhering to one another. This could be achieved by spotting a small amount (<10 μL) of the suspension on a glass slide and observing the spot under the microscope. If the suspension was too concentrated, a large amount of the microwires would be adhered to one another and would require more solvent to be added; if the suspension was too dilute, there would be very few microwires observed and some of the solvent could be boiled off to make the suspension more concentrated.

Electrical resistivity of silicon microwires is determined using a direct – contact technique that yields resistance measurements at various probe separations along individual wires.³⁹⁻⁴³ Resistance measurements are obtained by placing the tungsten probe at the end of a microwire and decreasing or increasing the separation distance. Resistivity and dopant density are obtained from the slope of the resistance – length curves and the contact resistance of the probes are obtained from the y intercept.

Evaluating the electrical nature of the silicon microwire/polymer junctions requires a model unit cell device structure to be created. Using the same manipulators highlighted in the previous

section, a single microwire can be picked up and put into contact with a small strip of polymer. The polymer used in these studies was poly(3,4 – ethylenedioxythiophene)/polystyrenesulfonate or PEDOT:PSS (Heraeus Clevios FE T; 3.5 wt% in water) because of its promising electrical conductivity and low visible light absorptivity that may be utilized for the membrane in an artificial photosynthetic device.¹⁷ A prepositioned set of clear tape or parafilm was used to define a 1 x 3 cm area on a glass slide (3.5 cm x 3 cm) and the PEDOT:PSS was slowly added to this area until it was covered. The glass slide was spun between 500 and 1500 rpm for 10 – 30 seconds respectively depending on the thickness desired for the analysis. Thicker polymer layers would be spun at slower spin rates in an attempt to keep the polymer wet, affording more time to embed the microwires into the polymer film. At 200x magnification, the silicon microwires are easily visible and can be put into contact with the PEDOT:PSS film. Approximately 10 – 20 μm of the silicon microwires are embedded into the polymer film and transferred to the vacuum oven to dry at 110°C for 30 minutes.

After the polymer film has dried, 3 circular pads (1 cm diameter; 3 cm center to center) of Ag or Au are deposited onto the polymer to create a soft contact between the tungsten probe and the polymer. I – V characterization of the junction is carried out by making ohmic contact to the microwire with the tungsten probe as before and measuring the electrical resistance through the microwire/polymer circuit. I – V tests between the pads are taken before any measurement of the junction is carried out. Polymer contribution to the total resistance should not exceed 1%; however, in the case that it does, the polymer and wire resistances are removed from the total to evaluate the junction. Figure 2.4 shows the electrical characterization setup of an individual wire within a single unit cell of a possible device.

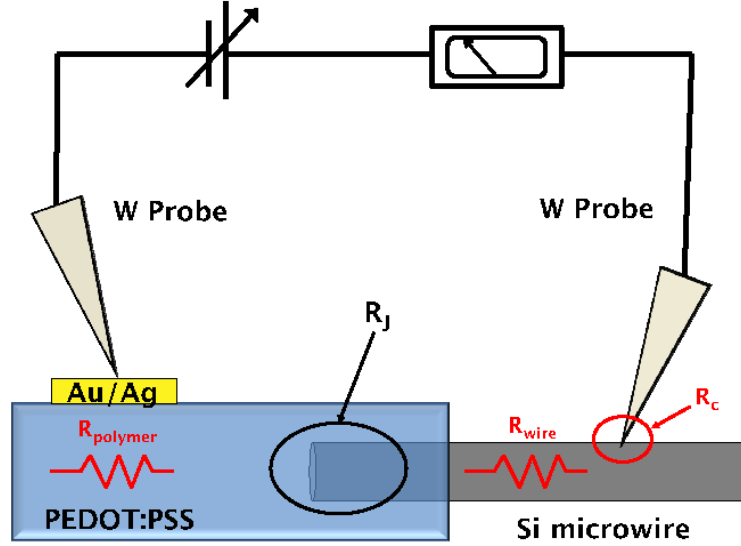


Figure 2.4: Single junction measurement of silicon microwire in contact with PEDOT:PSS. A full unit cell of a model device would have a p – type wire on one side of the PEDOT:PSS membrane and an n – type wire on the opposite side. R_{wire} is the slope of the resistance versus length measurement and the intercept is R_c .

The unit cell circuit for the characterization of the junction is as follows:

$$R_{total} = R_{polymer} + R_{wire} + R_{J,n} + R_{J,p} + R_c \quad (2.3)$$

R_c is the resistance associated with making contact with the tungsten probes. This value is obtained by linear extrapolation of the 2 point resistivity measurement of the microwires to the y – axis where the distance between probes is zero. Half of the extrapolated value is R_c , because the contacts are made by two probes. Microwires are covered with a small amount of polymer before baking to ensure good intimate contact between the two materials. Images of the junction formation and electrical setup are provided in Figure 2.5. Figure 2.5b illustrates a typical junction formed with PEDOT:PSS with Si microwire embedded in the membrane. The wire is covered completely at the junction and ohmic contact is made at the free end of the wire.

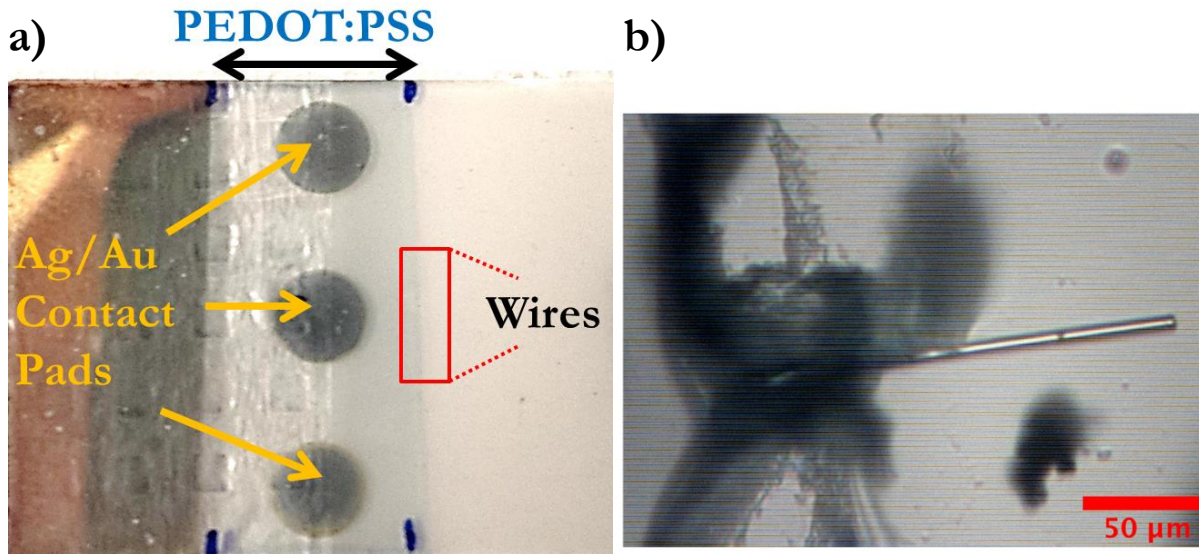


Figure 4.5: a) Image of electrical junction characterization setup. The pads used in this image are Ag. b) Light microscope image of junction formed between Si microwire and PEDOT:PSS film at 200x. The scale bar shows 50 μm.

Chapter 3: Improving the Characteristics of Silicon Microwire/p-type Conducting Polymer Junctions for Artificial Photosynthetic Devices

3.1 – Introduction

Photoelectrochemical splitting of water is a highly desirable alternative to the consumption of fossil fuels to meet the growing need for energy without additional impact on the environment. Integration of photoabsorbers and catalysts supported by a membrane mimics the natural photosynthetic process of harnessing light energy and converting it into a usable fuel, bringing each individual component in close proximity to one another. Splitting water into hydrogen and oxygen requires 1.23V of energy to drive the reactions and additional driving force will be required to compensate for losses associated with catalyst overpotential and electrical losses.^{12, 44, 45} High – aspect ratio silicon microwires have been proposed as the photoabsorbers in a model system, and have recently been characterized with p and n – type wires embedded, in series, in a polymer membrane.³⁹⁻⁴¹ PEDOT:PSS/Nafion blends are used as the membrane material because of the high electronic and ionic conductivity, as well as its minimal contribution to light absorption in the visible range of the spectrum.¹⁷

Significant solar energy to fuel conversion efficiency has been predicted for integrated photoelectrochemical water splitting devices by evaluating individual components.⁴⁶⁻⁴⁸ However, a tandem device similar to Figure 1.8 will require formation of a model structure to provide insight into the behaviour of a real integrated device. Analysis of charge dissipation is difficult to quantify by summing the electrical loss contribution from individual components, and usually requires characterization of a representative model. The complete electrical circuit, including solid state junctions formed between microwires and the membrane, is illustrated in Figure 3.1.

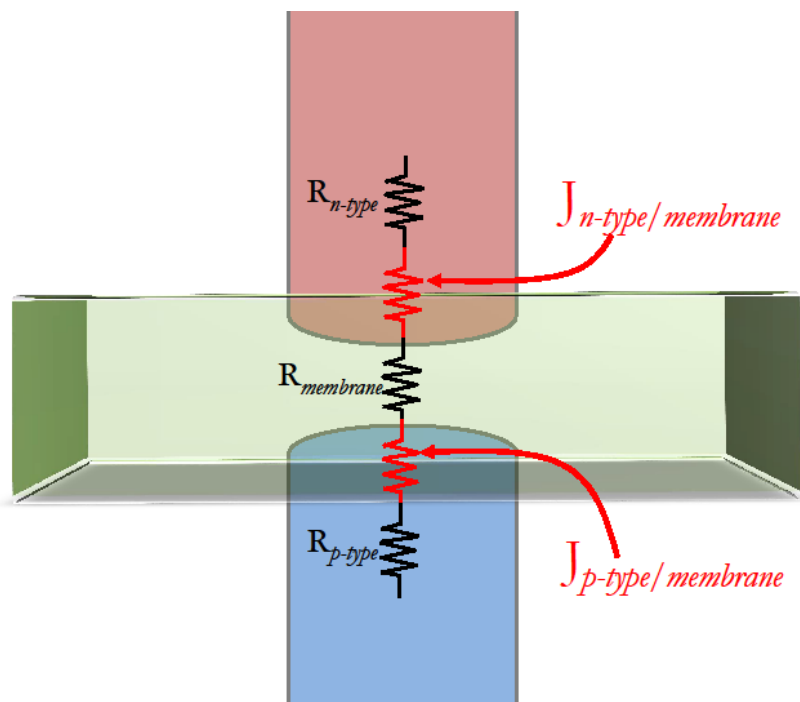


Figure 3.1: Unit cell of model solar fuels device with electrical contributions to the total circuit highlighted. The n-type microwire and p-type microwire junctions are highlighted as the majority contributions to the iR loss in the system.

Electrical characterization of a model device has shown electrical loss contributions from the membrane and microwires are small compared to the junctions between n-type Si/PEDOT:PSS and p-type Si/PEDOT:PSS.^{41, 43} These solid state junctions are considered the limiting resistive components of the system. The n-type Si/PEDOT:PSS junction was observed, in particular, to contribute a large loss to the overall system under solar operating conditions.^{39, 41, 43}

The formation of a thin, insulating silicon oxide layer slows charge transport across the interface between the microwire and membrane. Removal of this layer can be achieved using hydrofluoric acid, yielding a metastable, H-terminated surface under ambient and aqueous conditions where operation of a solar fuel device would occur. Passivation of the Si surface using a methyl group can prevent the formation of the oxide layer; however, recent studies have observed high resistances associated with the n-Si/PEDOT:PSS junction under solar operating

conditions.^{39-41, 43} In order to lower this resistance, the n-type Si/PEDOT:PSS junction was modified using two different methods. The first involves changing the energy band configuration of the n-type Si/PEDOT:PSS interface by introducing a higher dopant density near the contacting region. This region, located at the base of the microwire, is predicted to lower the junction resistance enough to maintain a high efficiency in a model solar fuels device.

The second method is modification of the surface group used to block the formation of the oxide layer. PEDOT is a modified thiophene moiety with an ethylene dioxide group bridging the β – positions of the thiophene ring. Functionalizing the surface of silicon with thiophene is expected to provide a more intimate contact between the surface and the PEDOT:PSS polymer. The modification to the interface in this manner may also facilitate more efficient charge transfer, leading to a lower electrical loss at the junction because of the similarity of the PEDOT:PSS and thiophene functionalized on the surface.

3.2 – Experimental

Arrays of silicon microwires were grown using chemical-vapor deposition (CVD) facilitated by the vapour–liquid–solid (VLS) growth process. Substrate preparation and growth procedures from the previous chapter are followed except for the following exceptions. The copper-catalyzed growth of arrays of highly doped n^+ -Si microwires was performed with uniform doping concentrations of $\sim 10^{19} \text{ cm}^{-3}$ along the 80 – 85 μm length of the microwires. Modified, n^+/n , microwires were grown with a highly doped base of $\sim 20\text{-}30 \mu\text{m}$ in length with a total microwire length of $\sim 60 \mu\text{m}$. The lengths of the highly doped and low-doped regions, respectively, were estimated by controlling the time of exposure to each flow rate of phosphine. The dopant concentration in the highly doped region was $\sim 10^{19} \text{ cm}^{-3}$, while the dopant

concentration in the low-doped region was $\sim 10^{17} - 10^{18} \text{ cm}^{-3}$. The Cu growth catalyst was removed using a 1:1:6 (v/v/v) HCl (27%v): H₂O₂ (30%v): H₂O (Millipore, 18.2 M Ω resistivity) RCA2 clean prior to surface treatment.

p-type microwires were grown with a consistent dopant profile along the length of the wire and had similar dopant densities to the low – doped n – type regions, $\sim 10^{17} \text{ cm}^{-3}$. Microwires grown with p-type dopants were 60 – 120 μm in length.

Microwire arrays that contained the metal catalyst on the tops of the wires were grown in a similar manner. The highly doped microwire bases, with dopant concentrations of $\sim 10^{19} \text{ cm}^{-3}$, were 10 – 20 μm in length with the remainder of the 60 μm long microwire having a dopant concentration of $\sim 10^{18} \text{ cm}^{-3}$. Microwires grown using Au as the growth catalyst were $\sim 120 \mu\text{m}$ in length with an $\sim 40 \mu\text{m}$ long highly doped base region.

All of the silicon microwire arrays were then functionalized with either methyl or thiophene groups using a two–step chlorination/alkylation procedure that exploits the kinetic stability of the Si-C surface bonding to minimize oxidation of the resulting Si surface.^{31, 32, 35, 37, 49, 50} Microwires functionalized with thiophene groups were placed into 2 – thienyllithium solution (1M in THF/hexanes; Sigma Aldrich). Thiophene surfaces also underwent a second functionalization with methyl groups in an effort to terminate any unreacted sites on the microwire surface. Reaction times with thiophene were varied to investigate whether the surface is fully terminated. All methyl reactions were allowed to proceed for a minimum of 3 h at 60 °C before removal of the array from the solution and subsequent rinsing in THF and methanol. After removal from the glove box, the arrays were washed sequentially in methanol, acetonitrile, isopropanol and water, before being stored under N₂(g).

Microwires were removed from the growth substrate by scraping a corner of the sample using a razor blade. A suspension of microwires was made using CH₃CN, and ~10 μL was drop cast on a glass substrate. The highly doped regions of the microwire were identified by obtaining resistance measurements at each end of the microwire using a separation length of 10 μm for the tungsten probes.

3.2.1 - Resistance Measurements to Characterize Dopant Density

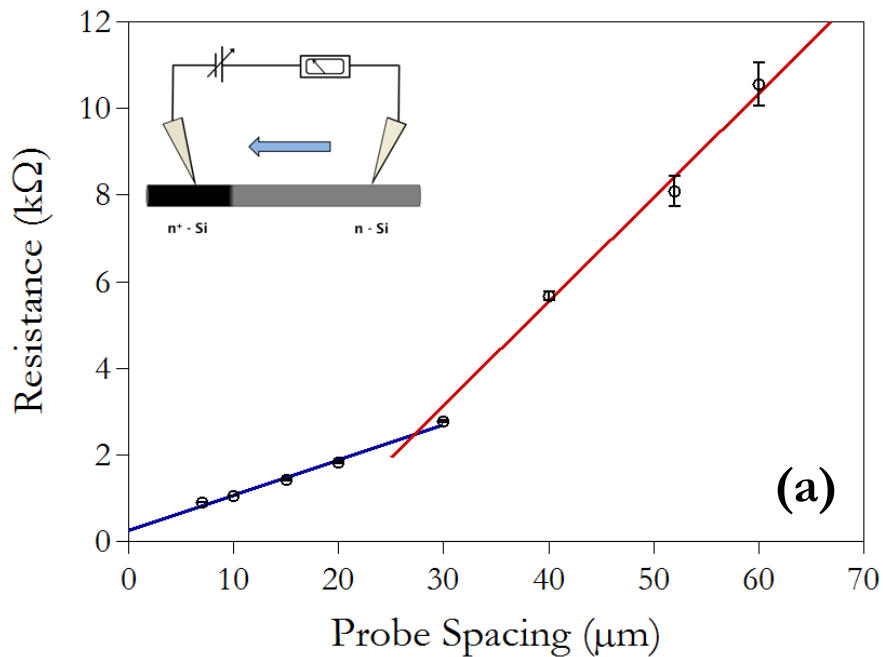
Resistance measurements were obtained by placing the tungsten probe at one end of the microwire and then increasing or decreasing the separation distance to the second tungsten probe. Repetition of the measurement at various locations along the microwire length provided confirmation of the dopant concentration in the high- and low-doped regions and allowed for location of the transition between the doping regions.

3.3 – Results

3.3.1 - Electrical Characterization of n⁺/n Silicon Microwires

Direct-contact characterization of the Si microwires using W probes enabled bulk resistivity measurements and allowed electrical characterization of an integrated microwire/polymer model system (Figure 3.1). The differential doping of the semiconductor microwires was also characterized, and heavily-doped (n⁺) regions were distinguished from lower-doped (n) regions by moving the tungsten probes along the microwire and obtaining electrical measurements at each position (Figure 3.2). As the mobile probe was moved from an n⁺ region to an n region, the change in resistivity was clearly detectable (Figure 3.2a). The data were validated by moving the probe in the opposite direction, from an n region to an n⁺ region (Figure 3.2b).

A linear fit to the resistance data for each region of distinct dopant density was used to extract the local bulk resistivity and to estimate the contact resistance between the W probes and the Si microwire. Extrapolation of the regression lines to an intersection provided an estimation of the transition point between the n^+ and n doped regions. From Figure 3.2, the length of the n^+ region when moving from n to n^+ was calculated to be $26 \pm 5 \mu\text{m}$, while the length of the n^+ region when moving from n^+ to n was calculated to be $18 \pm 5 \mu\text{m}$. The smallest probe spacing that permitted reproducible I - V measurements (was $5 \mu\text{m}$), however the linearity of the slope suggests a ~~that smaller much lower~~ spacings can be achieved. The limitations of the measurement may be in the ability to observe the probe tips and their spacing, and, as such, Hhigher magnifications and different probe angles may be required to gain a better understanding of the error in the spacing. With this in mind, the error in the spacing is estimated to be $1 \mu\text{m}$.



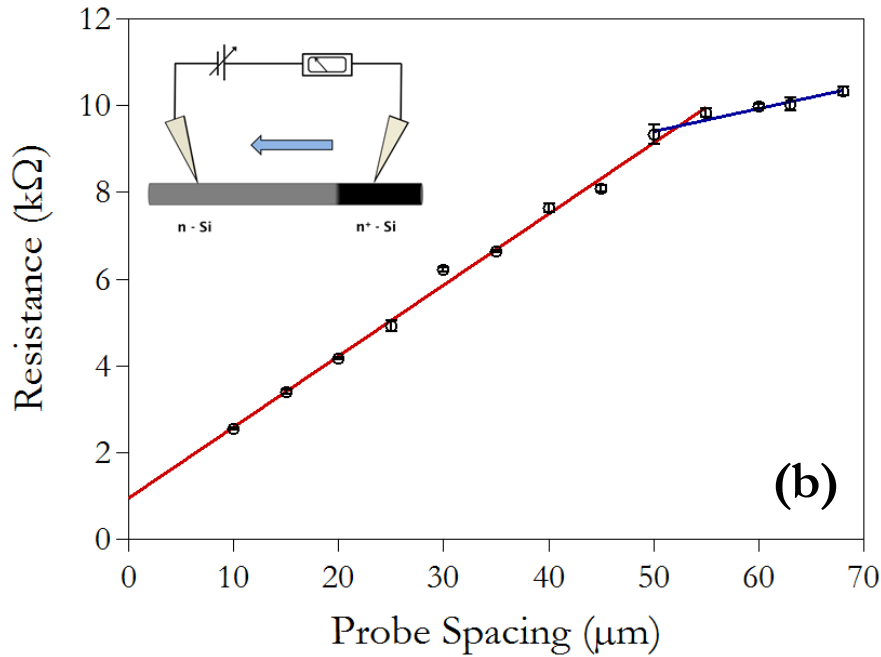


Figure 3.2: Contact resistance measurements of methylated highly doped base (n^+n) Si microwires. Three independent measurements were performed at each individual point along the wire, and measurements were conducted by movement of the W probes in both directions along the Si microwire. (a) movement of the mobile probe from the n (top) to n^+ (base) direction and (b) movement of the mobile probe from the n^+ (base) to n (top) direction. The linearity of the data reflects the uniformity of the dopant concentration over the length scales considered throughout the regions investigated.

The slope and intercept of the regression lines associated with each region of the resistance data were used to estimate the dopant concentration and the contact resistance of the W probes (intercept $\approx 2R_c$) with the values summarized in Table 3.1.

Table 3.1: Summary of the data relevant to the direct-contact technique with W probes on Si microwires.

	n^+	n^+/n (high doped contact)	n/n^+ (low doped contact)
Length and Diameter (μm)	80,1.5	60,1.5	70,1.5
Intercept ($\text{k}\Omega$) $\pm 10\%$	0.1	0.4	1.0
Slope ($\text{k}\Omega/\mu\text{m}$) $\pm 10\%$	n^+ 0.011 n -	0.071 0.25	0.051 0.16
Resistivity ($\Omega\cdot\text{cm}$) $\pm 10\%$	n^+ 0.002 n -	0.013 0.044	0.009 0.029
Dopant Concentration (cm^{-3})	n^+ $\sim 4 \times 10^{19}$ n -	$\sim 3 \times 10^{18}$ $\sim 3 \times 10^{17}$	$\sim 6 \times 10^{18}$ $\sim 8 \times 10^{17}$

The intercept was taken to represent the sum of the individual contact resistances of the W probes with the microwire. A minimum of 4 wires from a single wire array were tested.

The linearity of the slope on either side of the transition between the n^+ and n regions indicated that the dopant concentration was uniform within each region over the length scales under consideration (μm). The dopant concentrations calculated for each region were consistent with the values targeted during fabrication as well as in previous reports using similar wire growth procedures.^{39, 40} The absolute resistance of each homogeneously doped microwire was estimated using the slope of the line and the full length of the wire. For the n^+n -doped microwires, the resistance was calculated using the slope of the n region, and is considered an upper bound on the actual absolute resistance.

3.3.2 - Surface Functionalization of Silicon Microwires

Another possible route to address the high resistance is by modifying the group attached to the surface. Stability of the microwire surface to oxidation is still required for efficient electron transport throughout the device and substitution of methyl for a thiophene group should not increase the oxidation of the surface. Nucleophilic attack of the surface of silicon can be achieved using a thienyllithium moiety and a Si – C bond is formed at the α – carbon site of the thiophene ring.

Complete coverage of the microwire surface is desirable to maximize resistance to oxidation. Previous work on functionalization of planar silicon report surface coverage of the samples,^{33, 35, 38, 49, 51, 52} however, surface coverage of silicon microwires has not been investigated in detail. Chapter 4 will begin to address characterizing surface coverage of microwires but in this work, characteristic XPS peaks of surface bound species are normalized to the bulk silicon peak. Thiophene functionalized surfaces have a

characteristic S 2s peak in the survey spectrum, as observed in Figure 3.3a. High resolution spectra in Figure 3.3b and 3.3c are utilized to perform quantitative analysis on the amount of thiophene present on the surface.

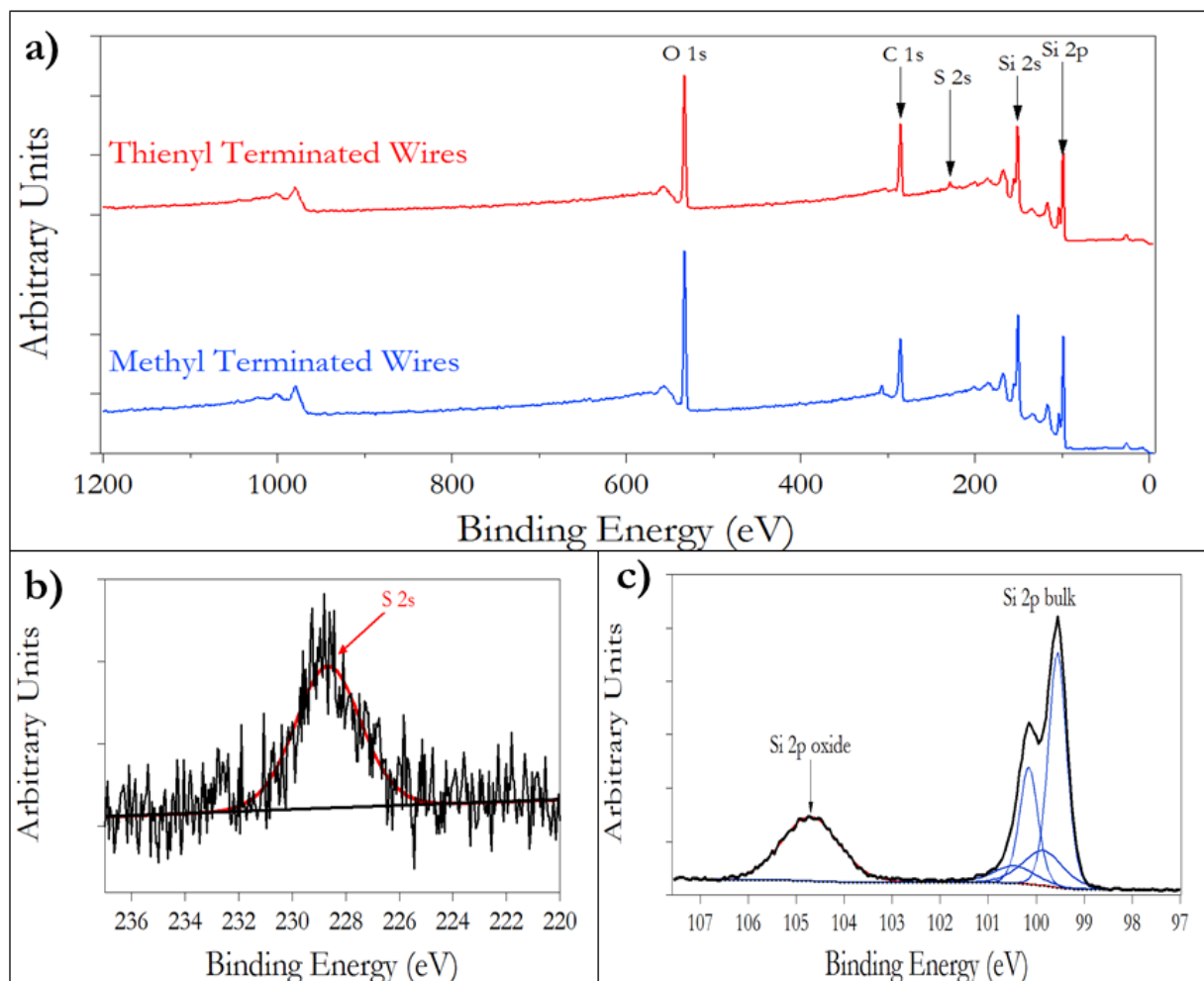


Figure 3.3: X-ray photoelectron spectra of surface functionalized silicon microwire arrays a) Survey spectra with comparison between methyl terminated wires and thiophene terminated wires b) High resolution spectra of the S 2s region c) High resolution spectra of the Si 2p region representative of functionalized silicon microwires.

Peak fitting of the Si 2p spectra in Figure 3.3c uses a Shirley algorithm to define a background in the spectrum. The Shirley background takes into account inelastic scattering within the bulk of the sample, manifested as an increase in baseline intensity at higher binding energies within the spectra.^{53, 54} The bulk region is fit with two spin – split contributions of Si^{3/2}

and $\text{Si}^{1/2}$ peaks while the oxide region is fit with a single Gaussian function. Separation between spin – split pairs are constrained to 0.6 eV and full width half maximum (FWHM) values are set equal for each pair. Multiple silicon oxide contributions begin to appear under the Si^{4+} region at ~103 eV after the sample has been left in ambient conditions for over a month and fitting all contributions unnecessarily complicates the fit. Silicon microwires, while still attached to the growth substrate, have an unusual oxide region in the Si 2p high resolution spectrum. A large oxide contribution at 105 eV convolutes peak fitting in that region. Signal from this oxide peak likely originates from the thick thermal oxide that remains at the base of the microwires after growth. Careful analysis of the oxide region is required and FWHM values are constrained to values less than 1.5 eV.

Background subtraction of the S 2s region is completed using a linear background instead of a Shirley background because the surface bound species would not have a significant amount of inelastic scattering associated with S 2s- photoelectrons escaping from deeper within the sample. In addition, the intensity at higher binding energy is very similar to the lower binding energy and would not be sufficiently described by using the Shirley background.^{53, 54} The S 2s area is then normalized to the Si bulk area in the Si 2p spectrum to quantify the amount of thiophene on the surface of the silicon microwires.

Saturation of the S 2s to Si 2p bulk signal ratio will indicate that the surface is effectively covered. Every wire has a finite number of sites available for functionalization, and maximum coverage of those sites is dependent on the size of the molecule. In Figure 3.4, the surface is completely covered after 60 minutes of reaction time in the thienyllithium solution. Oxidation after 3 months in ambient conditions is compared between samples that were functionalized

once, with a thiophene group and those that underwent a subsequent functionalized step with a methyl group.

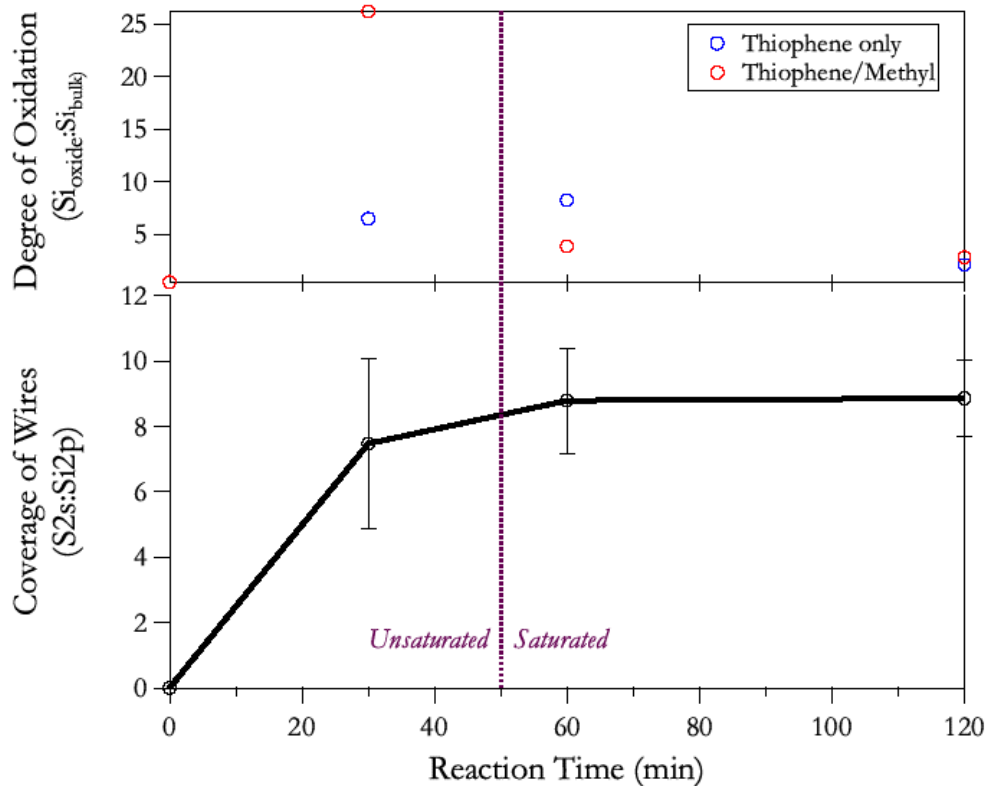


Figure 3.4: Complete coverage of the microwire surface with thiophene groups. The top of the figure shows the oxidation after 3 months in ambient conditions while the bottom shows coverage of the wires. A methylated microwire is the zero point for reaction time and degree of oxidation. Coverage and degree of oxidation are expressed as a percent of the Si 2p bulk peak for clarity.

A second functionalization step is added to functionalize any unreacted dangling bonds present on the silicon microwires. Steric interactions between molecules caused by the surface structure and size of the thiophene may hinder complete functionalization. Figure 3.4 indicates that secondary methylation has little effect on the long term oxidation of the surface; however the level of oxidation does decrease as the microwire surface approaches complete passivation.

3.3.3 - Electrical Characterization of the PEDOT:PSS/Si Microwire Junction

3.3.3.1 - Changes in Resistivity and Metal Contacts

In an integrated photoelectrochemical device that incorporates Si microwires as the photoabsorbing material, the junction between the n-Si microwire and PEDOT:PSS membrane has been shown to be the limiting resistive component in the system.^{40, 41} The direct-contact technique discussed above can also be utilized to characterize the junction.^{17,19} As shown in Figure 3.5, the $I-V$ behavior of the Si microwire/PEDOT-PSS junction was symmetric for the uniform n⁺ microwire ($N_D = 4 \times 10^{19} \text{ cm}^{-3}$) as well as for the n⁺ doped ($\sim 5 \times 10^{18} \text{ cm}^{-3}$) region of an n⁺n-Si microwire. This electrical behaviour is contrasted with the rectifying behavior observed for the junction between PEDOT-PSS and the n-type region ($N_D \approx 5 \times 10^{17} \text{ cm}^{-3}$) within the n⁺n-Si microwires.

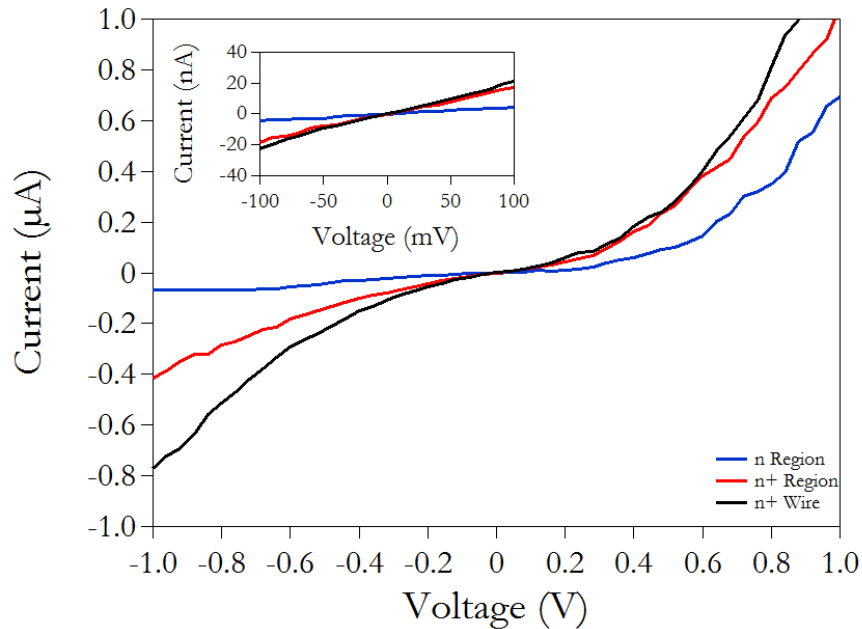


Figure 3.5: $I-V$ characteristics of methyl-terminated n-type Si microwires in contact with PEDOT:PSS. The low-doped end ($\sim 5 \times 10^{17} \text{ cm}^{-3}$) in contact with PEDOT:PSS was the only sample that exhibited a rectifying contact. For the highly doped region ($> 3 \times 10^{18} \text{ cm}^{-3}$) in contact with PEDOT:PSS, the $I-V$ behavior was symmetric. The inset shows the low-bias region relevant to Air Mass 1.5 G operating conditions.

The resistance of the Si microwire/PEDOT-PSS junction was calculated by considering all other resistive contributions, i.e. R_{polymer} , R_{wire} and R_c (Equation 2.3 and Figure 3.1) to the total measured resistance. The total resistance values were obtained from the linear portion of the $I-V$ data in the low bias region (-100 mV to 100 mV), representing the anticipated operating conditions of an artificial photosynthetic device under unconcentrated solar illumination.^{16,17,20} Complete absorption of photons with energy greater than the band gap of the Si microwires from sunlight incident normal to an array, with a 7 μm pitch, and with 1 Sun of AM 1.5 G solar irradiance, has been estimated to result in a maximum short-circuit photocurrent of ~ 20 nA per microwire.^{39, 41, 55} Hence, currents within this range of voltages include the 20 nA light-limited current associated with absorption of sunlight in Si microwires from 1 Sun of the global Air Mass 1.5 (AM 1.5 G) solar irradiance spectrum.^{21, 55, 56}

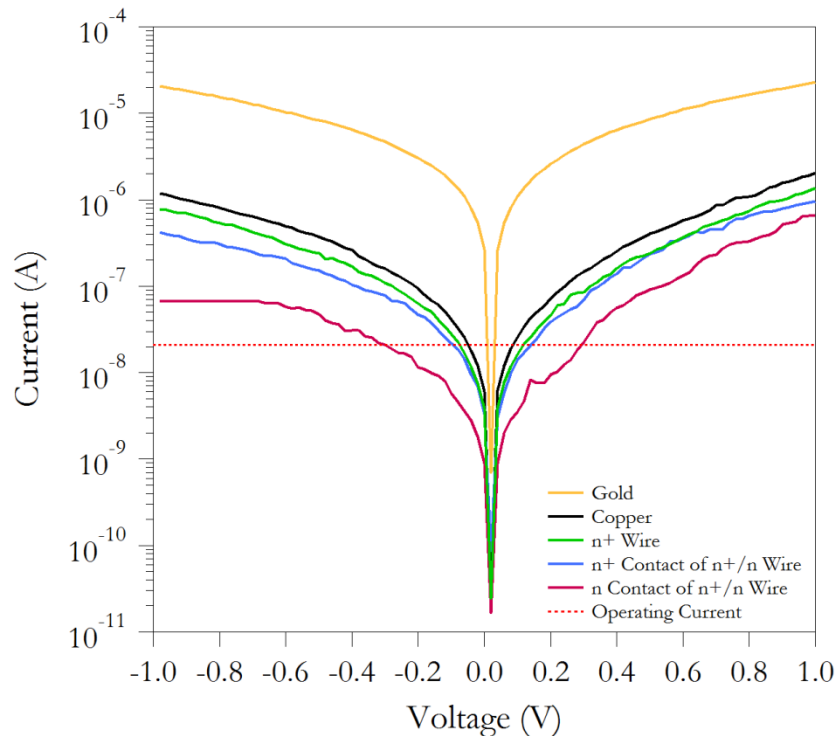


Figure 3.6: Semilog plot of operating current used to evaluate the iR losses for the different n-type Si microwires in contact with PEDOT:PSS. At 21 nA, the associated iR loss due to the junction between the highly doped Si microwire and PEDOT:PSS was 90 mV. The corresponding iR losses for the high-doped end and low-doped end of the n^+/n silicon microwire were 130 mV and 290 mV, respectively. Gold and copper catalysts that were left after surface functionalization produced iR losses of <10 mV and 50 mV, respectively.

The iR losses due to the junction between PEDOT-PSS and the Si microwire were 90 mV for the uniformly doped n⁺ microwire and were 130 mV and 290 mV for the high-doped and low-doped regions of the n⁺/n microwires, respectively.

The metal catalysts that remained from the microwire growth procedure were located on the tops of the Si microwires, and were also used to contact the PEDOT:PSS. These catalysts formed a junction between the low doped region of the Si microwire as well as the PEDOT:PSS. The copper catalysts exhibited ohmic *I-V* behavior with an iR loss of 50 mV. Gold catalysts exhibited ohmic *I-V* behavior with an iR loss of < 10 mV. The iR loss associated with the expected short-circuit current under AM 1.5 G illumination provides a figure-of-merit for how the electronic losses will affect the final device performance (Table 3.2).

Table 3.2: Summary of junction resistances of n-type silicon microwires in contact with PEDOT:PSS

	Diameter (μm)	Dopant Concentration (cm^{-3})	Junction Resistance ($\text{M}\Omega$)	iR drop observed (mV)
n⁺	1.5	$\sim 4 \times 10^{19}$	5.0 ± 0.2	90 ± 10
n⁺/n (high doped contact)	1.5	$\sim 5 \times 10^{18}$	6.0 ± 0.2	130 ± 10
n/n⁺ (low doped contact)	1.5	$\sim 6 \times 10^{17}$	21 ± 3	290 ± 50
Copper	1.0	$\sim 4 \times 10^{17}$	3 ± 1	50 ± 25
Gold	1.0	$\sim 6 \times 10^{17}$	0.05 ± 0.02	<10

Junction resistances reported are taken from the slope of the *I-V* curve in the +/- 100 mV range. The iR drop is reported at 21 nA. A minimum of 4 wires from the same wire array were tested. The gold iR drop was consistently lower than the limit of detection at 21 nA.

3.3.3.2 - Effects of Surface Functionalization

Reducing the junction resistance of the n – Si microwire/PEDOT:PSS contact can be achieved by increasing the bulk resistivity of the material in the contacting region

between the two materials. The control over this area is a great advantage if the junction resistance can be lowered enough to minimize the electrical loss. Decoupling the contact region from the remainder of the light absorber would not sacrifice photovoltaic performance to reduce iR contributions by optimizing the dopant density throughout the microwire. Saturation of the silicon microwire surface by another Si – C functional group has been achieved as illustrated in Figure 3.4. Resistance to oxidation is also maintained when using a thiophene group in place of a methyl.

The p – type/PEDOT:PSS and n – type/PEDOT:PSS junctions were also investigated. Changing the identity of the surface group will modify the interfacial alignment at the Si microwire/PEDOT:PSS junction and, as such, both p – type and n –type/PEDOT:PSS contacts are investigated. In the previous section, the p – type/PEDOT:PSS junction was not characterized because its contribution to the overall iR loss in comparison to the n – type/PEDOT:PSS junction was minimal.⁴¹

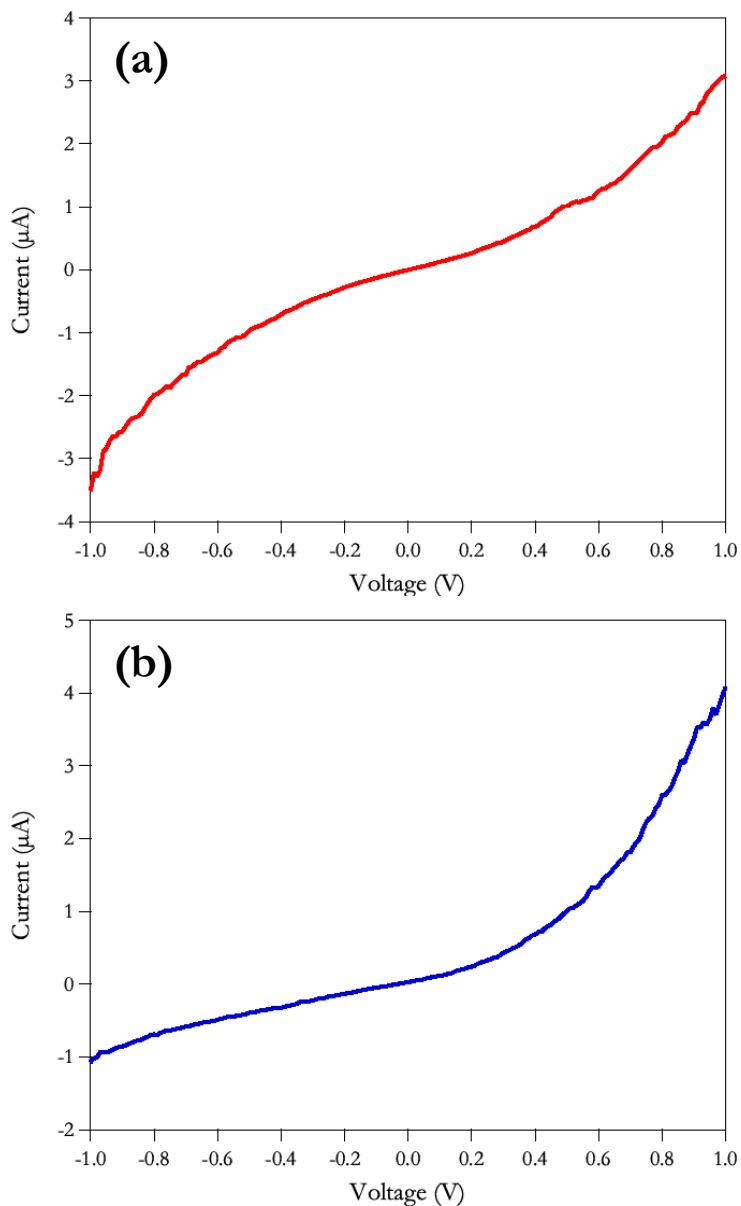


Figure 3.7: Current – Voltage curves of thiophene functionalized silicon microwires in contact with PEDOT:PSS. a) p – type wire curves indicate non – ideal ohmic behaviour and b) n –type wire curves indicate leaky diode behaviour

From Figure 3.7a, the junction behaviour of the thiophene terminated p-type Si/PEDOT:PSS junction preserves behaviour observed for methylated p-type Si/PEDOT:PSS wires.⁴¹ The junction resistance in the low bias region (-100 to 100 mV) that encompasses the light – limited current for thiophene terminated silicon microwires

is $810 \pm 50 \text{ k}\Omega$. Figure 3.7b shows the n – type thiophene terminates Si/PEDOT:PSS junction behaviour over the large bias voltage regime. This junction is expected to exhibit diode behaviour because of the large workfunction difference between the PEDOT:PSS ($\sim 5 \text{ eV}$) and n - Si ($N_D = 8 \times 10^{17} \text{ cm}^{-3}$, 4.14 eV). The behaviour observed in reverse bias shows a significant amount of current passing through the system that is inconsistent with diode behaviour. This behaviour is more consistent with a leaky diode and higher currents are observed in reverse bias as more thiophene is added to the surface. Figure 3.8 illustrates the increase in current in reverse bias with more thiophene on the surface. The junction resistance under the low bias conditions is $1300 \pm 500 \text{ k}\Omega$.

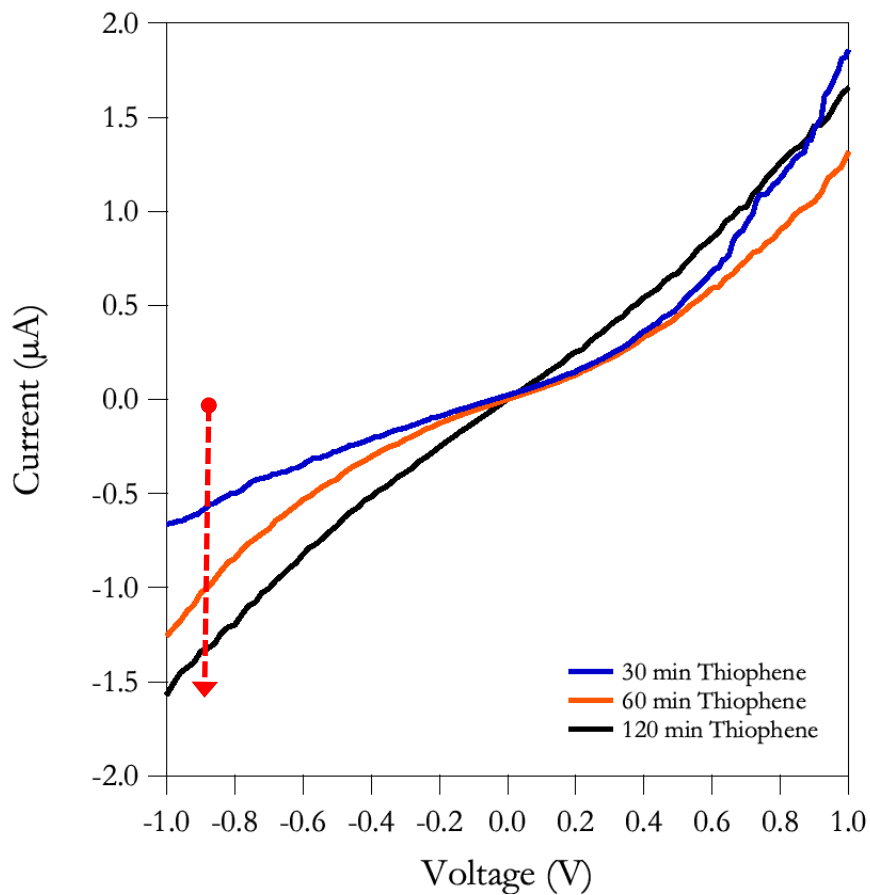


Figure 3.8: Addition of thiophene and its effect on junction resistance. Higher currents observed in reverse bias indicated by the arrow.

Surface saturation is considered to be complete after 60 minutes of reaction time in the 2 – thienyllithium solution based on the XPS characterization. Junction resistances and voltage drops are considered with respect to reaction time in Figure 3.9.

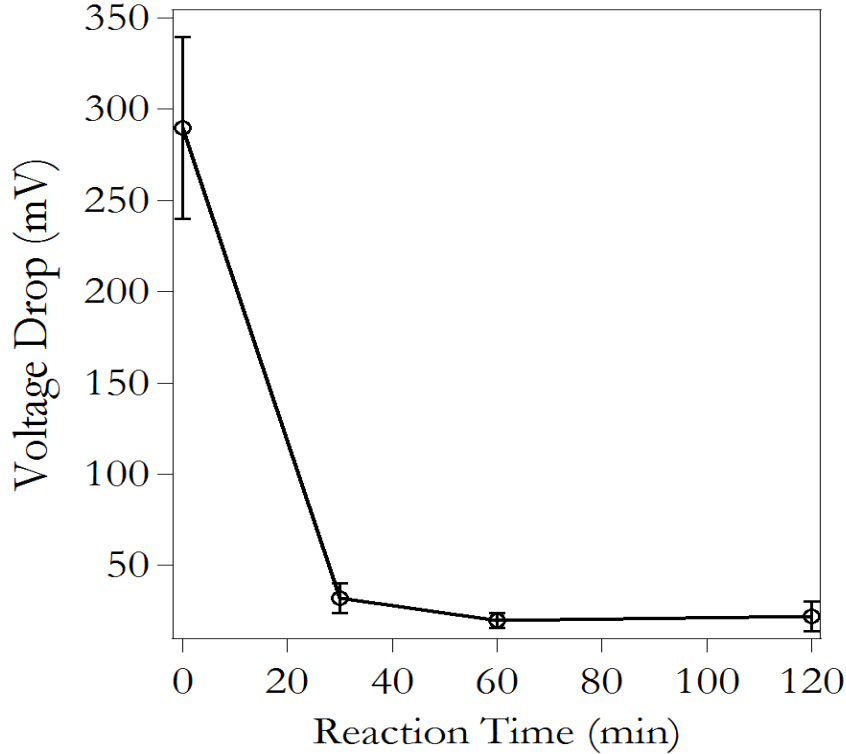


Figure 3.9: Junction voltage drops based on thiophene reaction time. The voltage drops are considered for n-type Si/PEDOT:PSS junction only under solar irradiation AM1.5 conditions. Zero reaction time is methylated n-Si microwires.

The voltage contribution of the n-Si/PEDOT:PSS contact is considerably reduced with the addition of thiophene to the surface. Junction resistances for n-Si microwires ($\sim 10^{17} \text{ cm}^{-3}$) decrease the iR contribution from 300 mV to 30 mV when changing the surface group from methyl to thiophene. Saturation of the junction resistance also occurs after a reaction time of 60 minutes where the value of the resistance is lowered to less than 1 M Ω .

Comparison of each strategy addressing the high junction resistance of the n – Si/PEDOT:PSS junction is illustrated in Figure 3.10. Quantifying the iR drop under solar operating condition shows a decrease in junction resistance between the two methods when compared to methylated n – doped Si. The thiophene decrease is much larger than only the inclusion of a highly doped region near the base. The iR contribution decreases from 300 mV for an n – doped contact to 100 mV to 30 mV when using n^+ - doped and thiophene terminated contact respectively.

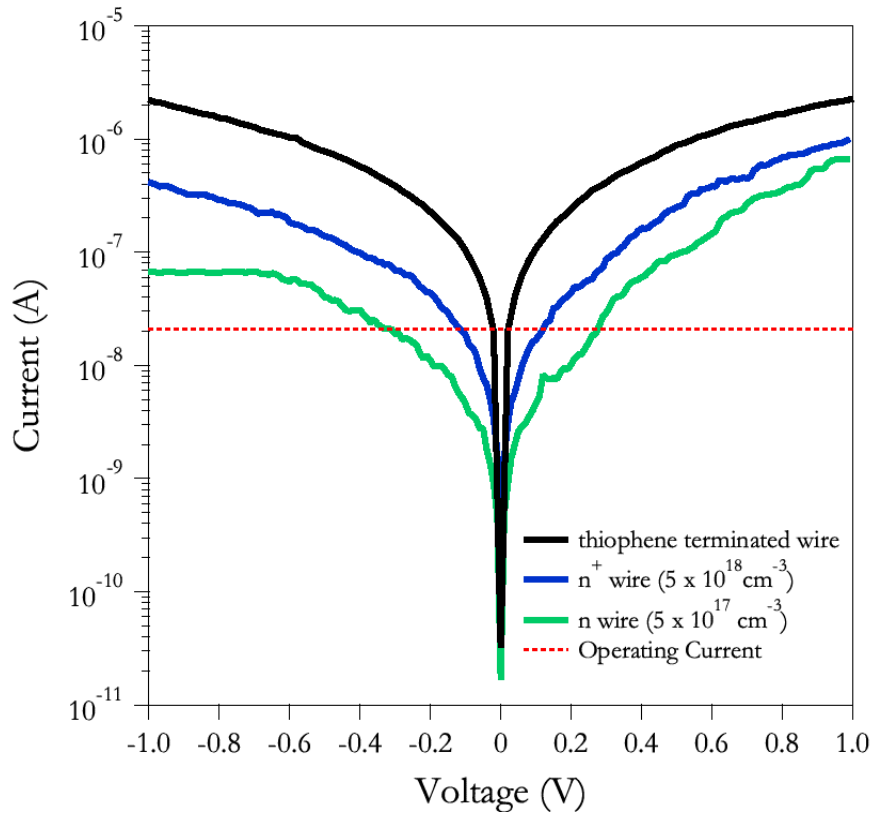


Figure 3.10: Comparison of thiophene terminated n – Si/PEDOT:PSS junctions with highly doped and low doped contacts. Operating currents of 20 nA are generated under light limited conditions and is represented by the horizontal red line.

A voltage drop of 100 and 30 mV constitutes a significant improvement to the electrical characteristics of the model device. The inclusion of the highly doped base to thiophene

terminated wires could also be investigated to lower the junction resistance further but was not characterized in this work.

3.4 - Discussion

3.4.1 - Electrical Behaviour of Differential Doping in Silicon Microwires

The location of the transition region between the n and n⁺ regions, identified *via* the direct-contact measurements, was limited by the error associated with physical manipulation of the probes and the tip diameter. A minimum probe spacing of 5 μm was required to obtain reliable electrical measurements and dopant densities. The concentration of electrically active dopant is dependent on the concentration used during the growth process,¹⁸ however the doping level within the microwires responds immediately to changes in dopant flow rate, due to diffusion in the Si-saturated VLS growth catalysts. Thus, an abrupt change in dopant density that could not be detected by this method is unlikely despite limitations such as probe size or minimum spacing.

3.4.2 - X – ray Photoelectron Characterization of Silicon Microwires

Characterization of the silicon microwire surface with XPS indicates saturation of the surface occurs after 60 minutes of reaction time. The S 2s peak is not ideal for quantification because of its low intensity compared to the S 2p peak. Unfortunately, silicon has phonon bands in the region where the S 2p peak normally appears and high intensity associated with these phonon bands makes quantification using the S 2p peak extremely difficult. Another possible avenue for surface coverage quantification is by using the Si – C peak in the C 1s spectra. Figure 3.11 shows the C 1s high resolution envelope used to quantify the surface coverages of silicon

microwires. Figure 3.11a clearly indicates the presence of a Si – C bond by the shifted peak in red. In contrast, Figure 3.11b shows the thiophene terminated silicon microwire C 1s window. The region between 283 and 285 eV, where the Si – C peak shift was observed for methyl, is no longer distinguishable from the remainder of the spectra and the peak fitting becomes more convoluted and difficult. Error in the fit also increases significantly and accuracy of surface coverage becomes questionable.

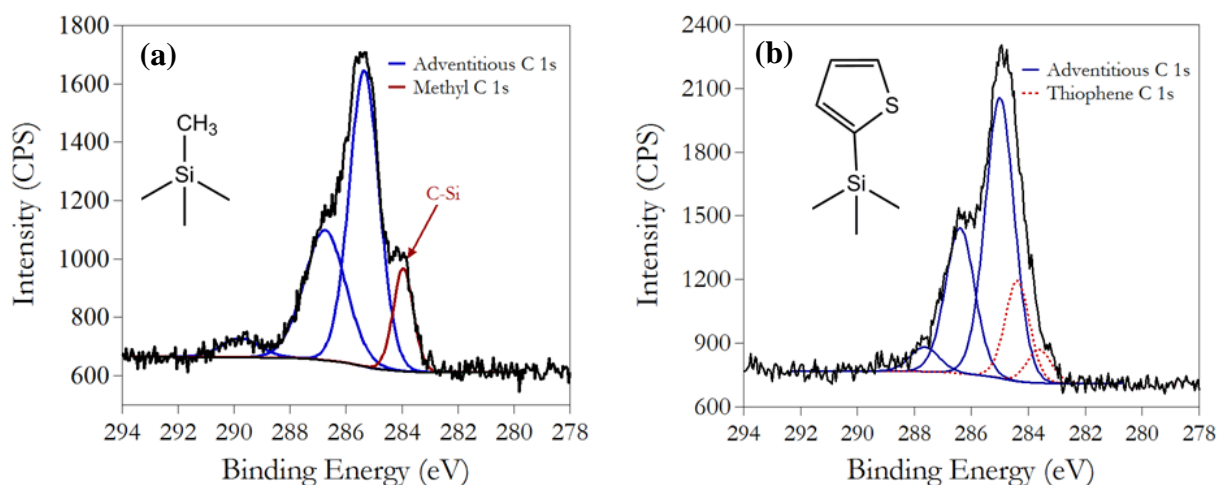


Figure 3.11: C 1s envelope of Si microwires. (a) methyl terminated wires show a distinct shift in the Si – C bond to the surface (b) thiophene terminated Si – C bond is convoluted, with multiple carbon contributions near the Si – C binding energy that reduces the accuracy for quantification of surface coverage.

The C 1s spectrum for thiophene terminated microwires becomes more convoluted because of the increase in aromatic character in the system attached to the surface. In addition, the C – S bond of the thiophene ring creates a peak at 285.3 eV, increasing the full width half max for the peaks around 285 eV.⁵⁷ The peak model in Figure 3.11a indicates four different peaks with two noteworthy chemical species. The blue peaks are characteristic of adventitious species on the surface. These include C – O, C=O, C – C and aromatic peaks whereas the red peak represents the Si – C bond to the surface. In Figure 3.11b, the adventitious species are also highlighted in

blue and a second red contribution is added to the fit. This represents a shifted aromatic peak or possibly attenuation of the adventitious species, widening the adventitious contribution to the spectrum. Difficulty in obtaining a reliable peak fit in the C 1s spectra is why the low intensity S 2s peak is utilized for quantification of the surface species.

Saturation of the surface bound thiophene species can be followed using the S 2s: Si 2p_{bulk} ratio. The ratio in these studies is expressed as a percent for clarity. After the 60 minute reaction time the ratio saturates and no longer increases. Additionally, the error in the measurement decreases with reaction time indicating the variability of the surface coverage decreases with longer reaction times. Oxide formation under to ambient conditions is also observed in Figure 3.4. In general, for all species, the degree of oxidation after a period of 3 months decreases when more of the surface becomes functionalized with the thiophene group. The S 2s region shows little decrease in intensity over that time suggesting the surface bound thiophene unit is not removed by the oxidation.

Variability in the degree of oxidation may be due to the large oxide peak at ~105 eV. Analysis in the presence of this large oxide peak will lower the accuracy despite the addition of numerous constraints to the model. Removal of this peak from the analysis without compromising the signal from the microwires, would be advantageous in order to increase the accuracy.

3.4.3 - Junction Behavior of Si Microwires in Contact with PEDOT:PSS

3.4.3.1 - n⁺/n contribution

The rectifying contact in the n-Si microwire/PEDOT:PSS devices is attributable to a mismatch in the Fermi levels between the high-work-function PEDOT:PSS and the low-work-

function n-type Si.^{16, 41} Utilization of the n^+ base for the Si/PEDOT:PSS contact altered the balance of charge-transfer mechanisms across the junction from thermionic emission to tunnelling, shifting the behavior from rectifying towards a more symmetric I - V response. The observed behavior was not perfectly ohmic, but in theory such could be obtained by additional increases in the concentration of electrically active dopants. The junction behavior can be evaluated over a large bias region (-1 to 1 V), however, the low bias region (-100 mV to 100 mV) provides the most relevant perspective for the operational photocurrent under unconcentrated AM 1.5 G illumination conditions.

The junction between PEDOT:PSS and the n^+ region of Si microwires with uniformly high doping levels, or between PEDOT:PSS and the n^+ region of Si microwires with an n^+/n microwire contact, exhibited a resistance of 5 M Ω and 6 M Ω , respectively. The n-type region contact to PEDOT:PSS exhibited a junction resistance of 21 M Ω . Inclusion of the n^+ base to the microwire/polymer contact decreased the n^+ -Si/PEDOT:PSS junction resistance by $\sim 25\%$, however the resulting resistance value is still well above a value needed to produce a proposed electrical iR loss limit of < 10 mV for an integrated artificial photosynthetic device.⁴¹ Fabrication of n^+/n silicon microwires with n^+ region dopant concentrations in the mid - 10^{20} cm⁻³ range could be considered. However, the dopant concentration is constrained by the saturation point in Si, beyond which no increase occurs in the conductivity of the material associated with an increased dopant concentration.^{58, 59} The dopant densities in the present work are within an order of magnitude of this limit. On the basis of these measurements, a junction resistance (R_J) as small as ~ 1 M Ω might be attainable through increased doping, but such a value of R_J would still lead to an iR drop of 21 mV, above the proposed limit, indicating that other means of addressing the high junction resistances are desirable.

A 25% efficient solar cell made entirely of crystalline silicon has been shown to yield an open-circuit voltage (V_{oc}) of 706 mV.⁵⁵ When operated under AM 1.5 G illumination conditions, Si microwire-based photovoltaics have been shown to display V_{oc} values that are within ~80% of this value.^{21, 60} The iR losses associated with the junction between the Si microwire and PEDOT:PSS, as a percentage of V_{oc} , correspond to 12.7% for the uniformly doped n^+ microwire, 18.4% for the highly doped contact, and 41.1% for the low-doped contact. An iR loss equivalent to 50% of V_{oc} would be extremely detrimental to the overall performance of the device; however, the addition of the n^+ base to the system reduces this loss substantially.

3.4.3.2 - Metal catalysts

Cu contacts to n-type Si are reported to exhibit rectifying behavior, however the temperatures at which the microwire growth process occurs are higher than the eutectic temperature of Cu with Si.⁶¹ The formation of a Si/Cu eutectic provides the appropriate contact for a less resistive junction, and Cu silicide would not be present at the contacting interface.^{62, 63} Au is expected to produce an excellent ohmic contact to Si, with minimal Au silicide formation during the growth process. Au is not preferred for use with Si microwires because of the high mobility of Au, the difficulty of extracting all Au-containing species incorporated in the wire itself, and Au acts as a recombination center in Si.^{22, 64, 65} The resistance data for the Au/Si microwire junction indicate that the proposed iR loss benchmarks are attainable with Au as a contact, however the presence of other recombination pathways associated with the presence of the Au may lead to lower overall efficiencies for a full microwire-based artificial photosynthesis system. These recombination pathways are the main motivating factors for the substitution of Cu for Au as a catalyst for microwire growth.²⁰

The diameters of the metal-capped Si microwires were 0.5 μm smaller than the diameters of the other Si microwires evaluated in this study. The contact resistance is inversely proportional to the contact area, and thus the junction resistance of the smaller microwires is expected to increase two-fold. However this increase was not observed for the Cu and Au contacts, indicating that the interface between the microwire and the polymer has a greater effect on the junction resistance than the change in diameter of the microwire.

3.4.3.3 – Thiophene termination

Addition of the thiophene group to the surface of p – type Si microwires show that p-Si/PEDOT:PSS contacts remain ohmic in character, which is expected for a PEDOT:PSS contact to p-type Si. The junction resistance for this contact increases four fold in comparison to previous studies investigating methyl terminated p-type Si wires in contact with PEDOT:PSS/Nafion blends.⁴¹ Junction resistances in previous work were reported at $\sim 200\text{ k}\Omega$ of resistance for the p – type junction and this system has a junction resistance of $\sim 800\text{ k}\Omega$. Under light limited current, the methyl p – Si would contribute 5 mV of drop compared to the 25 mV of drop observed with the thiophene terminated p – Si microwires. The junction for methyl p –type Si/PEDOT:PSS was calculated over the entire -1 to 1 V range instead of the low bias, -100 to 100 mV, range. This may underestimate the junction resistance over the operation range.

Functionalization of the n-Si microwires with thiophene shows an unexpected response. The n – Si/PEDOT:PSS contact is expected to be rectifying because of the difference in the workfunctions of n – Si and PEDOT:PSS; however, the observed response resembles a leaky diode before surface saturation and an ohmic response once the surface has been completely terminated. Junction resistances of 20 $\text{M}\Omega$ or greater are observed for methylated n – Si/PEDOT:PSS whereas junction resistances decrease to $< 1\text{ M}\Omega$ for thiophene terminated n –

Si/PEDOT:PSS junctions. This decrease is very significant and is especially apparent when the iR response under light limited currents is compared. Methyl terminated n – Si/PEDOT:PSS contacts are observed to have > 300 mV of iR loss while the saturated thiophene surface has only 30 mV of iR loss. Table 3.3 summarizes the junction resistances and iR losses under light limited current for n – Si and p – Si with different terminating groups.

The junction with thiophene terminated n - Si represents a 95% improvement of the resistance in comparison to the methyl terminated junction. In addition, the observed iR drop for the thiophene junction represents only 4% of the V_{oc} for both the n – Si and p – Si junction resistance in a standard solar cell. This is a significant improvement from the 40% iR contribution to the V_{oc} for the methylated n – Si/PEDOT:PSS contact.

Table 3.3: Summary of Si/PEDOT:PSS junctions with different groups attached to the surface

	Dopant Concentration (cm^{-3})	Junction Resistance ($\text{M}\Omega$)	iR drop observed (mV)
n – Si methyl	$\sim 10^{17}$	21 ± 3	290 ± 50
p – Si methyl ^a	$\sim 10^{17}$	0.2	4
n – Si thiophene	$\sim 10^{17}$	1 ± 0.03	30 ± 10
p – Si thiophene	$\sim 10^{17}$	0.8 ± 0.06	25 ± 6

a. Values from reference 26 for comparison. Error is 1% of values reported

Decreasing the junction resistance to these values is a significant step forward toward integrated photoelectrochemical splitting of water. Interfacial modification of the silicon microwires with a methyl group shows an increase in V_{oc} which has been attributed in the literature to a dipole effect on the charge transfer out of the semiconductor.^{16, 39, 66-68} The presence of the interfacial dipole oriented perpendicular to the surface also contributes to the high junction resistance observed for the n – Si/PEDOT:PSS contact. Computational studies on

silicon surface functionalization with thiophene moieties have proposed enhancement of this effect, with a larger dipole at the interface of the silicon.^{67, 69, 70} Although these studies predict a larger dipole effect, the results in this study do not suggest an increase of a dipole at the surface of the wires.

Orientation of the dipole may have the largest impact on the junction. Methyl groups are oriented perpendicular to the surface and its dipole would be oriented in the same direction. Thiophene, on the other hand, would not have the dipole oriented perpendicular to the surface but would instead be at a fixed angle away from the surface. In Figure 3.12, the orientation of the dipole moments of each attached group is shown with respect to the surface.

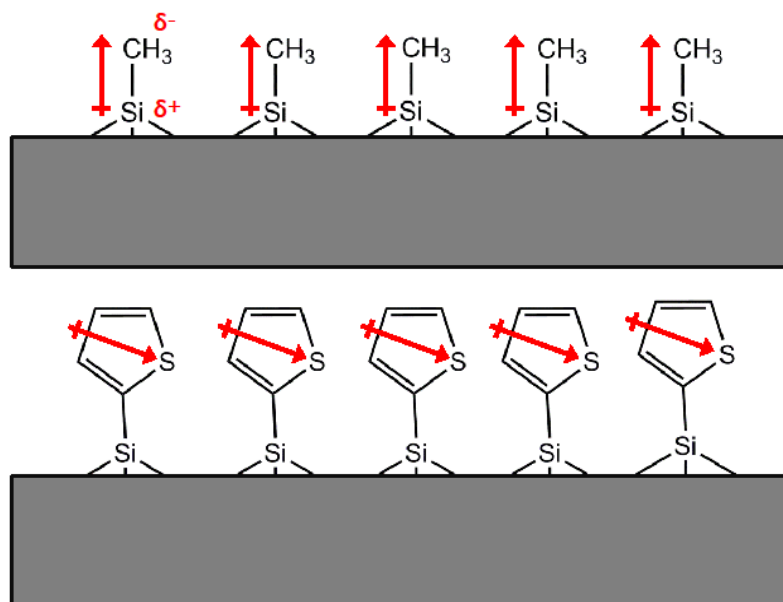


Figure 3.12: Dipole orientations of terminating groups to silicon surfaces

Attachment of thiophene to the surface of silicon is through the α -C on the ring based on the lithiated species. The dipole moment of thiophene is 1.07D whereas the dipole moment of the Si – C bond is 0.67D.⁶⁷ A dipole associated with the Si – C bond at the surface would not be observable because of the thiophene dipole moment. In addition, the orientation of the thiophene,

as shown in Figure 3.12, is not perpendicular to the surface and would have a fraction of the dipole affecting charge transfer and junction potential of the n – Si/PEDOT:PSS contact in comparison to the entire dipole moment affecting charge transfer when methyl is used.

Non – rectifying behaviour suggests that there may be a different mechanism of charge transfer altogether when thiophene is covalently bound. In addition, dipole effects would also manifest themselves when other rectifying contacts are utilized with n – Si. Mercury is often used to evaluate junction characteristics because of its metallic character and excellent diode contacts.⁷¹ Preliminary investigations using mercury drop contacts have not yielded results observed in this study with PEDOT:PSS. Further investigation is currently being conducted to gain insight into the mechanism of charge transfer between thiophene functionalized n – Si and a metallic contact. Capacitance measurements are being used to investigate the energy band configuration of the junction. Shifts in the flat band potential, correlated with surface coverage and dipole strength, would make a strong argument for a dipole effect at the interface. Junction measurements while controlling the temperature of the system will determine whether the mechanism is related to tunnelling or thermionic emission. An absence of temperature dependence would indicate a tunnelling mechanism of charge transfer across the interface whereas temperature dependence would indicate a different mechanism.

Interfacial alignment between the PEDOT:PSS and n – Si has also changed with the addition of the thiophene group to the surface. There has been a lot of contention in the literature describing the absolute energy levels of the HOMO/LUMO in thiophene, however, the most consistent values for these levels are 0.408 eV (LUMO) and 6.486 eV (HOMO)⁷² and are shown in Figure 3.13.

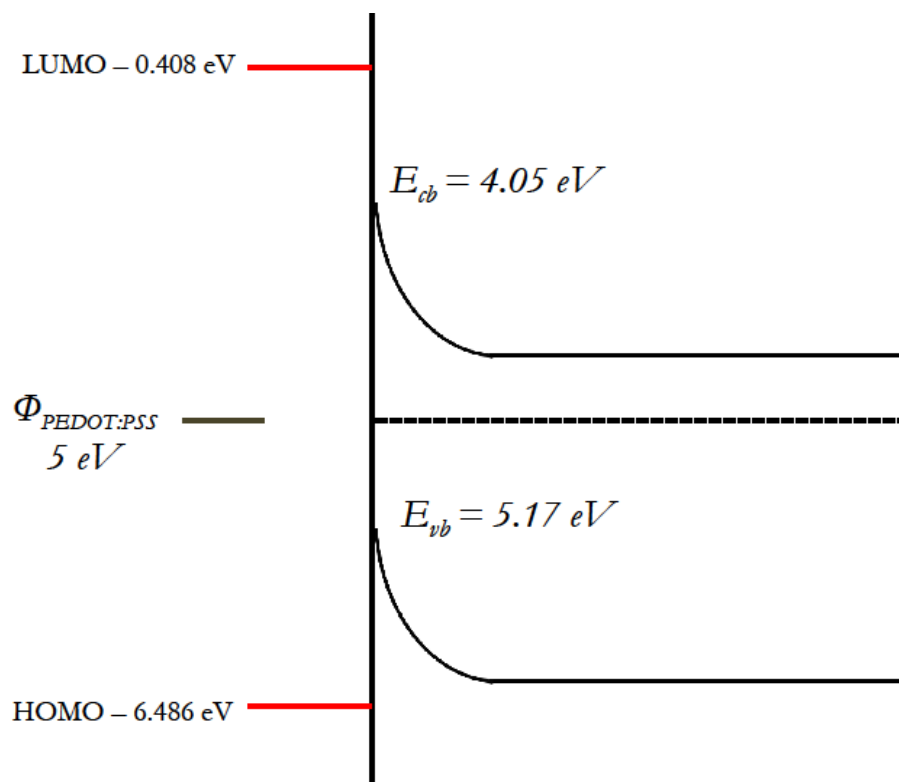


Figure 3.13: Interfacial energy diagram of n – Si in contact with PEDOT:PSS. The red lines indicate the HOMO/LUMO of the thiophene molecule. PEDOT:PSS workfunction is 5 eV.

The wide gap observed in the HOMO-LUMO diagram indicates the mechanism for charge transfer should be similar to a silicon oxide type contact. Silicon oxide has an energy gap of 9 eV and yields a very resistive junction to silicon.¹⁵ However, the conjugated pi – system of the thiophene ring would be much less resistive to electron transfer than a silicon oxide and is a possibility for the decrease in junction resistance.

Figure 3.13 shows the n – Si band diagram when equilibrated with the PEDOT:PSS. Electron transfer out of the silicon would be very energy intensive if the transfer happens through the LUMO of the thiophene. Hole conduction will also come at an energy penalty if the hole is transferred through the HOMO of the thiophene to the PEDOT:PSS. Another possibility for the lower junction resistance is the reduction of band bending in the silicon. The energy

penalty for charge transfer from the silicon to the PEDOT:PSS is large when thiophene is on the surface. Instead, thiophene would give up some of its electrons and, therefore, less would be drawn from the silicon when the contact is formed. If this were so, less charge would be gathered from the n – Si and the degree of band bending would be diminished. The reduction of the electric field in the n – Si would allow charge transfer to occur without surmounting an electric barrier, only passing through the thiophene ring. In addition, the absence of electron density in the HOMO of thiophene would facilitate favorable charge transfer across the interface and could be the basis for a lower junction resistance. Experimental and theoretical investigation of the fundamental basis of this effect may be explained using ultraviolet photoelectron spectroscopy (UPS) in conjunction with XPS in order to probe the valence structure of the interface. Much of the effects observed in this study have greater consequences in the bonding orbitals or valence band between thiophene and n – Si than the conduction band where XPS analysis usually characterizes the material and a thorough investigation of the interface between PEDOT:PSS/n – Si will aid in understanding the effects observed. Electrical techniques traditionally used to characterize diode behaviour, such as capacitance measurements, would not be sufficient because the diode character no longer dominates the behaviour and is replaced by an ohmic response of the junction.

3.4.4 Impact of Losses in Model Artificial Photosynthetic Device

Characterization of the electrical properties in a model artificial photosynthetic device has identified and addressed possible losses that may be detrimental to performance. The key metrics for evaluation of the losses are: the amount of current generated by the photoabsorbers (J_{sc}), the driving force of the junction for charge separation (V_{oc}) and the amount of acceptable loss for the system. In the initial work for evaluation of the junction, acceptable loss throughout the system

was 10 mV under light limited currents.^{17, 27, 39-41} Other sources have proposed losses of 800 mV for a single semiconductor device, including catalyst overpotentials.^{10, 12, 73} Evaluation of the losses in the system, based on the photovoltaic parameters, would give a more complete picture of the efficiency of the model artificial photosynthetic device.

Assuming light limited current is generated at both photocathode and photoanode and that a maximum V_{oc} is approximately 700 mV for a silicon system,⁵⁵ any loss contributions for an integrated system will be based on ion conduction through the membrane, electrical losses and catalyst overpotentials. Catalyst overpotentials for HER have currently been reported near 100 mV for earth abundant nanoparticle catalysts⁷⁴⁻⁷⁷ and OER overpotentials are often greater than 400 mV under ideal operating conditions.⁷⁸⁻⁸⁰ Ion conduction through the membrane structure is often negligible if materials such as Nafion are the benchmark or if a bipolar type configuration is used.^{17, 27, 28}

At dopant densities near $1 \times 10^{17} \text{ cm}^{-3}$ the microwires would contribute 20 k Ω of resistance; which at a light limited current of 20 nA per microwire, yields a voltage contribution of < 1 mV and would be considered negligible.⁴⁰ This is also true for the membrane contribution, where a 12 wt% PEDOT:PSS/Nafion composite yields a resistance of 2 k Ω or < 1 mV and can be neglected.

Voltage loss at the microwire/PEDOT:PSS junctions contributed significantly to the total electrical loss of the model system. Using highly doped base junctions, the voltage loss for the n – Si/PEDOT:PSS junction was 130 mV and the thiophene terminated n – Si was 30 mV. Methyl terminated p –type junctions were already significantly low, only contributing 5 mV to the

overall iR loss however addition of the thiophene group increased the junction resistance and iR contribution to 25 mV.

Table 3.4: Summary of voltage losses in a model integrated artificial photosynthetic device operating under AM1.5 conditions

	Thiophene Terminated Si	Methyl Terminated Si	Highly Doped Base Si
HER Overpotential (mV)	100	100	100
OER Overpotential (mV)	400	400	400
n – Si/PEDOT:PSS Junction Potential (mV)	30	300	130
p – Si/PEDOT:PSS Junction Potential (mV)	25	5	5
Total (mV)	555	805	635

The junction resistance using only methyl terminated silicon microwires constituted 40% of the total overall loss. The addition of the highly doped base and thiophene functionalized wires decreased the electrical contribution to 21% and 9% of the loss respectively. If we factor in the 1.23 V required for thermodynamic water splitting, the total potential required for the methyl terminated configuration will be 2V, the highly doped base configuration will be 1.9 V and the thiophene functionalized configuration only requires 1.8 V. Operation of the integrated solar fuels device under AM 1.5 light limited current and only 800 mV of loss, would not be possible if the methyl terminated microwire configuration was used. Thiophene terminated and highly doped base configuration would yield a workable device, assuming these materials and conditions are used.

3.4 - Conclusion and Future Work

To address the high junction resistance between methyl-terminated n-type Si microwires and PEDOT:PSS, a highly doped ($\sim 4.5 \times 10^{18} \text{ cm}^{-3}$) region was grown at the base of the Si microwires. This contact to PEDOT:PSS decreased the junction resistance from 21 M Ω to 5 M Ω and reduced the associated system-based iR loss from 290 mV to 130 mV. These values amount to a voltage drop of 41% and 12%, respectively of the V_{oc} reported for Si-based photovoltaics under AM 1.5 G illumination. Characterization of the transition between the n^+ and n region of the Si microwire provided insight into the alignment of the interface between the two dopant regions and provided a better understanding of the dynamics of charge transfer in Si microwires doped in this fashion. Techniques for increasing the efficiency, such as the use of a buried junction that use a high-doped/low-doped contact, would benefit from this type of characterization.

Once the dopant concentrations in Si have reached a saturated value, the addition of more dopants will not decrease the resistivity of the material.⁵⁹ To circumvent this concern, the surfaces of n – Si and p – Si microwires were functionalized with a thiophene moiety until the surface was saturated. The contact resistance to PEDOT:PSS dropped to 1 M Ω under operating voltages for both contacts and system – based iR contributions decreased to 30 mV for n – Si but increased to 25 mV for p – Si junctions. In addition, non – rectifying contact was observed for n – Si/PEDOT:PSS junctions. Such favorable decreases in junction resistances constitute major steps forward for use of silicon – based photovoltaics in integrated photoelectrochemical splitting of water.

Future work will focus on systematic studies of planar silicon with UPS and XPS, in addition to electrical measurements, to understand the charge transfer at the interface between n

– Si and PEDOT:PSS functionalized with different groups. Building on interfacial data of single moieties, additional groups can also be added to the surface to create a conjugated system, covalently bound to the surface. Focusing on conjugated systems may lead to evidence for HOMO/LUMO effects on charge transfer out of the semiconductor. Another possible avenue to unravel charge transfer across the interface with thiophene attached to the surface is to repeat the same experiments with different polymer materials. Different polymers have different workfunctions and band alignments and may show that this effect is specific to PEDOT or whether it is a broader effect related to polymer interaction with the surface.

Finally, modification of n – Si with the monomer unit, 3,4 – ethylenedioxythiophene (EDOT), is currently being investigated to reduce the junction potential even further. Covalent binding of the monomer to the surface of silicon and subsequent polymerization from of the monomer would be considered to be the lowest possible junction resistance because the polymer is covalently bound to the surface. All previous studies are through non – covalent interactions between the polymer and PEDOT:PSS. A comparative study of the covalently bound EDOT and the polymerized PEDOT from the monolayer would examine whether covalent binding to the surface has any effect on the junction resistance to the polymer material.

Chapter 4: Functionalization of Representative Silicon Microwire Surfaces

4.1 – Introduction

In the previous chapter, novel approaches improving the junction characteristics of silicon microwire/conducting polymer contacts were investigated. Modification of the junction has allowed for more efficient charge transfer across the interface, lowering the junction resistance between them.⁴³ Despite the successful drop in junction resistance, the formation of an insulating silicon oxide layer still occurs and its impact remains unclear over long term exposures to aqueous and ambient conditions. Another observation is a large oxide peak, which does not appear with planar silicon under the same conditions, in the silicon microwire X-ray photoelectron spectra.

X – ray photoelectron spectroscopy is utilized extensively for the characterization of planar silicon surfaces and the effectiveness of functionalization on these surfaces. The formation of oxide, passivation of the surface with an organic group and stability of any terminated surface can be investigated using this technique. Literature on functionalization of planar silicon surfaces has focused on two crystal faces, Si (111) and Si (100).^{30, 35, 68, 81, 82} The unreconstructed Si (111) phase has a single perpendicular, surface bond and Si (100) has two bonds located on the surface.^{30, 49} These two faces, however, are not the largest contributors to the surface area of the exposed silicon microwire surface. Two crystal faces oriented 90° to the Si (111) direction make up the sides of the microwire surfaces. For a 12 – sided microwire, the Si (211) and (110) crystal faces alternate around the circumference of the wire while a 6 – sided microwire only has the Si (110) crystal phase exposed around the wire.^{24, 83, 84} In Figure 4.1, the model of the silicon microwire shows the dominance of these higher order crystal faces on the surface of the silicon microwires.

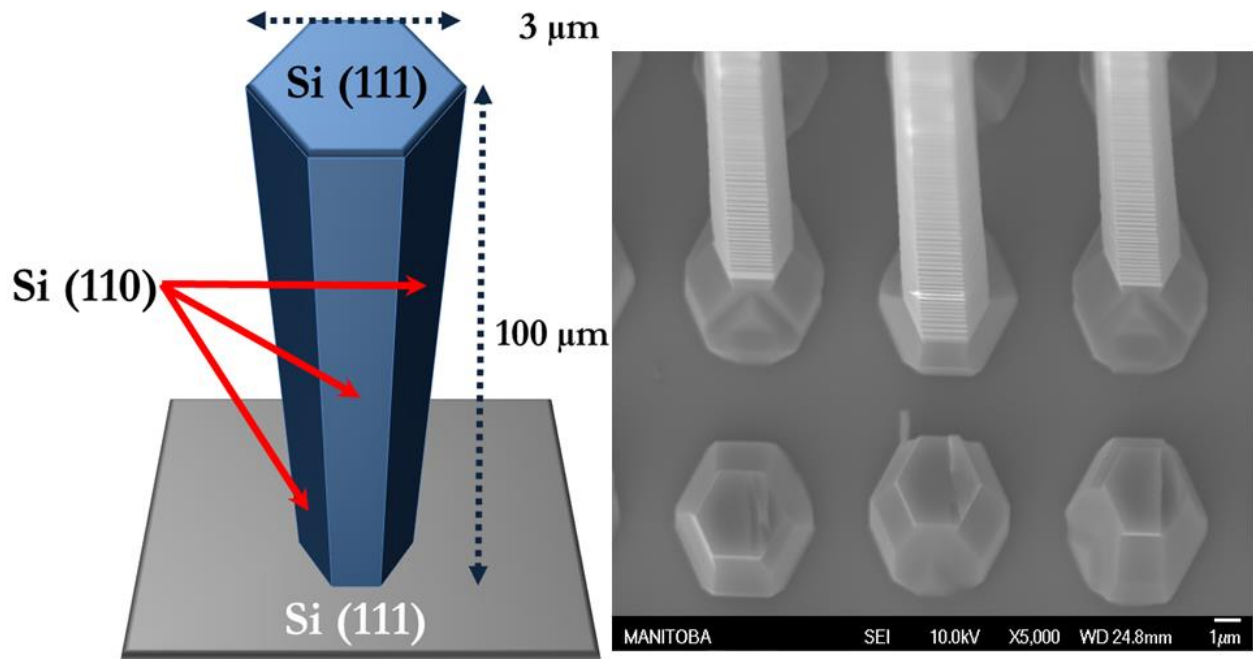


Figure 4.1 Model of silicon microwire with dominant crystal faces highlighted for a 6 – sided wire. The right scanning electron image an array of microwires that have 6 – sided facets down the length of the wire.

These phases have a fundamentally different surface bonding structure to Si (111) and would therefore change the possibility of completely saturating every surface site with a Si – C bond to prevent the formation of silicon oxide at the surface. Figure 4.2 shows the unreconstructed Si (211) and (110) surfaces.

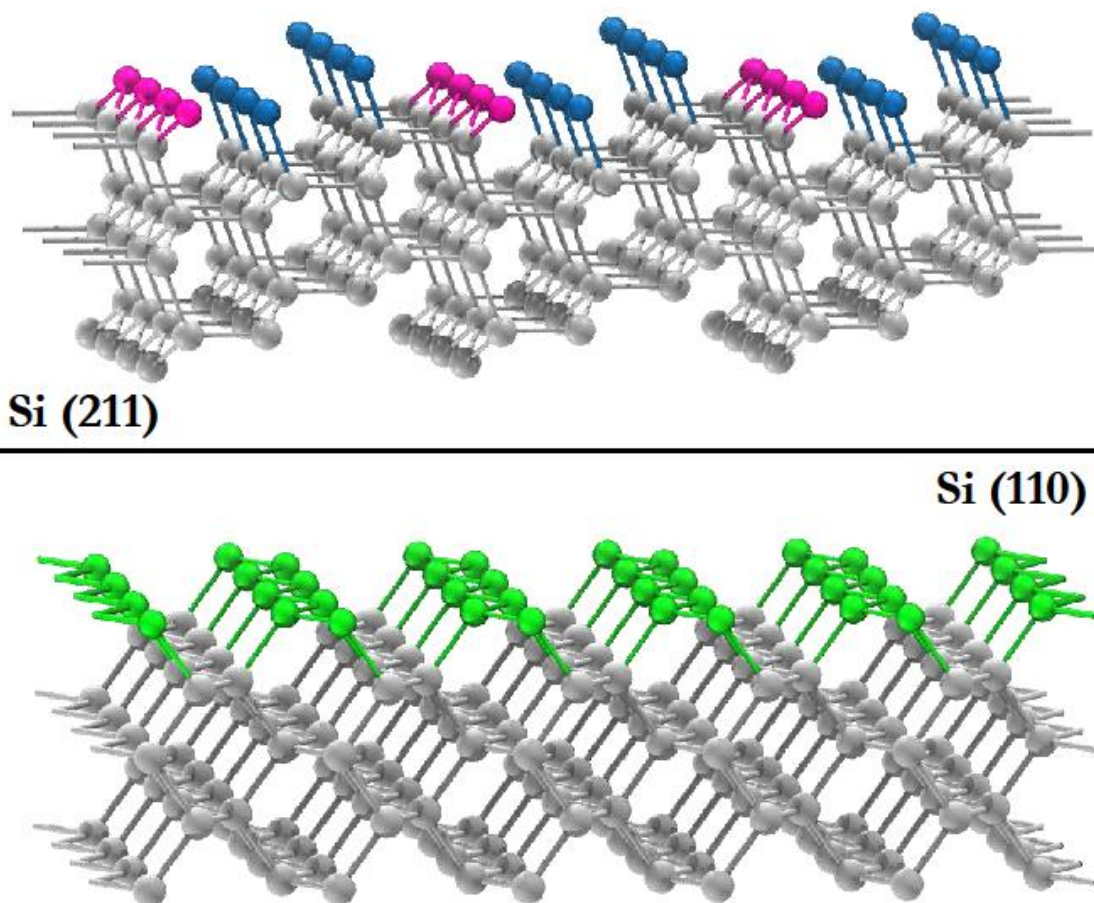


Figure 4.2 Unreconstructed Si (211) and (110) surfaces. The different colours represent possible surface bonding sites. In Si (211), the two colours represent distinct bonding sites. The blue represents one possible bonding site, similar to Si (111), while the pink represents two bonding sites, similar to Si (100). Si (110) has one possible bonding site that is similar across the whole surface.

Possible differences in the functionalization of silicon microwire surfaces and those investigated in literature present a challenge when interpreting the quality of passivation of a silicon microwire array. In this work, Si (211), Si (110) and Si (111) will be functionalized using a methyl group. Passivating the Si (111) surface with a methyl group has shown complete termination of all silicon atop sites^{52, 85} and is used as the standard when comparing the other planar, representative silicon surfaces. The rate and amount of oxidation between each surface will also be compared to investigate the effect of passivation on each crystal surface.

4.2 - Experimental

4.2.1 - Surface Chemistry

Planar Si surfaces were dipped in a 10 vol% HF solution before being transferred to a RCA 1 (NH₄OH (30 vol%): H₂O₂ (30 vol%): H₂O (18 MΩ); 1:1:5 v/v/v) clean for 15 minutes at 70 °C. The samples were then removed from the RCA 1, HF dipped and transferred to an RCA 2 (HCl (27 vol%): H₂O₂ (30 vol%): H₂O (18 MΩ); 1:1:6 v/v/v) clean for 15 minutes at 70 °C. After cleaning, samples were HF dipped, transferred to a 30 wt% KOH solution for 1 minute and RCA 2 cleaned again to remove any growth catalyst that may be present at the surface of the rods. These samples were then given a final HF dip to create an H-terminated surface before transferring them to a N₂ filled glovebox. Si (111) samples would also be placed in a N₂ purged NH₄F solution for 10 minutes before rinsing and transferring them to the glovebox. NH₄F solutions were purged for a minimum of 30 minutes with PP grade N₂. The glovebox O₂ content never exceeded 10 ppm at any time during the reactions. H-terminated samples were placed in a saturated solution of PCl₅ (99.999 %, Alpha-Aesar) in chlorobenzene (99.8% anhydrous, Sigma – Aldrich) and was heated at 90 °C for 45 minutes to give a Cl – terminated surface. After the reaction, the arrays were rinsed with chlorobenzene and THF (>99.9% anhydrous inhibitor free, Sigma - Aldrich) before being transferred to a solution of methyl lithium (1.6 M in diethyl ether, Sigma – Aldrich) that was allowed to react for a minimum of 3 hours at 30 °C. Diethyl ether (99.8% anhydrous, Sigma Aldrich) was added to the solution in equal parts to prevent solvent loss during the reaction and the reaction tubes were enclosed in a polyethylene container vented out of the box. The solution was then allowed to cool; samples were rinsed with THF and methanol (99.8% anhydrous, Sigma-Aldrich) and were finally removed from the glovebox in methanol. Following removal from the glovebox samples were rinsed with acetonitrile,

methanol, isopropanol and water and were stored under nitrogen for further use and characterization.³⁰

4.2.3 - X-ray Photoelectron Spectroscopy

X-ray photoelectron spectroscopy (XPS) was performed on a Kratos Axis Ultra DLD spectrometer (Kratos Analytical Ltd.) with monochromated Al K α radiation (1486.6 eV) at 10 mA emission current and 15 kV anode voltage with a base pressure of 1×10^{-9} torr without the use of charge neutralization. Spectra were collected with a fixed analyzer transmission mode perpendicular to the surface; survey scans were collected with a pass energy of 160 eV while high resolution scans of individual elements were collected with a pass energy of 20 eV. Peak fitting was carried out on the high resolution spectra using CasaXPS fitting software. Background subtraction was completed using the Shirley algorithm and all peaks were fit using mixed Gaussian - Lorentzian functions with 70% Gaussian and 30% Lorentzian contribution. All results are calculated by taking the average of three spots on three separate samples of a single crystal phase.

4.2 Results

4.2.1 Ideal Coverage of Si (110) and Si (211) Surfaces

In order to investigate the surface coverage and degree of oxidation of any planar silicon surface in this study, an expected ratio of surface to bulk species is calculated and compared to experimental ratios of characteristic photoelectron peaks associated with a surface group and the bulk silicon peak. Passivation of the Si (111) surface using a methyl moiety forms a single monolayer, terminating every atop site on the surface. The size of the methyl group (Van der

Waals radius = 2.3 Å) and the internuclear spacing between atop sites on Si (111) (3.8 Å) enable full coverage of the surface.^{29, 50-52, 86, 87} Computationally expected ratios of surface sites to bulk species will be compared to peaks fit in the high resolution XPS data. Silicon oxide (~103 eV) in the Si 2p region and Si – C (~283.8 eV) in the C 1s region are normalized to the bulk silicon (~100 eV) to generate the experimental ratio. Bulk silicon species are only examined over a finite depth based on the escape depth of a Si 2p electron. The effective escape depth of a Si 2p electron is based on an empirical formulation given in Equation 4.1.⁸⁸

$$\lambda_{Si} = \left(0.41 \text{ nm}^{-\frac{1}{2}} \text{ eV}^{-\frac{1}{2}}\right) a^{1.5} E_{Si}^{0.5} \quad (4.1)$$

Where a_{Si} is the radius of the silicon atom (0.272 nm)^{50, 51, 86, 89} and E_{Si} is the kinetic energy of the Si 2p electron. In this study, Al K α (1486.6 eV) radiation is used and E_{Si} is 1387 eV making the value for $\lambda_{Si} = 2.17$ nm. Calculated ratios of surface to bulk species are given in Equation 4.2.^{50, 51, 86, 89}

$$\frac{I_{Si,surf}}{I_{Si,bulk}} = \frac{n_{Si,surf}}{n_{Si,bulk} l_{Si} - n_{Si,surf}} \quad (4.2)$$

Where l_{Si} is the escape depth given by $l_{Si} = \lambda_{Si} \cos\theta$ with respect to surface normal. At 90°, where the majority of the analysis is undertaken, the value of l_{Si} is 2.17 nm. The bulk density of Si is given as $4.995 \times 10^{22} \text{ cm}^{-3}$. In Table 4.1, each representative silicon surface is summarized with the expected ratios for $\frac{I_{Si,surf}}{I_{Si,bulk}}$.

Table 4.1 Summary of surface density and calculated surface to bulk ratios.

Crystal Phase	Surface Density (atoms/cm ²)	$\frac{I_{Si,surf}}{I_{Si,bulk}}$
Si (111)	7.83 x 10 ¹⁴	0.078
Si (110)	9.59 x 10 ¹⁴	0.098
Si (211)	5.54 x 10 ¹⁴	0.054

*Bulk silicon density is 4.998 x 10²² cm⁻³

From Table 1 the Si (110) shows the highest ratio between the three different phases while Si (211) is the lowest. The surface density of Si (211) is currently still under contention in the literature.⁹⁰⁻⁹² Unreconstructed Si (211) surface density is calculated from the surface density of Si (111).⁹²

Experimental ratios are determined by normalizing characteristic peaks of surface bonded species to the bulk. Ratios of the silicon oxide peak and the methyl carbon peak to the bulk Si 2p envelope will determine the extent of oxidation or coverage of any functionalized group. Freshly etched samples do not show a silicon oxide peak above the limit of detection but exposed to ambient conditions over time, the oxide peak at ~ 103 eV eventually begins to appear above the background and can be quantified. The experimental ratio is then normalized to the calculated ratio to determine surface coverage of an unreconstructed sample.

In Figure 4.3, survey and high resolution spectra of planar silicon surfaces are illustrated. The survey spectra are often utilized to ensure the surface is free of contaminants from the surface chemistry procedure. Magnesium, manganese, fluorine and iron are all contaminants that have been observed in previous sample preparations. Grignard reagents are often the source of metal contamination while fluorine results from hydrofluoric acid or ammonium fluoride etch

solutions. If any contaminants are present on the surface, lower surface coverages have been observed and these samples are not used in further surface functionalization.

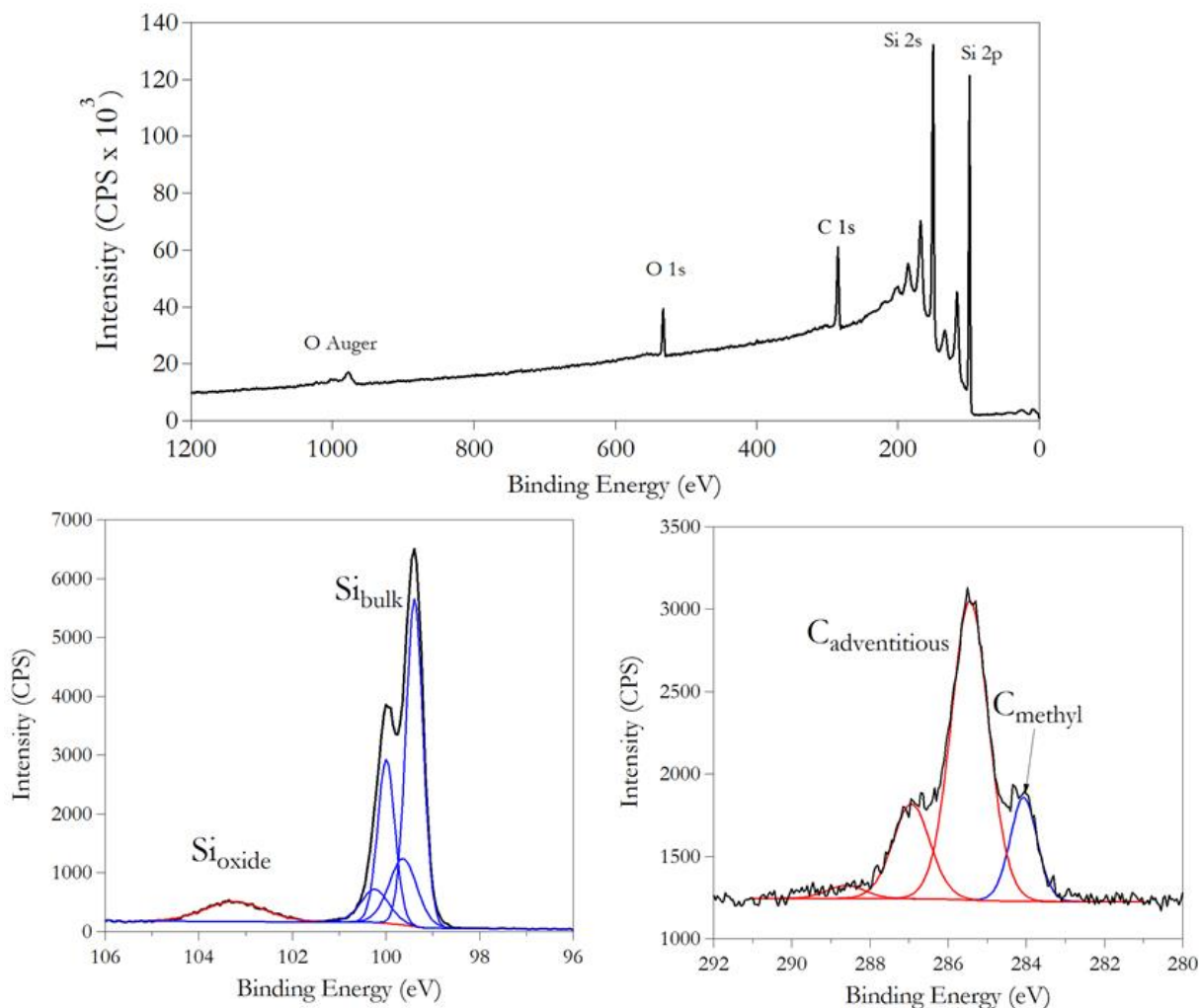


Figure 4.3 X-ray photoelectron spectra of planar silicon sample. Top shows survey spectra, bottom left is the Si 2p high resolution spectrum and the bottom right is the C 1s high resolution spectrum.

Peak fitting of the high resolution Si 2p and C 1s spectra is carried out using CasaXPS fitting software. In the Si 2p envelope, the spin – coupled 2p orbital creates two peaks separated by 0.6 eV and two individual contributions are required to model the Si_{bulk} region of the spectrum. The second set of peaks in the Si_{bulk} region, located 0.3 eV higher in binding energy

than the large peaks, are often considered peaks originating from silicon atoms at the surface.^{29, 85, 93} Normalizing the high binding energy contribution to the low binding energy contribution is not used to find experimental ratios because high error is observed when fitting these peaks using the Kratos instrument. A synchrotron source with variable excitation energy was utilized in studies that quantified surface coverage using the peaks under the Si_{bulk} region of the spectrum. The spin – split pairs of Si^{3/2} and Si^{1/2} were constrained to the same full width half max (FWHM) values. The Si_{Oxide} region of the Si 2p high resolution spectrum is fit with one peak because the number of chemically distinct oxides is close enough in energy that they cannot be distinguished with the resolution of our instrumentation. In addition, the total oxide contribution at the surface is used to quantify extent and amount of oxidation, therefore, the entire Si_{oxide} region is fit with one peak.

Fitting the C 1s region requires multiple peaks to accurately describe the C_{adventitious} region and one peak is used to describe the C_{methyl} region. Adventitious carbon consists of adsorbed hydrocarbons present in the atmosphere and within the instrument under ultra – high vacuum conditions. These hydrocarbons are often removed using thermal desorption however this was not utilized in these experiments. Aliphatic and aromatic species are described under the peak at 285 eV, alcohols/ethers are at 287 eV and carboxylic acids are described by the 289 eV binding energy. All of these peaks have the same FWHM and are constrained to FWHM < 1.2 eV. The C_{methyl} species is described by the peak at 283.8 eV and its FWHM < 1.0 eV. Peak models are created once for every crystal face and are propagated to ensure the same model is used to describe the same sample. The average of three samples for each crystal face is used to describe the surface coverage and extent of oxidation.

4.2.2 H-terminated Planar Silicon Surfaces

To understand the manner with which the representative silicon microwire surfaces will behave in ambient conditions, oxidation of H-terminated surfaces are monitored by XPS. In Figure 4.4, the oxidation of these surfaces is followed over the course of a month.

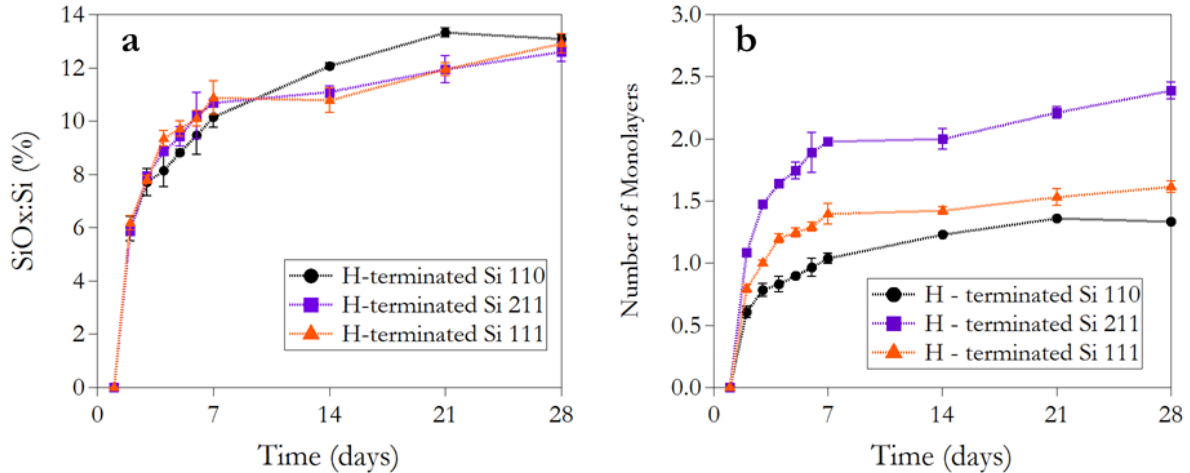


Figure 4.4 Oxidation of H-terminated silicon surfaces over the course of 1 month. a) Ratio of Si_{oxide} to Si_{bulk} time dependence represented as a percentage for clarity b) Equivalent monolayers formed on each silicon surface.

Each surface reaches a saturation value after a week of ambient exposure. The left figure shows the ratio between the silicon oxide and the silicon bulk peaks in the high resolution spectrum, while the figure on the right shows the normalized ratio based on the calculated values for monolayer coverage in Table 4.1. Monolayer coverage assumes that for each atom at the surface, there exists one possible bonding site and reconstruction of the surface is negligible. The Si (111) and (110) surfaces saturate at approximately 1 monolayer, however the Si (211) surface requires 2 equivalent monolayers to saturate. The thickness of native oxide layer on silicon is expected to be ~10 Å while a silicon oxide monolayer is expected to be 3.5 Å thick.⁹⁴⁻⁹⁶ Based

on Figure 4.4 above, the Si (211) surface is the only surface that reaches a full native oxide while the Si (110) and Si (111) surfaces only grow a monolayer of oxide on the surface.

4.2.3 Methyl Terminated Silicon Surfaces

Methylation of the silicon surface provides kinetic protection to the formation of a thermodynamically favorable silicon oxide layer by passivating reactive surface sites with a Si – C bond.^{30, 50, 51, 86, 89, 97} Accurate characterization of surface coverage on silicon microwires is difficult because the majority of the exposed surface is not the same phase as those investigated in the literature. Accurate determination of surface coverage is essential to prevent oxidation and can be achieved by characterizing planar silicon with crystal faces that represent the exposed microwire surfaces.

Stability of the monolayer over the course of a month is extremely important to ensure protection from oxidation. A characteristic shift is observed in the C 1s high resolution spectrum due to the presence of a Si – C bond at the surface and can be observed in Figure 4.3 Using the ratio of the C 1s methyl peak to the bulk silicon peak, a surface coverage can be calculated. Figure 4.5 illustrates the behaviour of surface coverage over the course of a month.

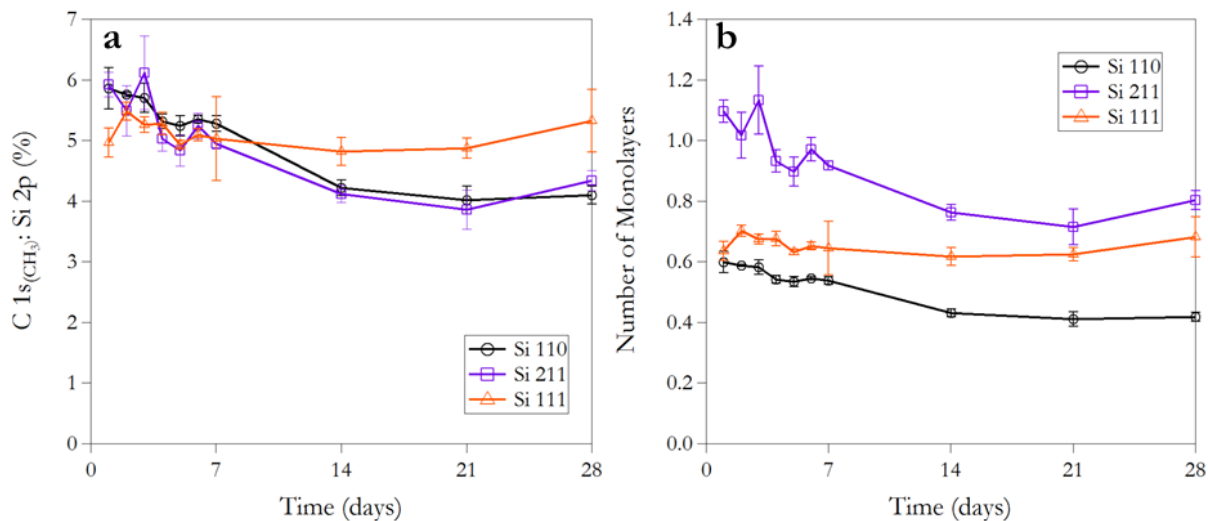


Figure 4.5: Behaviour of methyl monolayer over the course of 1 month exposed to ambient conditions. (a) Ratio of methyl peak in C 1s to Si_{bulk} represented as a percentage for clarity. (b) Surface coverage expressed in monolayers

Figure 4.5b shows the Si (211) surface has formed a full monolayer but Si (111) and (110) only form ~0.6 of a monolayer after the initial functionalization. Si (110) and Si (211) surface coverage drops below 0.5 and 0.8 of a monolayer respectively as the samples are exposed to the ambient conditions; however, Si (111) surface stays relatively stable over the period of a month.

Surfaces terminated with a methyl group are expected to exhibit lower rates of oxidation and incomplete monolayers of oxide when compared to H – terminated samples. In Figure 4.7, the oxidation of methylated Si (111), Si (110) and Si (211) over the course of 1 month is presented.

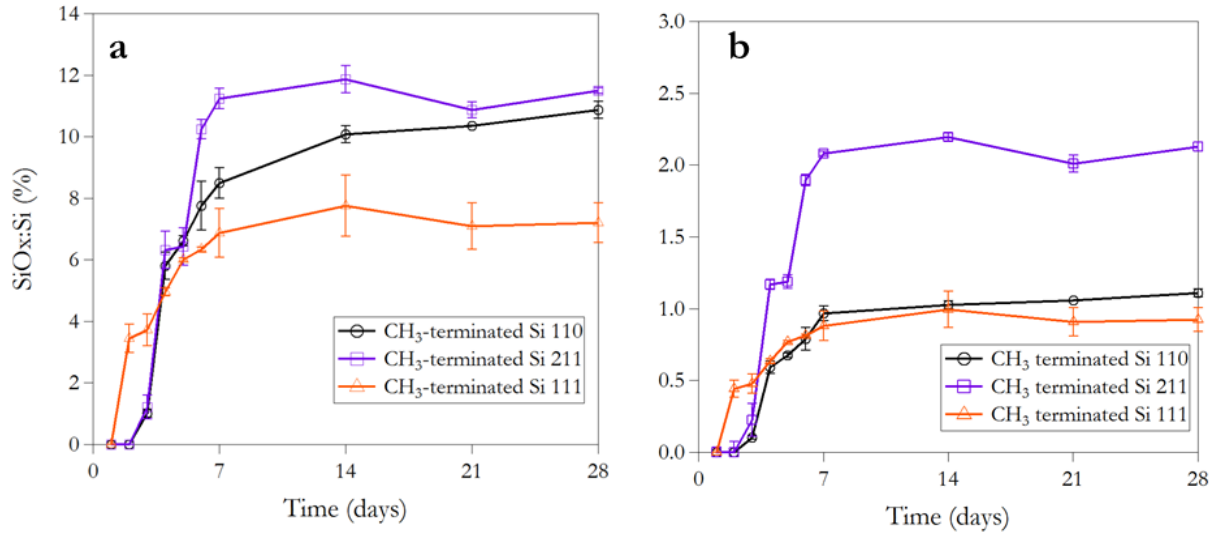


Figure 4.6: Oxidation behaviour of methylated silicon surfaces. (a) Ratio of oxide peak to Si_{bulk} as a percent for clarity. (b) Number of monolayers of oxide formed over the course of a month

All silicon samples reach a saturation value after a week in ambient conditions. Oxidation of the surface is delayed by at least 3 days and no silicon oxide peak observable above the baseline in comparison to H-terminated samples. Direct comparison between H-terminated with methyl terminated silicon microwire surfaces will give an indication to the level of oxide expected to grow in as the samples are exposed to ambient conditions. Figure 4.7 shows a comparison of the rates of oxidation on each crystal phase for H-terminated and methyl terminated samples.

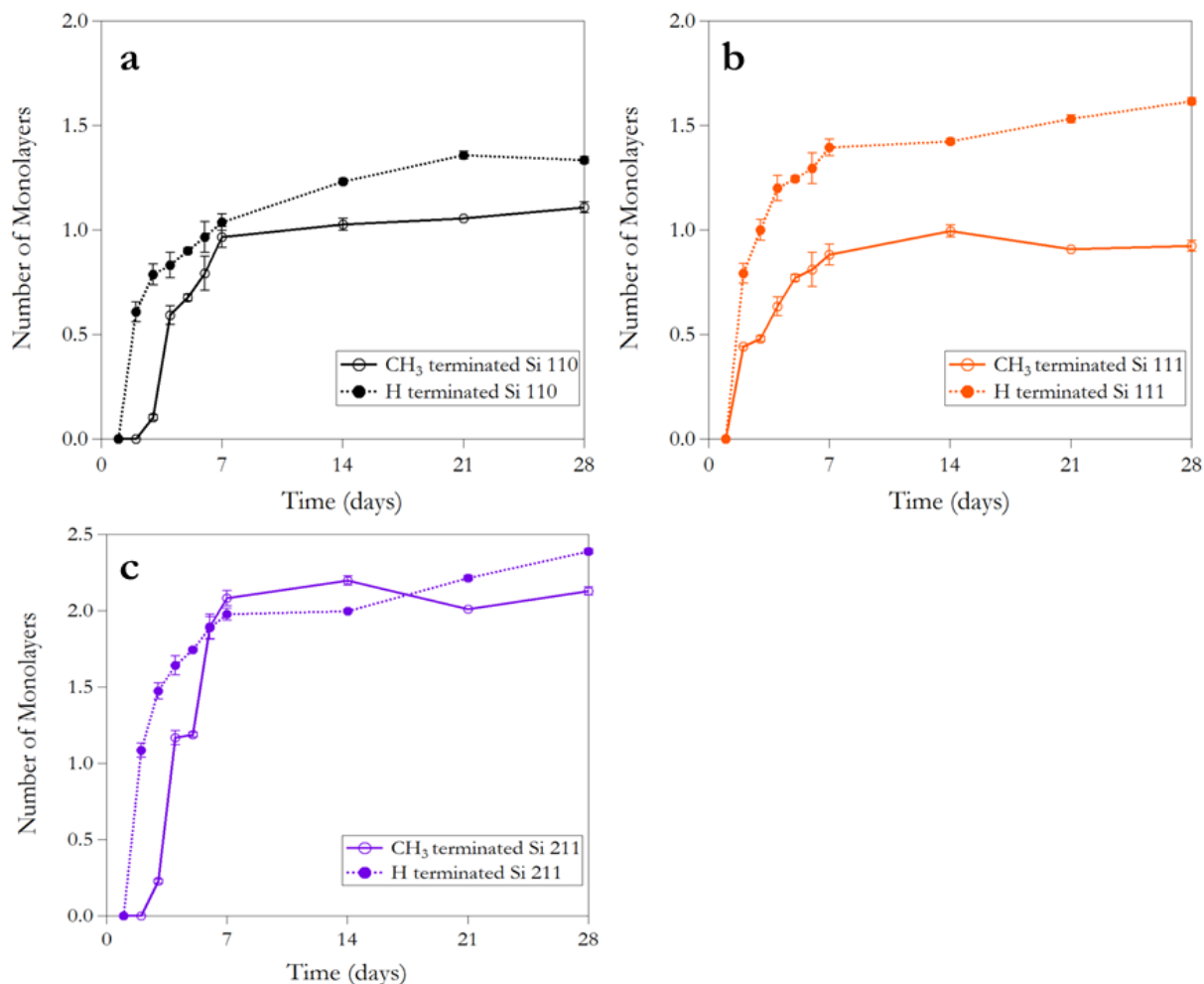


Figure 4.7: Rate of oxidation in number of equivalent oxide monolayers for each planar silicon phase (a) Si (110) (b) Si (111) (c) Si (211) The dashed lines represent the H – terminated surfaces while the solid lines represent the methyl terminated surfaces

Figure 4.7a,b indicate that the methyl termination blocks the formation of a complete silicon oxide layer on the surface of Si (111) and (110). The effect is more pronounced in Si (111), with less than a full monolayer being formed at any time. Methylation of the Si (211) surface does not appear to affect the overall amount of silicon oxide formed on the surface; however it does affect the rate of oxidation for the first week. The monolayer forms much faster without the methyl group protecting the surface.

4.3 Discussion

4.3.1 Oxidation of H-terminated Planar Silicon Surfaces

The rates of oxidation for each surface are similar for all faces as shown in Figure 4.4. The saturation value of the surface is different for all the phases and could be due to the manner in which the surface is oxidized. The openness of the Si (211) surface may allow for oxidation to occur below the plane of the surface. Figure 4.2 shows two individual areas where surface termination could occur. Surface sites represented by the pink spheres would be below the surface plane and are not considered bonding sites for the ideal calculation.⁹² However, they are still accessible to ambient oxygen molecules and, in addition to its high surface energy, the Si (211) surface would be more susceptible to oxidation in comparison to the other crystal faces.

Ratios higher than one monolayer are somewhat unexpected for Si (110) and Si (111). The number of surface sites and available dangling bonds for functionalization are well established in the literature, especially when compared to the Si (211) surface where there are still contentious issues on reconstruction and actual number of surface sites. High ratios could originate from lower oxidation states present at the surface in addition to fully oxidized SiO₂ species. These states appear at lower binding energies less than 103 eV and will expand the FWHM of the SiO_x peak when fitting that region. This would give an artificially high ratio between the SiO_x and Si_{bulk} region and consequently, a higher calculated surface coverage.

Another possibility for high oxidation coverage is the surface roughness. All calculations in this Chapter have been based on unreconstructed crystal faces of silicon but these surfaces may not occur at the surface in reality. Etching of these crystal phases to create long terraced,

atomically flat surfaces is not trivial and may also contribute of the high ratios if unreconstructed surfaces are not achieved through etching.

4.3.2 Methylation of the Silicon Surfaces

Si (111) spacing between bonding sites is 3.8 Å, which is much larger than the 2.3 Å Van der Waals radius of the terminating methyl group. Functionalization of the Si (111) surface in this study showed a surface coverage of 0.65 of a monolayer and leaves approximately 0.35 open to oxidation. The difference in monolayer coverages after 1 week of oxidation between methyl terminated and H –terminated Si (111) is 0.3 which could represents the open surface sites not passivated by the methyl groups. Oxidation levels may, however, be due to subsurface oxide formation or to the etching process highlighted in the previous section. Subsurface oxide formation would increase the silicon oxide to silicon bulk ratio, leading to higher monolayer coverages overall. In addition, the rate of oxidation over the first few days has a very similar character between H –terminated and methyl terminated Si (111) surfaces and may indicate the presence of highly reactive sites that were unable to be terminated by the methyl moiety. These sites could be terrace edges or defect points that are not taken into account when calculating the theoretical surface ratio.

Termination of the Si (110) surface is not as straightforward as the Si (111). The distance between the possible binding sites is 2.35 Å, which is very similar to the methyl Van der Waals radius. However, the Si – C bond length is 1.87 Å, and could allow enough space to functionalize all dangling bonds at the surface. Dangling bonds for functionalization would orient themselves ~ 50° to the surface instead of 90° with Si (111). The surface coverage of the Si (110) surface is observed to be 0.4 of a monolayer while the remainder of the surface remains

open to oxidation. Such a low surface coverage may be attributed to the orientation of the surface bonding environment. Steric interactions may prevent total passivation of the surface by the reacting methyl groups. The difference between the oxidation level methyl terminated and H – terminated Si (110) surface is only 0.2 after 1 week in ambient atmosphere. however the onset of oxidation does occur at a much later time than with the H –terminated Si (110) samples. Similar arguments can be made for the Si (110) surface as the Si (111) surface. Defect points, step edges and terraces may all be points where silicon oxide would easily form but would be difficult for methyl groups to attach. The Si (110) surface may be particularly susceptible to the defect points and step edges as the etching procedure used may not be ideal for this surface. The etch used is a general KOH etch but there may be a more suitable solution to create long terraced, atomically flat Si (110) surfaces on the microwires.

Methylation of Si (211) yields a surface coverage of 0.7 of a monolayer, which is the highest of any of the surfaces in this study. The available surface sites for functionalization are separated by 3.8 Å and are oriented 70° from the surface, making it very favorable to functionalize these surface sites. The methyl monolayer ratio does support this as the surface coverage is even higher than the Si (111) studied previously. Oxidation is also slowed initially but then reaches similar values as what is observed in the H –terminated samples after an extended period of time. This surface may suffer greatly from subsurface oxidation because of the open structure but it is encouraging to observe the high surface coverage sustained over the whole period of analysis and the shift in the rate of oxidation at the initial time periods. Microwires grown with 6 – sided facets would not be affected by this surface, however, 12 – sided silicon microwires would require careful evaluation of this surface.

4.3.3 Consequences of Methylation on Silicon Microwires

Functionalization of representative silicon microwire surfaces has been achieved at varying degrees of monolayer coverage. 6 – sided microwires have Si (110) surfaces around the circumference and 12 - sided microwires have alternating Si (211) and (110) surfaces.^{20, 24, 83, 84, 98} The tops of the wires are Si (111) and represent a small portion of the exposed microwire surface. 6 – sided microwires are predicted to be more resistant to oxidation because they do not have a Si (211) phase present on any exposed surface. Fabrication of silicon microwires with Si (111) phase along the circumference would be ideal to exhibit the maximum resistance to oxidation. Characterization of methyl terminated microwires will likely display methyl to bulk silicon ratios similar to Si (110) and Si (111) surfaces because of their individual contributions to the overall exposed area.

4.4 Conclusion and Future Work

Representative silicon microwire surfaces were functionalized using methyl groups to protect the surface against oxidation. The Si (111) surface was observed to have the greatest resistance to oxidation despite not having the highest surface coverage while the Si (211) surface proved to be the least resistant to oxidation despite having the highest overall surface coverage. Si (110) surfaces showed some resistance to oxidation, much greater than the Si (211) surface. A 6 – sided silicon microwire would be more resistant to oxidation than a 12 – sided microwire based on the makeup of the surfaces around the circumference. Angle dependence of the calculated surface coverages indicates that there will be an angular component to surface characterization of silicon microwires because of their multi – dimensional nature.

Future work would involve greater efforts to investigate the overall surface roughness of the surfaces. It is not clear from this work whether this will contribute to the observed ratios and needs to be investigated. Atomic force microscopy (AFM) or scanning tunnelling microscopy (STM) will aid in investigation of the surface roughness of the surfaces. The angle dependence of the calculated ratios also requires more investigation and scrutiny. Angle resolved XPS is a powerful tool that will unravel some of the unanswered questions for understanding monolayer coverage on the silicon microwires. Currently, investigation of the angle resolved spectra has allowed us to differentiate between the base of the intact array and the microwires themselves however quantification of the surface coverage still requires further investigation.

Chapter 5: Conclusions and Future Work

Throughout the works presented in this thesis, surface functionalization of silicon microwires has proved to be a significant component to addressing many aspects of integration for an artificial photosynthetic device. High junction potentials with methyl terminated silicon microwires constituted a large energy penalty in order to prevent oxidation of the silicon surface. Two techniques were presented; one involved the use of a highly doped base to change the charge transfer mechanism from thermionic to tunneling in order to lower the junction potential and the other involved changing the terminating group preventing oxidation from a methyl group to thiophene; a group that resembled PEDOT:PSS, the electrical conducting component of the membrane. The junction potential dropped from 300 mV to 100 mV when using the highly doped base to make the contact and dropped to 30 mV when using the thiophene group. These two techniques now constitute a major step forward for integrated artificial photosynthesis because of the minimal iR contribution to the acceptable losses in this system. This also opens the door for less efficient catalysts, with higher overpotentials to be used in prototype device structures to investigate how an integrated device will behave.

Characterization of silicon microwires is a crucial step along a fabrication process. Leaving the array intact, without removing the microwires from the substrate would simplify fabrication and reduce waste when the device reaches the fabrication stage. Protection of the silicon microwire surface from oxidation has been achieved on Si (111) and Si (100) surfaces. These surfaces, however, do not significantly contribute to the silicon microwire surface area. The major surface contributions are the phases Si (211) and (110) which have their own individual bonding environment and non-trivial surface structures. Investigation of these surfaces showed they are in fact distinct from the Si (111) surface in X-ray photoelectron spectroscopic analysis.

Si (211) was observed to have the largest surface coverage but also the highest oxidation rate. The Si (111) surface had the highest resistance to oxidation despite it having a sub monolayer coverage and the Si (110) surface had resistance to oxidation greater than the Si (211) phase. Angle dependence on each of the silicon surfaces indicate that any characterization of the surface using XPS will be sensitive on the angle at which the analysis is taken. Contributions from the sidewalls will increase as the substrate is turned away from surface normal.

Future work for the surface functionalization of silicon microwires would be reducing the junction resistance further with a group that can also be functionalized itself to attach molecular catalysts. Interaction between the polymer and the surface is still not clear and the mechanism of charge transfer across the interface between the n – type wire and PEDOT:PSS will need to be investigated further. Attachment of EDOT to the surface of the silicon microwire is expected to generate the best contact between the two phases. Electrochemical deposition from the monolayer of EDOT may also be possible because of its lower oxidation potential to thiophene. In addition, attachment of a molecular catalyst from either the thiophene or EDOT moiety can be done using Heck chemistry^{99, 100} and should be done from the microwire surface.

It still remains unclear whether the thiophene surface remains intact after long periods of exposure to ambient conditions. Investigating the longevity of the surface bound species and its impact on the junction would be very important to ensure the gains made from the attachment are not short lived. To do this, one would have to follow the oxidation and characteristic S 2s peak over the course of several months and take junction measurements of new wires at each time point to find the effect on junction potential.

Understanding how the silicon microwire surfaces behave can now be achieved using these planar representative silicon phases. Attachment of new groups to the surface of silicon

microwires should be carried out with these surfaces first to understand the expected surface coverages. In addition, new etching techniques to create atomically flat silicon microwire surfaces that would give maximum surface coverages will also be developed using these techniques in conjunction with AFM or STM characterization.

References

1. Perez, R.; Zweibel, K.; Hoff, T. E., Solar power generation in the US: Too expensive, or a bargain? *Energy Policy* **2011**, *39* (11), 7290-7297.
2. <http://www.bp.com/en/global/corporate/about-bp/energy-economics/statistical-review-of-world-energy.html>, BP Statistical Review of World Energy. 2014.
3. Lopez, A.; Roberts, B.; Heimiller, D.; Blair, D.; Porro, G. *U.S. Renewable Energy Technical Potentials: A GIS-Based Analysis*; National Renewable Energy Laboratory: 2012.
4. *Global Energy Assessment: Towards a Sustainable Future*. Cambridge University Press: 2012.
5. Lewis, N. S.; Nocera, D. G., Powering the planet: chemical challenges in solar energy utilization. *Proc Natl Acad Sci U S A* **2006**, *103* (43), 15729-35.
6. Walter, M. G.; Warren, E. L.; McKone, J. R.; Boettcher, S. W.; Mi, Q.; Santori, E. A.; Lewis, N. S., Solar water splitting cells. *Chemical Reviews* **2010**, *110* (11), 6446-73.
7. Lewis, N. S., Toward cost-effective solar energy use. *Science* **2007**, *315* (5813), 798-801.
8. Lewis, N. S., Light work with water. *Nature* **2001**, *414* (6864), 589-90.
9. Gray, H. B., Powering the planet with solar fuel. *Nat Chem* **2009**, *1* (1), 7.
10. Bolton, J. R.; Strickler, S. J.; Connolly, J. S., Limiting and Realizable Efficiencies of Solar Photolysis of Water. *Nature* **1985**, *316* (6028), 495-500.
11. Murphy, A. B.; Barnes, P. R. F.; Randeniya, L. K.; Plumb, I. C.; Grey, I. E.; Horne, M. D.; Glasscock, J. A., Efficiency of solar water splitting using semiconductor electrodes. *International Journal of Hydrogen Energy* **2006**, *31* (14), 1999-2017.
12. Bak, T.; Nowotny, J.; Rekas, M.; Sorrell, C. C., Photo-electrochemical hydrogen generation from water using solar energy. Materials-related aspects. *International Journal of Hydrogen Energy* **2002**, *27* (10), 991-1022.
13. Zhang, Z.; Yates, J. T., Jr., Band bending in semiconductors: chemical and physical consequences at surfaces and interfaces. *Chem Rev* **2012**, *112* (10), 5520-51.
14. Tan, M. X.; Laibinis, P. E.; Nguyen, S. T.; Kesselman, J. M.; Stanton, C. E.; Lewis, N. S., Principles and Applications of Semiconductor Photoelectrochemistry. *Progress in Inorganic Chemistry, Vol 41* **1994**, *41*, 21-144.
15. Sze, S. M., *Physics of Semiconductor Devices*. Wiley: New York: 1981.
16. Walter, M. G.; Liu, X. L.; O'Leary, L. E.; Brunschwig, B. S.; Lewis, N. S., Electrical Junction Behavior of Poly(3,4-ethylenedioxythiophene) (PEDOT) Contacts to H-Terminated and CH₃-Terminated p-, n-, and n(+)-Si(111) Surfaces. *J Phys Chem C* **2013**, *117* (28), 14485-14492.
17. McFarlane, S. L.; Day, B. A.; McEleney, K.; Freund, M. S.; Lewis, N. S., Designing electronic/ionic conducting membranes for artificial photosynthesis. *Energy & Environmental Science* **2011**, *4* (5), 1700-1703.
18. Kayes, B. M.; Atwater, H. A.; Lewis, N. S., Comparison of the device physics principles of planar and radial p-n junction nanorod solar cells. *J Appl Phys* **2005**, *97* (11).
19. Maiolo, J. R., 3rd; Kayes, B. M.; Filler, M. A.; Putnam, M. C.; Kelzenberg, M. D.; Atwater, H. A.; Lewis, N. S., High aspect ratio silicon wire array photoelectrochemical cells. *J Am Chem Soc* **2007**, *129* (41), 12346-7.
20. Kayes, B. M.; Filler, M. A.; Putnam, M. C.; Kelzenberg, M. D.; Lewis, N. S.; Atwater, H. A., Growth of vertically aligned Si wire arrays over large areas (> 1 cm²) with Au and Cu catalysts. *Appl Phys Lett* **2007**, *91* (10).

21. Kelzenberg, M. D.; Turner-Evans, D. B.; Kayes, B. M.; Filler, M. A.; Putnam, M. C.; Lewis, N. S.; Atwater, H. A., Photovoltaic measurements in single-nanowire silicon solar cells. *Nano Lett* **2008**, *8* (2), 710-4.
22. Putnam, M. C.; Filler, M. A.; Kayes, B. M.; Kelzenberg, M. D.; Guan, Y.; Lewis, N. S.; Eiler, J. M.; Atwater, H. A., Secondary ion mass spectrometry of vapor-liquid-solid grown, Au-catalyzed, Si wires. *Nano Lett* **2008**, *8* (10), 3109-13.
23. Warren, E. L.; Atwater, H. A.; Lewis, N. S., Silicon Microwire Arrays for Solar Energy-Conversion Applications. *The Journal of Physical Chemistry C* **2014**, *118* (2), 747-759.
24. Wagner, R. S.; Ellis, W. C., Vapour-Liquid-Solid Mechanism of Single Crystal Growth. *Appl Phys Lett* **1964**, *4* (5).
25. Kelzenberg, M. D.; Turner-Evans, D. B.; Putnam, M. C.; Boettcher, S. W.; Briggs, R. M.; Baek, J. Y.; Lewis, N. S.; Atwater, H. A., High-performance Si microwire photovoltaics. *Energy & Environmental Science* **2011**, *4* (3), 866.
26. Boettcher, S. W.; Warren, E. L.; Putnam, M. C.; Santori, E. A.; Turner-Evans, D.; Kelzenberg, M. D.; Walter, M. G.; McKone, J. R.; Brunschwig, B. S.; Atwater, H. A.; Lewis, N. S., Photoelectrochemical hydrogen evolution using Si microwire arrays. *J Am Chem Soc* **2011**, *133* (5), 1216-9.
27. McDonald, M. B.; Ardo, S.; Lewis, N. S.; Freund, M. S., Use of Bipolar Membranes for Maintaining Steady-State pH Gradients in Membrane-Supported, Solar-Driven Water Splitting Michael. *Chemsuschem* **2014**, *7* (11), 3021-3027.
28. McDonald, M. B.; Freund, M. S., Graphene Oxide as a Water Dissociation Catalyst in the Bipolar Membrane Interfacial Layer. *Acs Appl Mater Inter* **2014**, *6* (16), 13790-13797.
29. Hunger, R.; Fritsche, R.; Jaeckel, B.; Jaegermann, W.; Webb, L.; Lewis, N., Chemical and electronic characterization of methyl-terminated Si(111) surfaces by high-resolution synchrotron photoelectron spectroscopy. *Phys Rev B* **2005**, *72* (4).
30. Nemanick, E. J.; Hurley, P. T.; Webb, L. J.; Knapp, D. W.; Michalak, D. J.; Brunschwig, B. S.; Lewis, N. S., Chemical and electrical passivation of single-crystal silicon(100) surfaces through a two-step chlorination/alkylation process. *J Phys Chem B* **2006**, *110* (30), 14770-8.
31. Bansal, A.; Li, X. L.; Lauermann, I.; Lewis, N. S.; Yi, S. I.; Weinberg, W. H., Alkylation of Si surfaces using a two-step halogenation Grignard route. *J Am Chem Soc* **1996**, *118* (30), 7225-7226.
32. Bansal, A.; Lewis, N. S., Stabilization of Si photoanodes in aqueous electrolytes through surface alkylation. *J Phys Chem B* **1998**, *102* (21), 4058-4060.
33. Terry, J.; Linford, M. R.; Wigren, C.; Cao, R.; Pianetta, P.; Chidsey, C. E. D., Alkyl-terminated Si(111) surfaces: A high-resolution, core level photoelectron spectroscopy study. *J Appl Phys* **1999**, *85* (1), 213.
34. He, J.; Patitsas, S. N.; Preston, K. F.; Wolkow, R. A.; Wayner, D. D. M., Covalent bonding of thiophenes to Si(111) by a halogenation/thienylation route. *Chemical Physics Letters* **1998**, *286* (5-6), 508-514.
35. Boukherroub, R.; Morin, S.; Bensebaa, F.; Wayner, D. D. M., New synthetic routes to alkyl monolayers on the Si(111) surface. *Langmuir : the ACS journal of surfaces and colloids* **1999**, *15* (11), 3831-3835.
36. Buriak, J. M., Illuminating Silicon Surface Hydrosilylation: An Unexpected Plurality of Mechanisms. *Chem Mater* **2013**, *26* (1), 763-772.
37. Buriak, J. M., Organometallic chemistry on silicon and germanium surfaces. *Chem Rev* **2002**, *102* (5), 1271-308.

38. Terry, J.; Linford, M. R.; Wigren, C.; Cao, R.; Pianetta, P.; Chidsey, C. E. D., Determination of the bonding of alkyl monolayers to the Si(111) surface using chemical-shift, scanned-energy photoelectron diffraction. *Appl Phys Lett* **1997**, *71* (8), 1056.
39. Yahyaie, I.; McEleney, K.; Walter, M.; Oliver, D. R.; Thomson, D. J.; Freund, M. S.; Lewis, N. S., Electrical Characterization of Si Microwires and of Si Microwire/Conducting Polymer Composite Junctions. *J Phys Chem Lett* **2011**, *2* (6), 675-680.
40. Yahyaie, I.; McEleney, K.; Walter, M. G.; Oliver, D. R.; Thomson, D. J.; Freund, M. S.; Lewis, N. S., Characterization of the Electrical Properties of Individual p-Si Microwire/Polymer/n-Si Microwire Assemblies. *J Phys Chem C* **2011**, *115* (50), 24945-24950.
41. Yahyaie, I.; Ardo, S.; Oliver, D. R.; Thomson, D. J.; Freund, M. S.; Lewis, N. S., Comparison between the electrical junction properties of H-terminated and methyl-terminated individual Si microwire/polymer assemblies for photoelectrochemical fuel production. *Energy & Environmental Science* **2012**, *5* (12), 9789-9794.
42. McClarty, M. M.; Bruce, J. P.; Freund, M. S.; Oliver, D. R., Piezoresistive characterization of bottom-up, n-type silicon microwires undergoing bend deformation. *Appl Phys Lett* **2015**, *106* (2), 022107.
43. Bruce, J. P.; Asgari, S.; Ardo, S.; Lewis, N. S.; Oliver, D. R.; Freund, M. S., Measurement of the Electrical Resistance of n-Type Si Microwire/p-Type Conducting Polymer Junctions for Use in Artificial Photosynthesis. *J Phys Chem C* **2014**, *118* (48), 27742-27748.
44. Bolton, J. R., Solar fuels. *Science* **1978**, *202* (4369), 705-11.
45. Bolton, J. R., Solar photoproduction of hydrogen: A review. *Solar Energy* **1996**, *57* (1), 37-50.
46. Haussener, S.; Hu, S.; Xiang, C.; Weber, A. Z.; Lewis, N. S., Simulations of the irradiation and temperature dependence of the efficiency of tandem photoelectrochemical water-splitting systems. *Energy & Environmental Science* **2013**, *6* (12), 3605-3618.
47. Haussener, S.; Xiang, C. X.; Spurgeon, J. M.; Ardo, S.; Lewis, N. S.; Weber, A. Z., Modeling, Simulation, and Design Criteria for Photoelectrochemical Water-Splitting Systems. *Energy & Environmental Science* **2013**.
48. Hu, S.; Xiang, C.; Haussener, S.; Berger, A. D.; Lewis, N. S., An analysis of the optimal band gaps of light absorbers in integrated tandem photoelectrochemical water-splitting systems. *Energy & Environmental Science* **2013**, *6* (10), 2984.
49. Nemanick, E. J.; Hurley, P. T.; Brunschwig, B. S.; Lewis, N. S., Chemical and electrical passivation of silicon (111) surfaces through functionalization with sterically hindered alkyl groups. *J Phys Chem B* **2006**, *110* (30), 14800-8.
50. Webb, L. J.; Lewis, N. S., Comparison of the electrical properties and chemical stability of crystalline silicon(111) surfaces alkylated using grignard reagents or olefins with Lewis acid catalysts. *J Phys Chem B* **2003**, *107* (23), 5404-5412.
51. Webb, L. J.; Nemanick, E. J.; Biteen, J. S.; Knapp, D. W.; Michalak, D. J.; Traub, M. C.; Chan, A. S.; Brunschwig, B. S.; Lewis, N. S., High-resolution X-ray photoelectron spectroscopic studies of alkylated silicon(111) surfaces. *J Phys Chem B* **2005**, *109* (9), 3930-7.
52. Yu, H.; Webb, L. J.; Ries, R. S.; Solares, S. D.; Goddard, W. A., 3rd; Heath, J. R.; Lewis, N. S., Low-temperature STM images of methyl-terminated Si(111) surfaces. *J Phys Chem B* **2005**, *109* (2), 671-4.
53. Grant, J. T., Methods for Quantitative-Analysis in Xps and Aes. *Surf Interface Anal* **1989**, *14* (6-7), 271-283.

54. Seah, M. P., A Review of the Analysis of Surfaces and Thin-Films by Aes and Xps. *Vacuum* **1984**, *34* (3-4), 463-478.
55. Green, M. A., Silicon solar cells: state of the art. *Philosophical transactions. Series A, Mathematical, physical, and engineering sciences* **2013**, *371* (1996), 20110413.
56. Putnam, M. C.; Boettcher, S. W.; Kelzenberg, M. D.; Turner-Evans, D. B.; Spurgeon, J. M.; Warren, E. L.; Briggs, R. M.; Lewis, N. S.; Atwater, H. A., Si microwire-array solar cells. *Energy & Environmental Science* **2010**, *3* (8), 1037.
57. Spanninga, S. A.; Martin, D. C.; Chen, Z., X-ray Photoelectron Spectroscopy Study of Counterion Incorporation in Poly(3,4-ethylenedioxythiophene) (PEDOT) 2: Polyanion Effect, Toluenesulfonate, and Small Anions. *J Phys Chem C* **2010**, *114* (35), 14992-14997.
58. Lourdudoss, S.; Zhang, S. L., High-Concentration Phosphorus Doping of Polycrystalline Silicon by Low-Temperature Direct Vapor-Phase Diffusion of Phosphine Followed by Rapid Thermal Annealing. *Appl Phys Lett* **1994**, *64* (25), 3461-3463.
59. Solmi, S.; Nobili, D., High concentration diffusivity and clustering of arsenic and phosphorus in silicon. *J Appl Phys* **1998**, *83* (5), 2484.
60. Boettcher, S. W.; Spurgeon, J. M.; Putnam, M. C.; Warren, E. L.; Turner-Evans, D. B.; Kelzenberg, M. D.; Maiolo, J. R.; Atwater, H. A.; Lewis, N. S., Energy-conversion properties of vapor-liquid-solid-grown silicon wire-array photocathodes. *Science* **2010**, *327* (5962), 185-7.
61. Chang, C. A., Formation of Copper Silicides from Cu(100)/Si(100) and Cu(111)/Si(111) Structures. *J Appl Phys* **1990**, *67* (1), 566-569.
62. Cros, A.; Aboelfotoh, M. O.; Tu, K. N., Formation, Oxidation, Electronic, and Electrical-Properties of Copper Silicides. *J Appl Phys* **1990**, *67* (7), 3328-3336.
63. Aboelfotoh, M. O.; Krusinbaum, L., Electrical Transport in Thin-Films of Copper Silicide. *J Appl Phys* **1991**, *70* (6), 3382-3384.
64. Dupré, L.; Buttard, D.; Leclere, C.; Renevier, H.; Gentile, P., Gold Contamination in VLS-Grown Si Nanowires: Multiwavelength Anomalous Diffraction Investigations. *Chem Mater* **2012**, *24* (23), 4511-4516.
65. Hannon, J. B.; Kodambaka, S.; Ross, F. M.; Tromp, R. M., The influence of the surface migration of gold on the growth of silicon nanowires. *Nature* **2006**, *440* (7080), 69-71.
66. Maldonado, S.; Plass, K. E.; Knapp, D.; Lewis, N. S., Electrical Properties of Junctions between Hg and Si(111) Surfaces Functionalized with Short-Chain Alkyls†. *The Journal of Physical Chemistry C* **2007**, *111* (48), 17690-17699.
67. Li, Y.; O'Leary, L. E.; Lewis, N. S.; Galli, G., Combined Theoretical and Experimental Study of Band-Edge Control of Si through Surface Functionalization. *J Phys Chem C* **2013**, *117* (10), 5188-5194.
68. Aliano, A.; Li, Y.; Cicero, G.; Galli, G., Structural and Electronic Properties of the Methyl-Terminated Si(111) Surface. *J Phys Chem C* **2010**, *114* (27), 11898-11902.
69. Arefi, H. H.; Fagas, G., Chemical Trends in the Work Function of Modified Si(111) Surfaces: A DFT Study. *The Journal of Physical Chemistry C* **2014**, *118* (26), 14346-14354.
70. Yu, M.; Doak, P.; Tamblyn, I.; Neaton, J. B., Theory of Covalent Adsorbate Frontier Orbital Energies on Functionalized Light-Absorbing Semiconductor Surfaces. *The Journal of Physical Chemistry Letters* **2013**, *4* (10), 1701-1706.
71. Maldonado, S.; Plass, K. E.; Knapp, D.; Lewis, N. S., Electrical Properties of Junctions between Hg and Si(111) Surfaces Functionalized with Short-Chain Alkyls. *J Phys Chem C* **2007**, *111* (48), 17690-17699.

72. Al-Anber, M.; Milde, B.; Alhalasah, W.; Lang, H.; Holze, R., Electrochemical and DFT-studies of substituted thiophenes. *Electrochim Acta* **2008**, *53* (20), 6038-6047.
73. Bolton, J. R.; Hall, D. O., Photo-Chemical Conversion and Storage of Solar-Energy. *Annual Review of Energy* **1979**, *4*, 353-401.
74. Callejas, J. F.; McEnaney, J. M.; Read, C. G.; Crompton, J. C.; Biacchi, A. J.; Popczun, E. J.; Gordon, T. R.; Lewis, N. S.; Schaak, R. E., Electrocatalytic and Photocatalytic Hydrogen Production from Acidic and Neutral-pH Aqueous Solutions Using Iron Phosphide Nanoparticles. *Acs Nano* **2014**, *8* (11), 11101-11107.
75. McEnaney, J. M.; Crompton, J. C.; Callejas, J. F.; Popczun, E. J.; Biacchi, A. J.; Lewis, N. S.; Schaak, R. E., Amorphous Molybdenum Phosphide Nanoparticles for Electrocatalytic Hydrogen Evolution. *Chem Mater* **2014**, *26* (16), 4826-4831.
76. McEnaney, J. M.; Crompton, J. C.; Callejas, J. F.; Popczun, E. J.; Read, C. G.; Lewis, N. S.; Schaak, R. E., Electrocatalytic hydrogen evolution using amorphous tungsten phosphide nanoparticles. *Chemical Communications* **2014**, *50* (75), 11026-11028.
77. Popczun, E. J.; Read, C. G.; Roske, C. W.; Lewis, N. S.; Schaak, R. E., Highly Active Electrocatalysis of the Hydrogen Evolution Reaction by Cobalt Phosphide Nanoparticles**. *Angew Chem Int Edit* **2014**, *53* (21), 5427-5430.
78. Wasylenko, D. J.; Palmer, R. D.; Schott, E.; Berlinguette, C. P., Interrogation of electrocatalytic water oxidation mediated by a cobalt complex. *Chem Commun (Camb)* **2012**, *48* (15), 2107-9.
79. Kanan, M. W.; Nocera, D. G., In situ formation of an oxygen-evolving catalyst in neutral water containing phosphate and Co²⁺. *Science* **2008**, *321* (5892), 1072-1075.
80. Reece, S. Y.; Hamel, J. A.; Sung, K.; Jarvi, T. D.; Esswein, A. J.; Pijpers, J. J. H.; Nocera, D. G., Wireless Solar Water Splitting Using Silicon-Based Semiconductors and Earth-Abundant Catalysts. *Science* **2011**, *334* (6056), 645-648.
81. Amy, S. R.; Chabal, Y. J., Alkylation of Silicon(111) surfaces. *J. Phys. IV France* **2006**, *132*, 195-198.
82. Bansal, A.; Lewis, N. S., Electrochemical properties of (111)-oriented n-Si surfaces derivatized with covalently-attached alkyl chains. *J Phys Chem B* **1998**, *102* (7), 1067-1070.
83. Wagner, R. S.; Treuting, R. G., Morphology and Growth Mechanism of Silicon Ribbons. *J Appl Phys* **1961**, *32* (11), 2490.
84. Wagner, R. S.; Ellis, W. C.; Jackson, K. A.; Arnold, S. M., Study of the Filamentary Growth of Silicon Crystals from the Vapor. *J Appl Phys* **1964**, *35* (10), 2993.
85. Jaeckel, B.; Hunger, R.; Webb, L. J.; Jaegermann, W.; Lewis, N. S., High-Resolution Synchrotron Photoemission Studies of the Electronic Structure and Thermal Stability of CH₃- and C₂H₅-Functionalized Si(111) Surfaces. *The Journal of Physical Chemistry C* **2007**, *111* (49), 18204-18213.
86. Webb, L. J.; Michalak, D. J.; Biteen, J. S.; Brunschwig, B. S.; Chan, A. S.; Knapp, D. W.; Meyer, H. M., 3rd; Nemanick, E. J.; Traub, M. C.; Lewis, N. S., High-resolution soft X-ray photoelectron spectroscopic studies and scanning auger microscopy studies of the air oxidation of alkylated silicon(111) surfaces. *J Phys Chem B* **2006**, *110* (46), 23450-9.
87. Fidélis, A.; Ozanam, F.; Chazalviel, J. N., Fully methylated, atomically flat (111) silicon surface. *Surface Science* **2000**, *444* (1-3), L7-L10.
88. Briggs, D.; Grant, J. T., *Surface Analysis by Auger and X-ray Photoelectron Spectroscopy*. 2003.

89. Webb, L. J.; Rivillon, S.; Michalak, D. J.; Chabal, Y. J.; Lewis, N. S., Transmission infrared spectroscopy of methyl- and ethyl-terminated silicon(111) surfaces. *J Phys Chem B* **2006**, *110* (14), 7349-56.
90. Fulk, C.; Sivananthan, S.; Zavitz, D.; Singh, R.; Trenary, M.; Chen, Y. P.; Brill, G.; Dhar, N., The structure of the Si (211) surface. *Journal of Elec Materi* **2006**, *35* (6), 1449-1454.
91. Jaime-Vasquez, M.; Martinka, M.; Groenert, M.; Dinan, J., Ion scattering and electron spectroscopy of the chemical species at a HF-prepared Si(211) surface. *Appl Phys Lett* **2006**, *88* (3), 031910.
92. Chadi, D. J., Theoretical study of the atomic structure of silicon (211), (311), and (331) surfaces. *Phys Rev B* **1984**, *29* (2), 785-792.
93. Wong, K. T.; Lewis, N. S., What a difference a bond makes: the structural, chemical, and physical properties of methyl-terminated Si(111) surfaces. *Accounts of chemical research* **2014**, *47* (10), 3037-44.
94. Krzywiecki, M.; Grządziel, L.; Peisert, H.; Biswas, I.; Chassé, T.; Szuber, J., X-ray Photoelectron Spectroscopy characterization of native and RCA-treated Si (111) substrates and their influence on surface chemistry of copper phthalocyanine thin films. *Thin Solid Films* **2010**, *518* (10), 2688-2694.
95. Khalilov, U.; Pourtois, G.; Huygh, S.; van Duin, A. C. T.; Neyts, E. C.; Bogaerts, A., New Mechanism for Oxidation of Native Silicon Oxide. *The Journal of Physical Chemistry C* **2013**, *117* (19), 9819-9825.
96. Haber, J. A.; Lewis, N. S., Infrared and X-ray Photoelectron Spectroscopic Studies of the Reactions of Hydrogen-Terminated Crystalline Si(111) and Si(100) Surfaces with Br₂, I₂, and Ferrocenium in Alcohol Solvents. *The Journal of Physical Chemistry B* **2002**, *106* (14), 3639-3656.
97. Solares, S. D.; Yu, H.; Webb, L. J.; Lewis, N. S.; Heath, J. R.; Goddard, W. A., 3rd, Chlorination-methylation of the hydrogen-terminated silicon(111) surface can induce a stacking fault in the presence of etch pits. *J Am Chem Soc* **2006**, *128* (12), 3850-1.
98. Kelzenberg, M. D.; Boettcher, S. W.; Petykiewicz, J. A.; Turner-Evans, D. B.; Putnam, M. C.; Warren, E. L.; Spurgeon, J. M.; Briggs, R. M.; Lewis, N. S.; Atwater, H. A., Enhanced absorption and carrier collection in Si wire arrays for photovoltaic applications. *Nature Materials* **2010**, *9* (3), 239-244.
99. O'Leary, L. E.; Rose, M. J.; Ding, T. X.; Johansson, E.; Brunshwig, B. S.; Lewis, N. S., Heck coupling of olefins to mixed methyl/thienyl monolayers on Si(111) surfaces. *J Am Chem Soc* **2013**, *135* (27), 10081-90.
100. Plass, K. E.; Liu, X. L.; Brunshwig, B. S.; Lewis, N. S., Passivation and secondary functionalization of allyl-terminated Si(111) surfaces. *Chem Mater* **2008**, *20* (6), 2228-2233.